

PREDICTION AND OBSERVATION OF TRANSFORMATION INDUCED PLASTICITY
BEHAVIOR IN CoCrNi MULTI-PRINCIPAL ELEMENT ALLOYS
WITH IN-SITU SYNCHROTRON X-RAY DIFFRACTION

by

John Andrew Copley

A thesis submitted to the Faculty and Board of Trustees of the Colorado School of Mines
in partial fulfillment of the requirements for the degree of Master of Science (Metallurgical and
Materials Engineering)

Golden, Colorado

Date _____

Signed: _____

John Andrew Copley

Signed: _____

Dr. Amy Clarke
Thesis Advisor

Golden, Colorado

Date _____

Signed: _____

Dr. Angus Rockett
Professor and Head
Department of Metallurgical and Materials Engineering

ABSTRACT

CoCrNi alloys are of interest as potential blast resistant materials, due to their high damage tolerance and toughness enhancing deformation mechanisms. As blast resistant materials need to exhibit high toughness in dynamic conditions, studies of the effects of strain rate on the activation of transformation- and twinning-induced plasticity, or TRIP and TWIP, respectively, are required. This work examines a CALPHAD-based approach to identifying TRIP capable alloys using the diffusionless transformation temperature, denoted as T_0 . The challenges associated with in-situ observation of phase transformations during dynamic deformation by state-of-the-art, synchrotron x-ray imaging and diffraction and strategies to minimize them are also explored. Using the CALPHAD-based approach for predicting TRIP, five multi-principal element alloys (MPEAs) were selected as both likely and unlikely to experience TRIP, and then tested under dynamic conditions at the Advanced Photon Source at Argonne National Laboratory with simultaneous x-ray diffraction to monitor for potential phase transformation. TRIP behavior was observed in two alloys with the highest diffusionless transformation temperatures, while it was suppressed in alloys with lower diffusionless transformation temperatures. This is attributed to adiabatic heating effects during high rate deformation. TRIP behavior was also observed in a Co-rich MPEA by in-situ synchrotron x-ray diffraction at the Brazilian Synchrotron Light Laboratory during quasi-static straining over a range of temperatures, before TRIP behavior was suppressed at high temperatures.

TABLE OF CONTENTS

| | |
|---|------|
| ABSTRACT..... | iii |
| LIST OF FIGURES | vi |
| LIST OF TABLES..... | xiii |
| ACKNOWLEDGEMENTS..... | xiv |
| CHAPTER 1: GENERAL INTRODUCTION AND LITERATURE REVIEW | 1 |
| 1.1 General Introduction..... | 1 |
| 1.2 Literature Review..... | 2 |
| 1.2.1 Multi-Principal Element Alloys and CoCrNi-Alloys..... | 2 |
| 1.2.2 Transformation and Twinning Induced Plasticity..... | 7 |
| 1.2.3 Calculation of Phase Diagrams | 10 |
| 1.2.4 Time Resolved Synchrotron Diffraction with High Rate Straining..... | 12 |
| References..... | 15 |
| CHAPTER 2: IDENTIFICATION OF TRIP ALLOYS BY CALPHAD METHODS, AN ACCESSIBLE APPROACH | 24 |
| 2.1 Abstract..... | 24 |
| 2.2 Introduction..... | 24 |
| 2.3 Approach..... | 25 |
| 2.4 Methods and Results..... | 26 |
| 2.5 Discussion..... | 32 |
| 2.6 Conclusions..... | 33 |
| 2.8 Supplemental Materials | 34 |
| References..... | 36 |
| CHAPTER 3: HISPOD AS A PREPERATORY TOOL FOR IMPROVING DESIGN OF HIGH-RATE-TIME-RESOLVED SYNCHROTRON X-RAY DIFFRACTION EXPERIMENTS | 41 |
| 3.1 Abstract..... | 41 |
| 3.2 Introduction..... | 41 |
| 3.3 Mitigating the diffraction effects of multiple harmonics by detector placement and sample geometry changes | 43 |
| 3.3.1 Energy dependent beam attenuation as a result of heavy or thick samples | 43 |
| 3.3.2 Detector positioning to minimize an unavoidable second harmonic | 45 |

| | | |
|--|---|----|
| 3.4 | Application of HiSPoD based optimization to a $\text{Co}_{50}\text{Cr}_{40}\text{Ni}_{10}$ MPEA..... | 47 |
| 3.4.1 | A brief description of TRIP behavior and interest | 47 |
| 3.4.2 | Second Harmonic Effects in $\text{Co}_{50}\text{Cr}_{40}\text{Ni}_{10}$ | 49 |
| 3.4.3 | Simulations of Transformation as Compared to Experimental Results | 50 |
| 3.5 | Summary | 50 |
| | References..... | 52 |
| CHAPTER 4: IN-SITU OBSERVATION OF FCC-HCP TRANSFORMATION INDUCED PLASTICITY BEHAVIOR DURING DYNAMIC DEFROMATION OF CoCrNi MULTI-PRINCIPAL ELEMENT ALLOYS | | 55 |
| 4.1 | Abstract..... | 55 |
| 4.2 | Background and Introduction | 55 |
| 4.3 | Experimental Methods..... | 57 |
| 4.3.1 | Quasi-Static Testing of a $\text{Co}_{55}\text{Cr}_{40}\text{Ni}_{15}$ MPEA at Elevated Temperatures..... | 57 |
| 4.3.2 | High Rate Testing of CoCrNi TRIP and TWIP MPEAs..... | 57 |
| 4.4 | Results..... | 58 |
| 4.5 | Discussion..... | 66 |
| 4.6 | Conclusions..... | 70 |
| 4.7 | Supplemental Materials | 71 |
| | References..... | 72 |
| CHAPTER 5: SUMMARY AND AVENUES FOR FUTURE WORK..... | | 76 |
| 5.1 | General summary and review of conclusions | 76 |
| 5.2 | Avenues for future work | 78 |
| APPENDICES | | 81 |
| Appendix A: Description of sample production and heat treatment..... | | 81 |
| Appendix B: Hardness Measurements of CoCrNi MPEAs | | 87 |

LIST OF FIGURES

| | |
|------------|--|
| Figure 1.1 | Entropy of configuration as a function of composition for a ternary alloy and the breakdowns of medium entropy alloys (MEAs) and low entropy alloys (LEAs), which are strict definitions based on entropy of mixing, as well as the less strictly defined multi-principal element alloys (MPEA) and conventional alloys, which do not have strict definitions or cutoffs.....5 |
| Figure 1.2 | Examples of planar defects in an FCC matrix that produce local regions of A-B-A-type stacking, as compared to an un-faulted, un-twinned crystal. The regions with A-B-C-type stacking are shown in blue, while the regions of A-B-A-type stacking are shown in red.....9 |
| Figure 1.3 | Improvement in both ultimate tensile strength and uniform elongation due to an increase in the work hardening rate of an alloy. The Considère criterion is used to evaluate the point at which instability will occur and shows an increase in mechanical performance for identical materials deforming by different mechanisms. Using area under the stress-strain curve as an approximation for toughness, it can be seen that a deformation mechanism favoring higher work hardening rates will increase damage tolerance.....11 |
| Figure 1.4 | . Example energy spectrum for white beam condition at Sector 32-ID at the APS using a 12 mm undulator gap, showing both the first and second harmonic, where the first harmonic has approximately 50 times the peak intensity of the second harmonic, but the second harmonic is much broader.....14 |
| Figure 2.1 | Free energy vs. composition curves may be used to define the diffusionless transformation temperature, T_0 , as the temperature at which the free energy curves of two phases intersect above the composition of interest, as illustrated above. T_0 can also be considered the projection of the intersection of two free energy surfaces onto the composition-temperature plane. The relative stability of the phases determines if T_0 increases or decreases with alloying. If the alloying element increases the stability of the high temperature phase, T_0 will decrease with alloying, such that $T_0(C_2) < T_0(C_1)$. If the alloying element increases the stability of the low temperature phase, T_0 will increase with alloying, such that $T_0(C_2) > T_0(C_1)$26 |

Figure 2.2 Plot of $\Delta G^{\alpha \rightarrow \beta}$ and T_0 for both TRIP and non-TRIP MPEAs and ferrous alloys. These data are distinguished based on their martensite phase as either BCC or HCP. All alloys shown here have an FCC parent austenite phase. The regions colored in red demark combinations of T_0 and $\Delta G^{\alpha \rightarrow \beta}$ which are not feasible for the case of α being the high temperature phase and β the martensitic phase. The TRIP enabled alloys are marked in blue and the non-TRIP alloys in orange. For $T/T_0 > 4$, T/T_0 is plotted as 4 for spacing. The results show clearly that these factors can be used to roughly group TRIP and non-TRIP alloys. The TRIP data that are shown above $T/T_0 = 1$ are marked with an “*”. These points are associated with TRIP behavior at cryogenic temperatures, and the predicted T_0 is well below room temperature. At these temperatures, accurate thermodynamic data, especially regarding the relative energies of non-equilibrium phases is difficult to generate.....30

Figure 2.3 Plot of $\Delta G^{\alpha \rightarrow \beta}$ and T_0 for both TRIP and non-TRIP Ti-alloys. The HCP phase listed as the martensite represents both the HCP martensite (α') and the orthorhombic martensite (α''), as these share a unified phase description in the TCTI2 Thermo-Calc databases. There are no easily demarked regions of TRIP and TWIP behavior, instead, the non-TRIP behavior continues to follow the TRIP behavior to well below $T/T_0 = 1$. The regions colored in red demark combinations of T_0 and $\Delta G^{\alpha \rightarrow \beta}$ which are not feasible for the case of α being the high temperature phase and β the martensitic phase. The TRIP enabled alloys are marked in blue and the non-TRIP alloys in orange. For $T/T_0 > 4$, T/T_0 is plotted as 4 for spacing.....32

Figure 3.1 Example energy spectrum for a “pink” beam at a synchrotron light source. This spectrum matches the output of Sector 32-ID of the Advanced Photon Source with an undulator gap of 12 mm. This is the energy spectrum used to generate all simulated diffraction and attenuated energy spectrum results in this work.....43

Figure 3.2 Schematic of the experimental setup for dynamic strain rate experiments at sector 32-ID of the APS, showing the positioning of the sample and detectors relative to the incident beam. Due to the requirement of the diffracted intensity to be transmitted through the sample in order to be collected, sample thickness effects become important for the diffraction.....44

Figure 3.3 Attenuation corrected energy spectrums and simulated diffraction patterns of various thicknesses of pure aluminum and nickel, highlighting the effect of composition and thickness on the relative intensity of the first and second harmonics. Light metals, like aluminum, have low attenuation coefficients and thus higher intensities for the peaks associated with the lower energy first harmonic. Heavier metals, such as nickel, have higher attenuation coefficients and thus lower relative intensities for the lower energy first harmonic. This effect can be mitigated by using a thinner sample. Practical limits exist, however. In order for nickel to have an equivalent relative intensity of the harmonics as the 500 μm thick aluminum requires a sample thickness of approximately 25 μm , which may be beyond a practical limit for machining or use. Note also for the case of the 500 μm thick nickel sample that the peaks associated with the second harmonic (the rightmost arc segments) are closer together and broader as compared to their equivalent peaks in the 25 μm nickel or 500 μm aluminum first harmonic cases. Only peak broadening as a result of the polychromatic nature of the beam is simulated, not other sources of broadening.....46

Figure 3.4 Simulated area diffraction patterns and corresponding integrated I vs 2θ plots for a 500 μm thick iron sample, illustrating how shifting the detector position can alter collected diffraction patterns. While the second harmonic remains more intense than the first for all cases, for right-shifted camera positions in positions 2 and 3, the only visible peaks associated with the high intensity 2nd harmonic are high index peaks with relatively low diffracted intensities. This enables observation of peaks that would have been too low in relative intensity to be observed simultaneously with the low index second harmonic peaks. Because the most intense peak is now associated with the first harmonic, all first harmonic peaks with sufficiently high relative intensity to be seen when the second harmonic is not considered can now be observed. Because the first harmonic peaks are low in absolute intensity, moving the detector closer to the sample can result in increased collected intensity, as more of each ring is in the view of the camera, however, this also results in decreasing the separation between peaks, as shown by position 3.....48

Figure 3.5 Attenuation corrected energy spectrums for given thicknesses of a TRIP enabled CoCrNi MPEA. As thickness decreases, both the relative intensity of the first and second harmonics and the absolute transmitted intensity increases. These thicknesses are actual sample thicknesses used during experiments at Sector 32-ID of the APS.....49

- Figure 3.6 Optimized and unoptimized area diffraction patterns for a 50/50 mixture of FCC and HCP $\text{Co}_{50}\text{Cr}_{40}\text{Ni}_{10}$ tested at Sector 32-ID-B of the APS. A comparison can be made between the simulated patterns (above) and the collected patterns (below), with low relative intensity peaks in the simulation invisible against the noise of the experimental results. Because the high index peaks have low relative intensity and have a lower arc length caught by the diffraction camera, they have low absolute intensity and can be difficult to conclusively capture during experiments. Also, there is increased broadening as compared to the simulated patterns. This occurs because simulated patterns only include broadening as a result of the polychromatic nature of the beam, no other sources. Differences between the aspect ratio of the experimental patterns are a result of different diffraction cameras being used.....51
- Figure 3.7 (Top) A comparison of an unoptimized and optimized simulation of a complete FCC \rightarrow HCP transformation in $\text{Co}_{50}\text{Cr}_{40}\text{Ni}_{10}$, as well as experimental results (bottom). In these simulations, the decrease in intensity of the FCC $\{111\}$ and $\{200\}$ peaks and appearance of the HCP $\{10\bar{1}1\}$ peak is much more evident in the optimized case, which uses both a decreased thickness ($100\ \mu\text{m}$ vs. $500\ \mu\text{m}$) and right-shift in detector position. In the unoptimized case, the high intensity of the high energy second harmonic results in the evidence of transformation being obscured by overlapping, broad peaks that are difficult to deconvolute, and the low intensity of peaks with sufficient separation to distinguish. In the optimized case, evidence of the transformation is clearer, as the peaks are both sharper and have greater separation.....52
- Figure 4.1 Diffusionless Transformation Temperatures of the CoCrNi ternary. Diffusionless transformation temperatures are increased by the additions of Co and Cr, which stabilize the HCP phase. Ni acts to stabilize the FCC phase, with resulting Ni-rich alloys having low T_0 , to the point of the HCP phase never being lower in energy than the FCC, regardless of temperature ($T_0 \leq 0\text{K}$). The single phase FCC region at 1200°C is marked with a dashed red line. The $\text{Co}_x\text{Cr}_{40}\text{Ni}_{60-x}$ line is marked by a black dotted line. Alloys believed to be TRIP enabled are marked by blue stars, and alloys believed to be TWIP enabled are marked by yellow stars.....59
- Figure 4.2 Heatmap of normalized intensity for $\text{Co}_{55}\text{Cr}_{40}\text{Ni}_5$ tested at 60°C showing the evolution of HCP peaks as a function of plastic strain from an initially pure FCC matrix. Detectable quantities of HCP begin forming at approximately 10% plastic strain, and the relative intensity of the HCP $(10\bar{1}1)$ peak continues to grow until approximately 20% plastic strain. The peaks are indexed and attributed to the FCC or HCP phases.....60

| | | |
|------------|---|----|
| Figure 4.3 | Heatmap of normalized intensity for $\text{Co}_{55}\text{Cr}_{40}\text{Ni}_5$ tested at 900°C showing no evolution of HCP peaks. This implies that either TRIP behavior was completely suppressed at this temperature, or so little transformation occurred that it could not be detected by the diffraction. In either case, this indicates elevated temperatures, even when still below T_0 , are able to result in suppressed TRIP behavior in CoCrNi alloys..... | 60 |
| Figure 4.4 | Transformation in $\text{Co}_{55}\text{Cr}_{40}\text{Ni}_5$ at 600°C continues after the failure of the sample (marked by red dashed line). The crosshead displacement (stroke) continues after the failure and ceases at approximately the same time as the HCP fraction plateaus. The constant rate of increase in HCP fraction with time differs from the logistic growth seen in the other temperatures with TRIP, but correlates well with the linear displacement. This suggests that HCP was forming in the material, likely in the necked region, before failure, and that after failure a more heavily transformed region was moved into the path of the beam..... | 62 |
| Figure 4.5 | Plots of HCP fraction as a function of plastic strain for tests from -100°C to 450°C behavior, as determined from in-situ diffraction experiments at LNLS, along with generalized logistic fits of the data to estimate the plateau heights of the samples that failed before the plateau was reached. This shows a decrease in the plateau height for the maximum HCP as a function of increasing temperature (due to porosity, the -100°C test failed at a too low a strain to allow accurate estimation of the plateau height). In addition to decreasing plateau height, the increasing temperatures resulted in decreased growth rates in the generalized logistic fits. In the plots, this appears as a decreasing slope of the near-linear portion of the logistic fits..... | 63 |
| Figure 4.6 | Comparison between simulated diffraction patterns showing a transformation from 100% FCC to 100% HCP, given the energy spectrum used for diffraction ($E_{peak} = 24.23\text{KeV}$, $\lambda_{peak} = 0.5117\text{\AA}$) and detector geometry with experimental results for a Co40 (non-TRIP), Co50 (TRIP), and Co55 (TRIP). The onset of straining, as well as failure or the end of the first straining pulse, whichever occurred first, are marked with dotted lines (gold and red, respectively). Qualitative comparison between the simulated diffraction and collected patterns shows a HCP fraction of 40-60% in the Co50 case at 30% strain, and of 60-80% in the Co55 case at 20% strain. Results for other non-TRIP alloys (CoCrNi and Co30) are similar to the Co40..... | 65 |

| | | |
|-------------|---|----|
| Figure 4.7 | Mechanical response of alloys tested at $1070 \pm 15s^{-1}$. Co30, CoCrNi, Co40, and Co50 all demonstrate similar mechanical response to the high rate deformation. Co55 showed limited ductility as compared to the lower Co alloys. Only the Co55 alloy failed before the end of the first strain pulse..... | 66 |
| Figure 4.8 | Measurements of stacking fault energy for Co55 at room temperature. These values are consistent with those reported in literature for Co-rich CoCrNi alloys, and are reflective of this alloy’s potential to exhibit TRIP type behavior. Measurement of the stacking fault energy was performed in the method of Pierce <i>et al</i> [35]. Results courtesy of Y. Guo, Colorado School of Mines..... | 67 |
| Figure 4.9 | Evolution of full diffraction rings from initially “spotty” rings collected before and during straining of Co40 at high rate ($1000s^{-1}$) at the APS. This behavior is attributed to deformation twinning, which is promoted in FCC alloys during high rate deformation, and has been shown to be a common deformation mechanism in the CoCrNi family of MPEAs..... | 70 |
| Figure 4.10 | Geometry of samples used during quasi-static testing at the XTMS beamline of the Brazilian Synchrotron Light Source. Dimensions in mm..... | 71 |
| Figure 4.11 | Geometry of samples used during high rate deformation of samples at Sector 32-ID of the Advanced Photon Source at Argonne National Laboratory. Dimensions in mm..... | 71 |
| Figure 5.1 | Example microstructural evolution visible in a TWIP enabled CoCrNi MPEA deformed under dynamic conditions at the APS with simultaneous synchrotron x-ray imaging. Grain and other microstructural features are clearly visible during deformation. This effect was maximized in the cases of thin and well-polished samples..... | 79 |
| Figure 5.2 | Maps of diffusionless transformation temperature (T_0) for two pseudo-ternary phase diagrams showing potential Fe-rich MPEAs capable of exhibiting FCC→HCP TRIP. Both pseudo-ternaries are 50 at% iron, with the remaining elements, either (top) Co-Cr-Ni or (bottom) Mn-Mi-Cr, comprising the remaining 50 at%. The FCC single phase region at 1200°C is marked with a black dotted and dashed line. While dual phase MPEAs have been studied, high volume fractions of σ -phase can form in these materials outside the FCC region, which can be significantly deleterious to mechanical performance..... | 80 |
| Figure A1 | An example backscatter electron micrograph of the spray formed Co ₅₅ Cr ₄₀ Ni ₅ alloy, showing a few large pores, circled in white. Grain contrast is a result of channeling contrast. Sample was section from the as cast material and mechanically polished to 0.05 μm | 81 |

| | | |
|------------|--|----|
| Figure A2 | MA backscatter electron micrograph of the bulk cast $\text{Co}_{55}\text{Cr}_{40}\text{Ni}_5$ alloy produced at UFSCar, illustrating the degree and size of inclusions. Black specks are chromium oxide inclusions. The sample was sectioned from the as cast material, then mechanically polished to $0.5 \mu\text{m}$ | 82 |
| Figure A3 | A backscatter electron micrograph of an example chromium-oxide found within the bulk cast $\text{Co}_{55}\text{Cr}_{40}\text{Ni}_5$ alloy produced at UFSCar, as well as EDS maps of the relative composition, showing the inclusion is rich in chromium and oxygen, while deficient in cobalt..... | 82 |
| Figure A4 | Backscatter electron micrograph and EDS map of the $\text{Co}_{30}\text{Cr}_{40}\text{Ni}_{30}$ alloy produced at Mines by arc melting, cold rolling to 50% reduction in height and annealing at 1200°C for two hours in air, illustrating the lack of visible secondary phases or segregation of the components. Sample was mechanically polished to $1 \mu\text{m}$ | 83 |
| Figure A5 | Equilibrium phase fraction for the equiatomic CoCrNi alloy as a function of temperature between 500°C and 1500°C | 84 |
| Figure A6 | Equilibrium phase fraction for $\text{Co}_{30}\text{Cr}_{40}\text{Ni}_{30}$ as a function of temperature between 500°C and 1500°C | 84 |
| Figure A7 | Equilibrium phase fraction for $\text{Co}_{40}\text{Cr}_{40}\text{Ni}_{20}$ as a function of temperature between 500°C and 1500°C | 85 |
| Figure A8 | Equilibrium phase fraction for $\text{Co}_{50}\text{Cr}_{40}\text{Ni}_{10}$ as a function of temperature between 500°C and 1500°C | 85 |
| Figure A9 | Equilibrium phase fraction for $\text{Co}_{55}\text{Cr}_{40}\text{Ni}_5$ as a function of temperature between 500°C and 1500°C | 86 |
| Figure A10 | XRD of a Co_{55} sample produced by arc melting, which was rolled to 50% reduction in height then annealed at 1200°C in air for 2 hours, then quenched to room temperature. It is unclear if the HCP present is due to the alloy possessing an M_s temperature above room temperature, or mechanically induced during the removal of oxide formed on the surface of this sample during heat treatment in open atmosphere..... | 86 |
| Figure A11 | XRD of a Co_{40} sample produced by arc melting, followed by rolling to 50% reduction in height, annealed at 1200°C in air for 2 hours, then quenched to room temperature. The diffraction indicates a fully FCC microstructure..... | 87 |

LIST OF TABLES

| | | |
|-------------|--|----|
| Table 2.1.1 | Alloy and thermodynamic data for steels and FCC→BCC MPEAs, including composition (in wt%, unless otherwise noted), TRIP behavior, testing temperature, diffusionless transformation temperature, normalized testing temperature, driving force for the transformation and reference. The BCC phase is used to describe both BCC and BCT martensite..... | 27 |
| Table 2.1.2 | Alloy and thermodynamic data for FCC→HCP MPEAs, including composition (in wt%, unless otherwise noted), TRIP behavior, testing temperature, diffusionless transformation temperature, normalized testing temperature, driving force for the transformation and reference..... | 29 |
| Table 2.1.3 | Alloy and thermodynamic data for BCC→HCP Ti-based alloys, including composition (in wt%, unless otherwise noted), TRIP behavior, testing temperature, diffusionless transformation temperature, normalized testing temperature, driving force for the transformation and reference. The HCP phase is used to describe both α' and α'' martensites..... | 31 |
| Table 4.1 | Diffusionless transformation temperatures for the alloys tested. For the equiatomic CoCrNi and Co30 alloys, the relative stability of the FCC and HCP phases is such that there is no temperature at which the HCP is predicted to be more stable than the FCC..... | 59 |
| Table 4.2 | Parameters for fits of TRIP behavior as a function of temperature for Co ₅₅ Cr ₄₀ Ni ₅ , showing decreasing upper asymptotes (K), as well as formation rates (B) with increasing temperatures. Also shown are the relevant thermodynamic parameters to TRIP behavior, T_0 and $\Delta G^{\text{FCC} \rightarrow \text{HCP}}$ for each temperature. 600°C and 750°C tests, which showed evolution of HCP after failure were not fit as the HCP formation is better attributed to changes in the sampled region than to deformation, and the 900°C test showed no HCP peak evolution..... | 64 |
| Table A1 | Vickers hardness measurements of several CoCrNi MPEAs with various reductions in height from rolling. All alloys started in the as annealed condition (1200°C for two hours)..... | 87 |

ACKNOWLEDGEMENTS

I would like to thank my loving girlfriend Anna for her forgiveness as I missed Valentines day for experiments at a beamline and her patience as I wrote this thesis. I can only hope that I will be as patient with her as she comes to the same stage in her graduate work.

I also thank my family, especially my parents who have stood behind me as I pursued my degrees, and humored me when I tried to explain what I was doing to them. I would also like to thank my brother, whose pride in my accomplishments dwarfs my own, and to whom I could always turn to brighten my day.

I would like to thank Hugh and Michelle Harvey for their financial support along my academic journey, as well as for their part in establishing the community of the Harvey Scholars, of whom I am proud to be a member.

I am grateful for the guidance provided by my advisor, Dr. Amy Clarke, as well as the opportunities she has produced for me to further both my research and career goals. None of the work that built this thesis would have been possible without her efforts and insights.

I thank all of the CANFSA students who assisted me with in-situ experiments for this thesis. Sector 32-ID runs non-stop, but much as I would like to, I cannot. This work could not have been performed without their help.

Dr. Francisco Coury provided both an initial direction to this project, and also invaluable insight during the course of my research.

I would like to thank my committee members Drs. Kip Findley and Kester Clarke, who have taken time out of their busy schedules to review and provide feedback on this work.

This work was supported by the Office of Naval Research (Award No. N00014-18-1-2567) through the Center for Advanced Non-Ferrous Structural Alloys (CANFSA), a National Science Foundation Industry/University Cooperative Research Center (I/UCRC) [Award No. 1624836], at the Colorado School of Mines (Mines). This research used resources of the Advanced Photon Source, a U.S. Department of Energy (DOE) Office of Science User Facility

operated for the DOE Office of Science by Argonne National Laboratory under Contract No. DE-AC02-06CH11357. Additionally, this work benefitted from use of the Brazilian Nanotechnology National Laboratory – LNNano and the Brazilian Synchrotron Light Laboratory – LNLS for the use of the XTMS installation at the XRD-1 beamline.

CHAPTER 1

GENERAL INTRODUCTION AND LITERATURE REVIEW

1.1 General Introduction

Multi-Principal Element Alloys (MPEAs), also referred to as complex concentrated alloys (CCAs) and high or medium entropy alloys (HEAs and MEAs) have gained much attention in recent years since their introduction in 2004 [1], [2]. This interest is a result of certain alloys' promising combinations of mechanical properties, such as strength and toughness, even at cryogenic temperatures [3]. These materials are generally equiatomic or near equiatomic, rendering it difficult to define a primary or principal component, thus distinguishing them from conventional alloys like steels, for example, which may contain numerous alloying additions in non-equiatomic amounts. As a result of occupying the center of high dimensional phase diagrams, rather than the corners and edges where most conventional alloy compositions reside, there is a vast number of possible alloys in a relatively unexplored design space [4], [5].

Exploring this design space with a purely experimental approach is difficult and incredibly time consuming. Efficient exploration requires the use of high throughput methods of predicting phase stability and mechanical properties, combined with experimental validation of promising alloys [6]. To this end, models ranging from simple CALPHAD-based investigations of phase stability to density functional theory, as well as complex artificial intelligence and machine learning approaches, have been used [7]–[11]. These models have had mixed success, needing more experimental results to form a strong basis from which accurate first principals or empirical models may be built.

While there is much exploration left to do, some alloys have shown excellent promise, especially the equiatomic CoCrNi alloy, which has shown remarkably high damage tolerance [12], [13]. The source of the equiatomic CoCrNi's excellent combination of strength and toughness has been attributed to deformation twinning [13]. Twinning induced plasticity and other toughness enhancing deformation mechanisms (such as transformation induced plasticity) can enable materials to overcome the strength-ductility tradeoff and result in simultaneously high strength and damage tolerant materials [3], [13]–[15]. This work focuses on predicting CoCrNi alloys capable of exhibiting transformation and twinning induced plasticity by use of a CALPHAD-based assessment of the thermodynamic factors behind these behaviors and

identifying the effects of strain rate, temperature, and alloying on the activation of these toughness enhancing deformation mechanisms.

1.2 Literature Review

A summary of existing literature relevant to this work follows below, broken into four main categories: Multi-Principal Element Alloys (MPEAs) and related materials, Transformation and Twinning Induced Plasticity (TRIP and TWIP), Calculation of Phase Diagrams (CALPHAD), and high rate, time resolved x-ray diffraction, which was utilized in this work to explore the dynamic response of selected MPEAs.

1.2.1 Multi-Principal Element Alloys and CoCrNi-Alloys

1.2.1.1 Multi Principal Element Alloys and Related Materials

High Entropy Alloys (HEAs) have grown in interest since Cantor *et al.* published “Microstructural development in equiatomic multi-component alloys” in 2004 [1]. While not naming these materials as HEAs, this work has served as the basis for continued studies of equiatomic, multi-component systems with five or more atomic species. Since Cantor *et al.* was published, much attention has been paid to the “Cantor Alloy”, an equiatomic FeMnCoCrNi face-centered-cubic (FCC) solid solution, as well as related alloys created by adding or substituting other transition block metals, especially 3d elements [16]–[24]. Definitions of HEAs vary, but are generally either entropy or composition based. The most common definitions for each category require either an entropy of configuration of $1.5R$ or greater ($|S_{config}| \geq 1.5R$), or for an alloy to contain 5 components with concentrations of 5-35 at% each [5]. As entropy was initially considered to be a critical factor in the properties of these materials, these definitions were designed to maximize the configurational entropy of the alloy. In the early years of HEA study, it was proposed that the high concentrations of solutes in HEAs generated four “core effects” described below [25]:

- 1) *The High Entropy Effect:* The high entropy of mixing for an alloy with a large number of components present in high concentrations is suggested to help stabilize a single disordered solid solution with extended solid solubility outside of the traditional Hume-Rothery rules and a simple crystal structure, such as face-centered-cubic (FCC), body-centered-cubic (BCC) or hexagonal-close-packed (HCP).

- 2) *The Lattice Distortion Effect*: Lattice distortions in HEAs are predicted to be larger than those in conventional alloys, resulting in increased strength and hardness and reduced thermal and electrical conductivity.
- 3) *The Sluggish Diffusion Effect*: Diffusivities in HEAs are suggested to be lower than in conventional alloys, improving their thermal stability.
- 4) *The “Cocktail” Effect*: The exploration of alloy design space outside that of conventional alloys could bear unexpected fruit due to the combination of elements in ways not yet considered, or an effect promoting a “whole greater than the sum of its parts.”

The first three of these effects are testable hypotheses, as thermodynamic studies, measures of mechanical and electrical properties, and diffusivities are relatively straightforward. The fourth core effect, the “Cocktail Effect,” is more a statement of hope in finding interesting and promising alloys than one based in a scientific hypothesis. These core effects have been largely discredited as large contributors to the alloys’ behavior over the last few years, but have served to inspire studies of HEAs and related materials, in part due to the identification of several promising alloys with interesting combinations of properties, such as strength and toughness at cryogenic temperatures [3], [13], [26]. Because the high entropy of mixing has been shown to be less critical than initially proposed, focus has shifted away from “true” HEAs to other categories of materials not necessarily meeting the strict definitions for an HEA [6], [13], [27]. These other categories have been referred to by a number of names, including Multi-Principal Element Alloys (MPEAs), Medium Entropy Alloys (MEAs), and Complex Concentrated Alloys (CCAs). These terms, aside from MEAs, do not have stringent definitions and are often used interchangeably in the literature. MEAs are defined as having an entropy of mixing between 1- and 1.5R ($1R \leq |S_{config}| < 1.5R$) [28]. These terms often overlap, as illustrated on page 5, in **Figure 1.1**. Continued studies of HEA-like materials has generally split into those focusing on either FCC and dual phase FCC-HCP structural alloys, or those focusing on BCC high temperature refractory alloys [4], [5], [29].

The “core effects” have been studied in more or less detail, depending on the effect. Much attention has been paid to the high entropy effect and the stability of solid solutions with large concentrations of solute [5]. Additional investigation into the effect has not supported a strong stabilizing effect of a high entropy of mixing. Firstly, the stability of the disordered phases

is in question, and many studies of the formation kinetics of ordered phases are underway by high resolution transmission electron microscopy and neutron diffraction [30], [31]. Secondly, examination of the thermodynamics of ordered phases, such as B2 or L1₂, were they to form within an HEA, has shown the increased enthalpy of formation of these phases as compared to disordered phases is sufficient to negate the effects of the increased entropy of mixing of “high entropy” disordered solid solutions [5]. The lattice strain effect has been investigated by diffraction, and most studies have found lattice strains not dissimilar to those of conventional, if highly alloyed, materials [32], [33]. Additionally, the anticipated mechanical responses of a highly strained lattice, namely strength and hardness, do not scale with entropy, as the equiatomic CoCrNi MEA with $\Delta S_{config} = -1.1R$ has superior mechanical properties as compared to the Cantor Alloy (equiatomic FeMnCoCrNi), with $\Delta S_{config} = -1.6R$, from which it was derived [6], [13]. The sluggish diffusion effect is perhaps the least studied of the core effects, but the experimental diffusivities found are not inconsistent with substitutional diffusion in conventional FCC alloys, especially when normalized for melting temperature [34], [35]. Additional evidence against anomalously slow diffusion is found in the ease at which precipitates form in many HEAs [2], [36]–[40]. However, some computational approaches have predicted sluggish diffusion as a result of larger amplitude fluctuations in interatomic potential for HEAs as compared to conventional alloys [34].

Traditionally, studies of the mechanical behavior of MPEAs and related materials focused on the solid solution strengthening component, as it was anticipated to be high compared to conventional alloys [6], [41]–[44]. However, with the discovery of equiatomic CoCrNi’s excellent combination of strength and toughness as a result of deformation twinning, a new focus on MPEAs and similar materials with deformation mechanisms like TRAnsformation Induced Plasticity (TRIP) and TWinning Induced Plasticity (TWIP) has grown [9], [12], [53], [54], [45]–[52]. The studies of TRIP and TWIP behavior in MPEAs and related materials has generally focused on low temperature applications, including cryogenic temperatures where the equiatomic CoCrNi has shown unrivaled toughness [12], [55]. Less attention has been paid to the mechanical behavior of FCC and dual phase FCC-HCP MPEAs at elevated temperatures, as higher temperatures act to suppress both TRIP and TWIP behavior [56]. While many MPEA studies focus on equiatomic and near equiatomic compositions, the study of TRIP and TWIP behavior has forced studies away from equiatomic compositions to Fe-, Mn-, and Co- rich alloys,

where TRIP and TWIP are more thermodynamically favorable [46], [53], [57]–[60]. Additionally, interstitial High Entropy Alloys (iHEAs), where interstitial C or N additions are utilized to alter mechanical properties and deformation mechanisms as in steels, are being investigated [48], [61], [62].

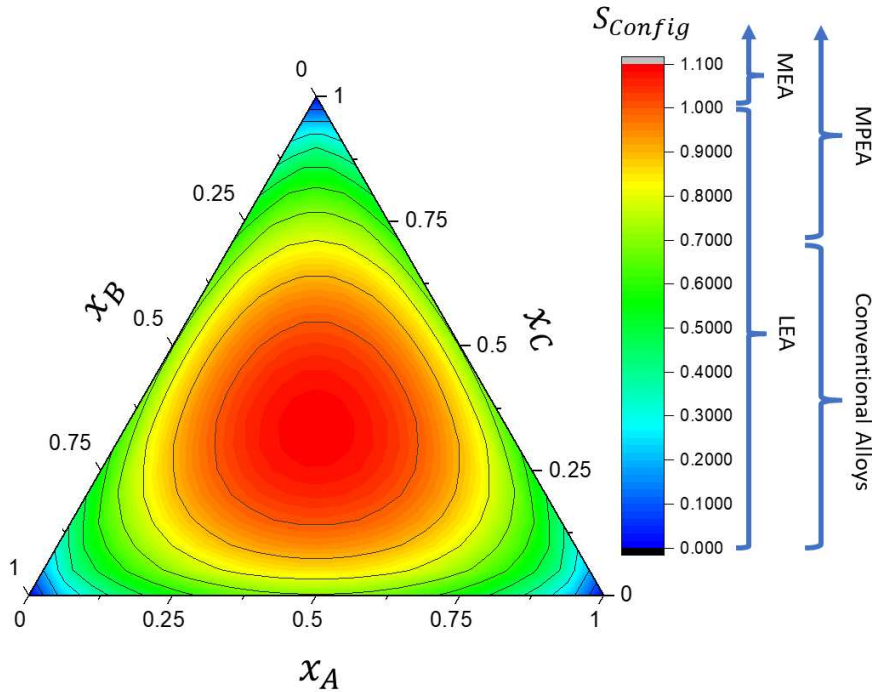


Figure 1.1: Entropy of configuration as a function of composition for a ternary alloy and the breakdowns of medium entropy alloys (MEAs) and low entropy alloys (LEAs), which are strict definitions based on entropy of mixing, as well as the less strictly defined multi-principal element alloys (MPEA) and conventional alloys, which do not have strict definitions or cutoffs

Calculating the number of potential alloys living within the HEA/MEA/MPEA design space, when counting differences in composition of no less than 5at% and considering there are 72 non-radioactive elements (not including noble gases or halogens), generates more than 10^{37} combinations. As a result, high throughput methods are useful for identifying promising alloys before experimental validation [6], [27]. Different methods used range from simple CALPHAD type approaches using Thermo-Calc or Pandat software that identify likely single-phase regions (to avoid mechanically deleterious intermetallics such as σ -phase), to methods examining the electronic or magnetic structures of materials, to complex artificial intelligence and machine learning approaches, developed with the goal of directly identifying alloys with specific desired

properties like strength or ductility [7]–[11], [63]–[66]. Some success has been found with each approach, but more data is needed to accurately model high dimension phase diagrams and predict behaviors.

1.2.1.2 State of the Art in CoCrNi Alloys

Originally explored in the 1960s and 1970s for Co-based super alloys, which require additional alloying elements to form carbides or a γ' phase to achieve high temperature performance, CoCrNi alloys have only recently grown in interest again. This resurgence is due primarily to the identification of the equiatomic CoCrNi alloy's excellent combination of strength and ductility, even at cryogenic temperatures [12]. This alloy has been reported as one of the toughest alloys in literature, with K_{JIC} values of 200 MPa m^{1/2} at room temperature and 275 MPa m^{1/2} at cryogenic temperatures (77K) [12]. This behavior has been attributed to deformation twinning, which is favored at low temperatures. The reported high toughness as a result of the TWIP effect has resulted in growing interest in exploiting the TWIP and TRIP behaviors to produce high toughness MPEAs [7], [9], [67]–[70].

The initial work on CoCrNi has shown that Co and Cr additions act to reduce stacking fault energies [71], [72]. Experimentally measured room temperature stacking fault energies range from 10 – 60 mJ/m², depending upon the alloy, with the lowest stacking fault energies being reported in alloys with greater than 70% Co [73]. The effect of Co on the γ_{SFE} of CoCrNi alloys is expected, due to its low temperature equilibrium structure being HCP, while the effect of Cr (BCC at room temperature) is more complicated. These low stacking fault energies enable the activation of strain-induced martensitic transformation, as well as deformation twinning, which have been studied in closely related alloys (e.g. CoCrNiMo alloys) since at least the 1970s [74].

After publication on the “Cantor alloy” by Cantor *et al.* in 2004 and the later move away from focusing on the “High Entropy Effect”, the CoCrNi ternary system was rediscovered, with the most interest being paid to the equiatomic alloy [1], [5], [13], [24]. Other alloys from this system have shown superior mechanical performance and the potential for even higher toughness as a result of optimized solid solution strengthening. Additionally, in Co-rich alloys, the stabilization of the HCP phase at low temperatures has enabled activation of a strain induced martensitic transformation from FCC→HCP [74]. One such alloy, Co₅₅Cr₄₀Ni₅, was shown by

in-situ synchrotron x-ray diffraction to experience a FCC→HCP transformation as a function of strain, producing a simultaneously strong and ductile alloy through the TRIP effect [53].

Due to the temperature dependence of the deformation mechanisms responsible for these alloys' combination of strength and ductility, more work has focused on their cryogenic properties; relatively little work has been performed at elevated temperatures [3], [11], [12], [63]. However, as high strain rate and low temperature are often considered analogous with respect to their effects on deformation behavior, the low temperature performance of these materials indicates that they may also be suitable for high strain rate applications, such as blast resistance. There are few studies on the high rate performance of MPEAs in general, and none that focus on the CoCrNi ternary, but initial work has shown both an increase in strength and ductility with increasing strain rate for the equiatomic FeMnCoCrNi and FeCoCrNi alloys [75], [76]. In addition to the promotion of high yield and flow stresses as a result of suppression of thermal contributions to dislocation motion at high strain rates, this behavior has been attributed to the activation and increased frequency of deformation twinning with increasing strain rate in FCC materials. Limited studies have been performed on the dynamic response of MPEAs that exhibit TRIP behavior [77].

1.2.2 Transformation and Twinning Induced Plasticity

Transformation and twinning induced plasticity are credited with the combination of strength and ductility present in some HEAs [13], [46], [48]. Both TRIP and TWIP have been more thoroughly explored and developed for advanced high strength steels, and a larger body of literature exists regarding these behaviors in ferrous alloys [78], [79]. These deformation mechanisms are capable of extending uniform elongation through increased work hardening rates [79]–[83]. The actual source of the high work hardening rates is complex, but a simplified description, the “dynamic Hall-Petch effect,” is commonly cited as a source of the high strain hardening in TWIP materials [67], [68], [84]–[86]. The dynamic Hall-Petch effect centers on TWIP generating barriers to dislocation motion as a function of strain. Twin boundaries generally do not allow for conservation of a dislocation's Burger's vector, preventing glide across the boundary. As the mean free path for dislocation motion decreases as a function of strain, it is analogous to shrinking the grain size, hence the name “dynamic Hall-Petch effect.” In-situ experiments have shown this to be a simplified assessment of the actual source of strain

hardening behavior in TWIP steels [86]. For TRIP materials, the martensite phase is often a lower symmetry phase and can have reduced ductility and increased strength as compared to the austenite phase. The evolution of a hard phase during straining, as in steels and some MPEAs, can result in stress partitioning to the martensite and produce a composite strengthening type effect, and again, one that evolves with strain, producing high work hardening rates [56], [79], [87]. While the actual dislocation/twin/martensite interactions may be complex, it remains valid to assert that both TRIP and TWIP result in high work hardening rates.

The transformation in ferrous TRIP alloys is a strain-induced martensitic transformation (SIMT), where strain provides the requisite impetus to initiate a transformation, usually from an FCC austenite parent phase to a BCC or BCT product martensite phase, though in some alloys ϵ -martensite, an HCP phase, forms [14], [80], [88]–[93]. In all cases, the transformation is governed by the thermodynamics of diffusionless transformations and limited by the diffusionless transformation temperature, T_0 [94]. For a given composition, this is the temperature at which two phases have identical free energies. Below this temperature, a transformation from the high temperature phase to the low temperature phase may proceed without diffusion and still produce free energy savings. Because of the lack of diffusion as a limiting step, these types of transformations are fast as compared to diffusionally driven transformations [94]. As the transformation cannot proceed forward above T_0 , T_0 serves as a hard limit for the operational temperature of a TRIP enabled alloy. However, T_0 alone cannot be considered as the maximum temperature at which TRIP *will* occur, only the maximum temperature TRIP *may* occur.

The formation of deformation twins in a TWIP alloy is dominated by the stacking fault energy, γ_{SFE} , with low γ_{SFE} materials being more likely to experience TWIP behavior [95]–[100]. The Olsen-Cohen model for stacking fault energy in FCC materials describes the stacking fault energy as a combination of a volumetric free energy change, due to the local change in crystal structure associated with the stacking fault, as well as an interfacial energy, as described below, by **Equation 1.1** [90]:

$$\gamma_{SFE} = \frac{8}{\sqrt{3}} * \frac{1}{a^2 N_A} (\Delta G_m^{\gamma \rightarrow \epsilon} + E_m^{str}) + 2\sigma \quad (1.1)$$

where a is the lattice parameter of the FCC unit cell, N_A is Avagadro's constant, $\Delta G_m^{Y \rightarrow \epsilon}$ is the molar free energy change for the FCC \rightarrow HCP transformation, E_m^{str} is the molar strain energy, and σ is the surface energy of the FCC \rightarrow HCP phase boundary.

While a twin is not a stacking fault, the energetic cost of each are strongly related. In an FCC matrix, a twin forms a three atomic layer thick region of A-B-A-type stacking, while an intrinsic stacking fault in FCC forms a four atomic layer thick region of A-B-A-type stacking. These defects and the HCP nano-regions they form are illustrated in **Figure 1.2**. These defects are effectively a few atomic layers of HCP in an FCC matrix, and the energy associated with their formation can be described by the energy difference between the FCC and HCP phases for the given composition and the surface energy associated with their interfaces with the matrix FCC. Here, the greatest difference in describing the two is due to the difference in volume to surface area ratio, which are fixed for each case. While both twins and stacking faults diffusionlessly form some volume of HCP, they are not subject to the diffusionless transformation temperature, largely because the volume of a twin or stacking fault is so small as to be negligible when compared to the volume of a bulk transformation, indicating the surface energy and strain terms strongly contribute to the twinning behavior.

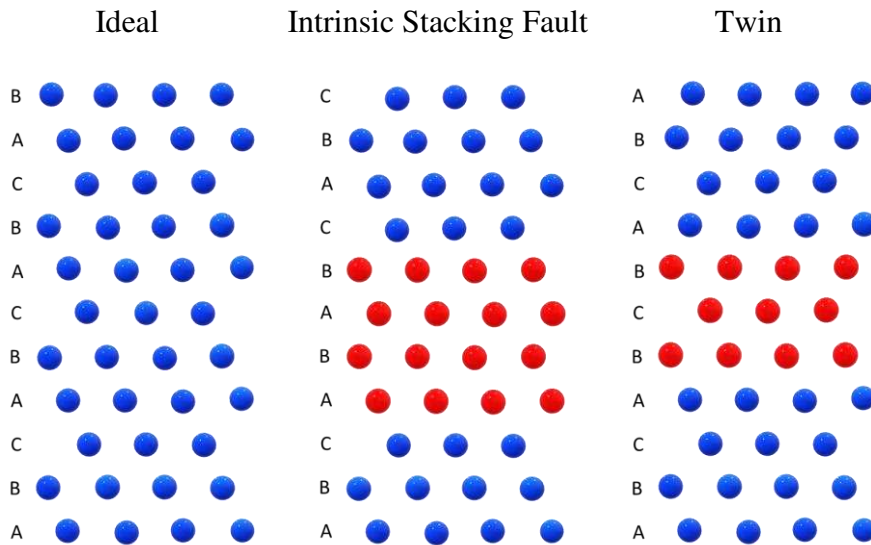


Figure 1.2: Examples of planar defects in an FCC matrix that produce local regions of A-B-A-type stacking, as compared to an un-faulted, un-twinned crystal. The regions with A-B-C-type stacking are shown in blue, while the regions of A-B-A-type stacking are shown in red.

In addition to TWIP, the stacking fault energy is often described as determining an alloy's TRIP potential, where materials move from deforming by dislocation slip to twinning induced plasticity to transformation induced plasticity as γ_{SFE} decreases [81], [95], [100]. This is easiest to understand in FCC-HCP TRIP alloys, as the structure-based free energy term, $\Delta G_m^{\gamma \rightarrow \epsilon}$ that is a component of γ_{SFE} is identical to the free energy change for the martensitic transformation, $\Delta G_{FCC-HCP}$. With more negative $\Delta G_{FCC-HCP}$, γ_{SFE} decreases, and TRIP becomes more favorable. Additionally, twins and twin intersections can serve as nuclei or nucleation sites for the product phases, especially in an FCC \rightarrow HCP martensitic transformation [89]. The relationship between γ_{SFE} and $\Delta G_{FCC-HCP}$ can also partially explain the temperature dependence of γ_{SFE} . As temperature changes, the energy difference between the FCC and HCP phases can change, altering the stacking fault energy. In materials where FCC becomes more stable compared to HCP at elevated temperatures, this results in an increasing γ_{SFE} with temperature. For other alloys, such as TRIP steels with non-FCC-HCP transformations, the relationship between TRIP and low γ_{SFE} is less easily understood, but is still applicable [81], [89], [101], [102].

The dynamic Hall-Petch effect, which results in increased work hardening rates, is beneficial to the mechanical performance of alloys and can allow them to overcome the strength-ductility tradeoff paradigm. The Considère criterion indicates that increased work hardening rates will result in increased ultimate tensile strength and uniform elongation. This is illustrated on page 11 in **Figure 1.3**. While these are not the only contributions to a material's toughness, they do help produce a damage tolerant material. The excellent toughness of the equiatomic CoCrNi has been attributed to its deformation twinning [13].

1.2.3 Calculation of Phase Diagrams

Calculation of Phase Diagrams or CALPHAD techniques utilize models of alloying, temperature, and pressure effects on a phase's free energy to predict phase stability. Since their development by Kaufman and Bernstein in 1970, CALPHAD techniques have been expanded to be used in integrated computational materials engineering (ICME), and many CALPHAD-based programs have added capability to model diffusion and non-equilibrium behavior as well [103]. Thermo-Calc and Pandat softwares are among the most recognized and used commercial

CALPHAD-based softwares. In this study, CALPHAD approaches are used to both identify single phase solid solutions and alloys likely to experience TRIP behavior.

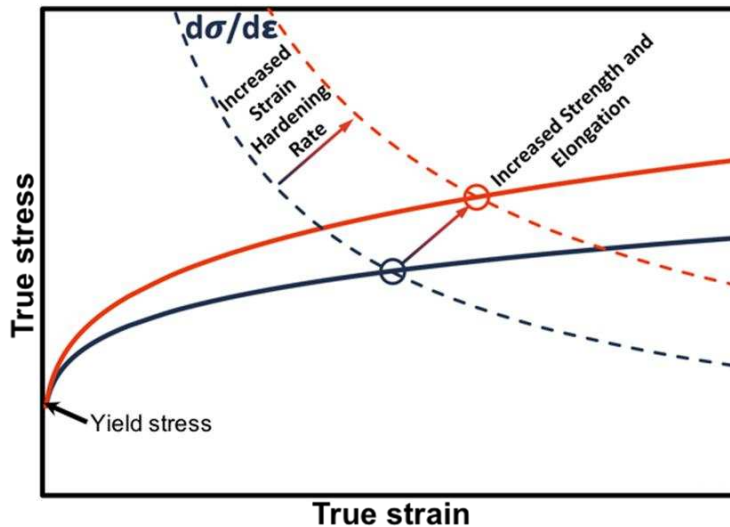


Figure 1.3: Improvement in both ultimate tensile strength and uniform elongation due to an increase in the work hardening rate of an alloy. The Considère criterion is used to evaluate the point at which instability will occur and shows an increase in mechanical performance for identical materials deforming by different mechanisms. Using area under the stress-strain curve as an approximation for toughness, it can be seen that a deformation mechanism favoring higher work hardening rates will increase damage tolerance

Because of the large number of potential MPEA compositions, high throughput methods for examining phase stability are invaluable in alloy design studies of MPEAs and related materials. In CALPHAD approaches, models of a phase’s free energy dependence on temperature, composition and pressure are used to evaluate the combination of phases and compositions that will minimize free energy given a set of constraints (composition, pressure, and temperature). While the relationship between free energy curves and phase diagrams was known well before the development of CALPHAD, CALPHAD enabled the quantitative calculation of phase stability for complex alloys and higher dimensionality phase diagrams [103]. Also, because the free energy for all phases are evaluated for a given set of constraints, CALPHAD approaches can also examine metastability by evaluating the difference in energy between two phases or by suspending from consideration the lowest energy phase.

Frequently, the compositional dependence of a phase’s free energy are described by Compound Energy Formalism (CEF) variants, which can be used to describe a wide range of

types of phases, including liquids, disordered solids, ordered solid solutions and gas phases [104]. CALPHAD methodologies take advantage of the ability of most phases with more than three or four components to be described as solid solutions of phases with fewer components. This allows the polynomial terms for the CEFs to be extracted from lower dimensionality phase diagrams (binary and ternary) and still be applied to higher dimensionality phase diagrams (quaternary and greater) with little loss in accuracy [105]. In addition to composition, CALPHAD approaches model the effects of temperature and pressure. The temperature dependence of a phase's free energy is often described by:

$$G_m^\phi = a + bT + cT \ln(T) + \sum_n d_n T^n \quad (1.2)$$

where a , b , c , and d are experimentally determined coefficients [106]. Experiments to evaluate these coefficients and the terms of the CEFs for compositional effects focus on binary and ternary systems, both because they are generally sufficient for assessment of more complex systems, and because the difficulty in assessing a phase diagram completely grows exponentially with the number of components. Pressure effects are modeled differently, depending on the software, but are generally only valid for small and medium pressure changes, with geological pressures producing non-physical results [103]. This work focuses primarily on the CoCrNi ternary system, which is fully assessed in both the TCHEA3 and TCHEA4 databases developed by Thermo-Calc. Additionally, assessment of ferrous and titanium alloys has been performed using TCFE9 and TCTI2, respectively. Because these databases contain hundreds of fully and partially assessed ternary systems, developing our own databases for this work is not practical.

1.2.4 Time Resolved Synchrotron Diffraction with High Rate Straining

In-situ experiments are highly beneficial for studies of transformation rates and interaction between straining and transformation, especially for high rate testing. At lower strain rates ($\dot{\epsilon} < 10 \text{ s}^{-1}$), it is possible to perform interrupted mechanical tests, where straining is stopped, a non-destructive experiment is performed on the sample, often x-ray diffraction, and straining is resumed. While easy to perform, the discontinuities in straining can result in different behavior during an interrupted test as compared to continuous straining. For higher rate deformation ($\dot{\epsilon} \geq 100 \text{ s}^{-1}$), however, interrupted tests become challenging due to momentum effects, where stopping the displacement takes time and interferes with the accuracy of the measured stop. As strain rates increase further ($\dot{\epsilon} \geq 1000 \text{ s}^{-1}$), instrumentation moves away

from load frames into pressure bar setups where there is no instrumental control of the displacement rate after the bar is released. Mechanical stops can be added to the system to force deformation to cease at a certain displacement, but additional straining is not possible on the same sample, so inter-sample variation can create discontinuities in behavior. As a result, in situ experiments, with time resolved results can overcome the limitations of high rate experiments.

For diffraction during high rate deformation, other challenges emerge. Given high rate deformation tests using Kolsky Bar or other types of pressure bars last on the order of tens of micro-seconds, a high flux of x-rays is required. As a result, high rate experiments like these are usually performed at synchrotron light sources or free electron lasers (FELs). While FELs produce significantly higher peak intensity x-rays than synchrotrons, they are not designed for time resolved imaging or diffraction, being designed instead to generate one high intensity burst of x-rays [107]. Synchrotrons are able to generate repeated, timed bursts of x-rays, but their lower intensity can produce difficulty in collecting sufficient diffracted intensity during a high rate deformation experiment [107]. Additionally, a synchrotron x-ray beam is not as inherently monochromatic as an FEL's. For many synchrotron experiments that are not intensity limited, the beam can be monochromated, whether by use of a longer set of undulator magnets or by diffraction through a crystal [108]. Techniques to monochromate a beam often result in intensity loss, and can reduce the intensity of the beam to the point where high rate, time resolved diffraction experiments cannot collect sufficient diffracted intensity to differentiate from noise [108]. As a result, some diffraction experiments utilize a “pink” beam. This is a polychromatic beam with a relatively sharp peak that balances the need for mostly mono-chromatic x-rays, in order to get meaningful diffraction and the need for high intensity to collect enough signal for interpretable results when limited to short integration times. An example energy spectrum for a “pink” beam is shown in **Figure 1.4**, on page 14.

The lack of a truly monochromatic beam results in broad diffraction peaks that can be difficult to deconvolute if overlapped. Additionally, due to the mechanism by which an undulator produces x-rays, there can also be intensity associated with higher level harmonics than the first peak [109]. The harmonics arise from the sinusoidal nature of the magnetic field produced by the undulator. The first harmonic is comprised of x-rays generated by magneto-bremsstrahlung, with the electrons oscillating with a frequency matching that of the undulator. The second harmonic is

comprised of x-rays generated by electrons oscillating at twice the frequency of the undulator, and consequently, generates x-ray wavelengths half that of the first harmonic. In undulator setups designed to produce largely monochromatic light, these generally have lower intensities than the first harmonic, but can be broader. Depending on their relative intensities and interactions between the sample and the x-rays, these higher energy harmonics can have more or less effect on the diffraction. If they contribute to diffraction, they produce additional sets of rings at lower angles than the rings associated with the first harmonic. **Figure 1.4**, below, is an example of a multi-harmonic energy spectrum, with the second harmonic being lower in intensity, but broader than the first harmonic. In this work, synchrotron x-ray experiments were performed both at the Advanced Proton Source (APS) at Argonne National Laboratory and at the Brazilian National Synchrotron Light Laboratory (LNLS). The LNLS experiments were performed using a monochromated beam during quasi-static straining, while the APS experiments were performed under dynamic conditions using “pink-beam” conditions, specifically, those described by the energy spectrum shown in **Figure 1.4**, below.

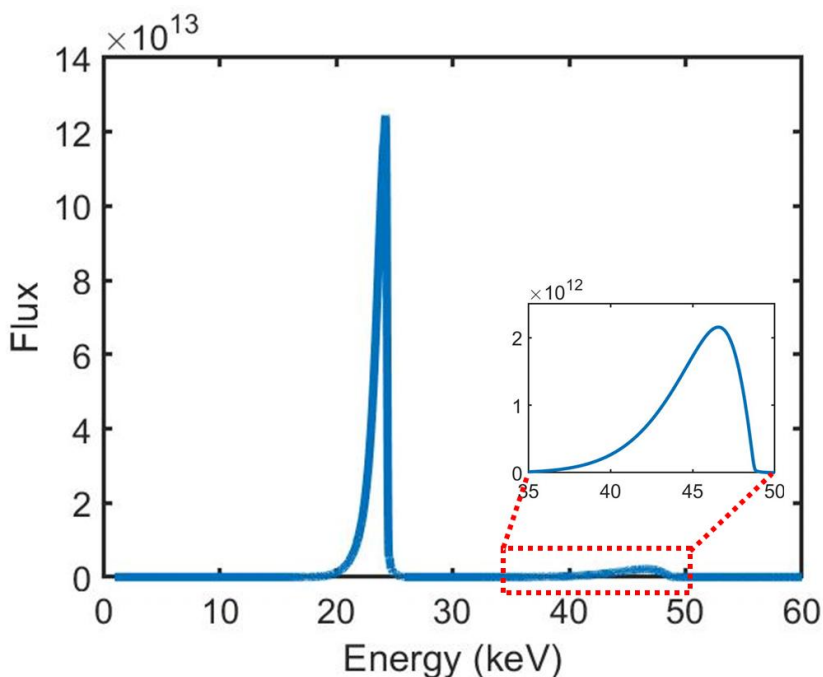


Figure 1.4: Example energy spectrum for white beam condition at Sector 32-ID at the APS using a 12 mm undulator gap, showing both the first and second harmonic, where the first harmonic has approximately 50 times the peak intensity of the second harmonic, but the second harmonic is much broader.

References

- [1] B. Cantor, I. T. H. Chang, P. Knight, and A. J. B. Vincent, “Microstructural development in equiatomic multicomponent alloys,” *Mater. Sci. Eng. A*, vol. 375–377, pp. 213–218, Jul. 2004.
- [2] J. W. Yeh *et al.*, “Nanostructured high-entropy alloys with multiple principal elements: Novel alloy design concepts and outcomes,” *Adv. Eng. Mater.*, vol. 6, no. 5, pp. 299–303, May 2004.
- [3] B. Gludovatz, A. Hohenwarter, D. Catoor, E. H. Chang, E. P. George, and R. O. Ritchie, “A fracture-resistant high-entropy alloy for cryogenic applications,” *Science (80-.)*, vol. 345, no. 6201, pp. 1153–1158, Sep. 2014.
- [4] S. Gorsse, D. B. Miracle, and O. N. Senkov, “Mapping the world of complex concentrated alloys,” *Acta Mater.*, vol. 135, pp. 177–187, Aug. 2017.
- [5] D. B. Miracle and O. N. Senkov, “A critical review of high entropy alloys and related concepts,” *Acta Mater.*, vol. 122, pp. 448–511, 2017.
- [6] F. G. Coury, P. Wilson, K. D. Clarke, M. J. Kaufman, and A. J. Clarke, “High-throughput solid solution strengthening characterization in high entropy alloys,” *Acta Mater.*, vol. 167, pp. 1–11, Apr. 2019.
- [7] M. Beyramali Kivy and M. Asle Zaeem, “Generalized stacking fault energies, ductilities, and twinnabilities of CoCrFeNi-based face-centered cubic high entropy alloys,” *Scr. Mater.*, vol. 139, pp. 83–86, Oct. 2017.
- [8] D. Ma, B. Grabowski, F. Körmann, J. Neugebauer, and D. Raabe, “Ab initio thermodynamics of the CoCrFeMnNi high entropy alloy: Importance of entropy contributions beyond the configurational one,” *Acta Mater.*, vol. 100, pp. 90–97, Nov. 2015.
- [9] Z. Li, F. Körmann, B. Grabowski, J. Neugebauer, and D. Raabe, “Ab initio assisted design of quinary dual-phase high-entropy alloys with transformation-induced plasticity,” *Acta Mater.*, vol. 136, pp. 262–270, Sep. 2017.
- [10] T. Klaver, D. Simonovic, and M. Sluiter, “Brute Force Composition Scanning with a CALPHAD Database to Find Low Temperature Body Centered Cubic High Entropy Alloys,” *Entropy*, vol. 20, no. 12, p. 911, Nov. 2018.
- [11] Z. Yang *et al.*, “Designing transformation-induced plasticity and twinning-induced plasticity Cr-Co-Ni medium entropy alloys: theory and experiment,” Elsevier BV, Feb. 2020.
- [12] B. Gludovatz *et al.*, “Exceptional damage-tolerance of a medium-entropy alloy CrCoNi at cryogenic temperatures,” *Nat. Commun.*, vol. 7, pp. 1–8, Feb. 2016.

- [13] G. Laplanche, A. Kostka, C. Reinhart, J. Hunfeld, G. Eggeler, and E. P. George, “Reasons for the superior mechanical properties of medium-entropy CrCoNi compared to high-entropy CrMnFeCoNi,” *Acta Mater.*, vol. 128, pp. 292–303, Apr. 2017.
- [14] S. Yan, T. Liang, Z. Wang, B. Yan, T. Li, and X. Liu, “Novel 1.4 GPa-strength medium-Mn steel with uncompromised high ductility,” *Mater. Sci. Eng. A*, vol. 773, p. 138732, Jan. 2020.
- [15] S. S. Sohn, H. Song, M. C. Jo, T. Song, H. S. Kim, and S. Lee, “Novel 1.5 GPa-strength with 50%-ductility by transformation-induced plasticity of non-recrystallized austenite in duplex steels,” *Sci. Rep.*, vol. 7, p. 1255, Dec. 2017.
- [16] S. G. Ma *et al.*, “Superior high tensile elongation of a single-crystal CoCrFeNiAl 0.3 high-entropy alloy by Bridgman solidification,” *Intermetallics*, vol. 54, pp. 104–109, Nov. 2014.
- [17] H. M. Daoud, A. Manzoni, R. Völkl, N. Wanderka, and U. Glatzel, “Microstructure and tensile behavior of Al₈Co₁₇Cr₁₇Cu₈Fe₁₇Ni₃₃ (at.%) high-entropy alloy,” *JOM*, vol. 65, no. 12, pp. 1805–1814, Dec. 2013.
- [18] S. J. Sun *et al.*, “Enhanced strength and ductility of bulk CoCrFeMnNi high entropy alloy having fully recrystallized ultrafine-grained structure,” *Mater. Des.*, vol. 133, pp. 122–127, Nov. 2017.
- [19] F. Wang, Y. Zhang, G. Chen, and H. A. Davies, “Tensile and compressive mechanical behavior of a CoCrCuFeNiAl_{0.5} high entropy alloy,” in *International Journal of Modern Physics B*, 2009, vol. 23, no. 6–7, pp. 1254–1259.
- [20] C. Ng *et al.*, “Phase stability and tensile properties of Co-free Al 0.5CrCuFeNi₂ high-entropy alloys,” *J. Alloys Compd.*, vol. 584, pp. 530–537, 2014.
- [21] A. V. Kuznetsov, D. G. Shaysultanov, N. D. Stepanov, G. A. Salishchev, and O. N. Senkov, “Tensile properties of an AlCrCuNiFeCo high-entropy alloy in as-cast and wrought conditions,” *Mater. Sci. Eng. A*, vol. 533, pp. 107–118, Jan. 2012.
- [22] A. J. Zaddach, R. O. Scattergood, and C. C. Koch, “Tensile properties of low-stacking fault energy high-entropy alloys,” *Mater. Sci. Eng. A*, vol. 636, pp. 373–378, Jun. 2015.
- [23] A. Gali and E. P. George, “Tensile properties of high- and medium-entropy alloys,” *Intermetallics*, vol. 39, pp. 74–78, 2013.
- [24] Z. Wu, H. Bei, G. M. Pharr, and E. P. George, “Temperature dependence of the mechanical properties of equiatomic solid solution alloys with face-centered cubic crystal structures,” *Acta Mater.*, vol. 81, pp. 428–441, 2014.
- [25] J. W. Yeh, “Recent progress in high-entropy alloys,” *Ann. Chim. Sci. des Mater.*, vol. 31, pp. 633–648, Nov. 2006.

- [26] Z. J. Zhang *et al.*, “Nanoscale origins of the damage tolerance of the high-entropy alloy CrMnFeCoNi,” *Nat. Commun.*, vol. 6, p. 10143, Dec. 2015.
- [27] F. G. Coury *et al.*, “Phase equilibria, mechanical properties and design of quaternary refractory high entropy alloys,” *Mater. Des.*, vol. 155, pp. 244–256, 2018.
- [28] M. C. Gao, J.-W. Yeh, P. K. Liaw, and Y. Zhang, “High-Entropy Alloys,” 2016.
- [29] D. B. Miracle, J. D. Miller, O. N. Senkov, C. Woodward, M. D. Uchic, and J. Tiley, “Exploration and development of high entropy alloys for structural applications,” *Entropy*, vol. 16, no. 1, pp. 494–525, 2014.
- [30] E. J. Pickering, R. Muñoz-Moreno, H. J. Stone, and N. G. Jones, “Precipitation in the equiatomic high-entropy alloy CrMnFeCoNi,” *Scr. Mater.*, vol. 113, pp. 106–109, Mar. 2016.
- [31] A. Fernández-Caballero, J. S. Wróbel, P. M. Mummery, and D. Nguyen-Manh, “Short-Range Order in High Entropy Alloys: Theoretical Formulation and Application to Mo-Nb-Ta-V-W System,” *J. Phase Equilibria Diffus.*, vol. 38, pp. 391–403, Aug. 2017.
- [32] N. L. Okamoto, K. Yuge, K. Tanaka, H. Inui, and E. P. George, “Atomic displacement in the CrMnFeCoNi high-entropy alloy - A scaling factor to predict solid solution strengthening,” *AIP Adv.*, vol. 6, p. 125008, Dec. 2016.
- [33] L. R. Owen, E. J. Pickering, H. Y. Playford, H. J. Stone, M. G. Tucker, and N. G. Jones, “An assessment of the lattice strain in the CrMnFeCoNi high-entropy alloy,” *Acta Mater.*, vol. 122, pp. 11–18, 2017.
- [34] K.-Y. Tsai, M.-H. Tsai, and J.-W. Yeh, “Sluggish diffusion in Co–Cr–Fe–Mn–Ni high-entropy alloys,” *Acta Mater.*, vol. 61, pp. 4887–4897, 2013.
- [35] A. M. Brown and M. F. Ashby, “CORRELATIONS FOR DIFFUSION CONSTANTS,” *Acta Metall.*, vol. 28, pp. 1085–1101, Aug. 1980.
- [36] N. G. Jones, J. W. Aveson, A. Bhowmik, B. D. Conduit, and H. J. Stone, “On the entropic stabilisation of an Al_{0.5}CrFeCoNiCu high entropy alloy,” *Intermetallics*, vol. 54, pp. 148–153, Nov. 2014.
- [37] M. R. Chen, S. J. Lin, J. W. Yeh, S. K. Chen, Y. S. Huang, and M. H. Chuang, “Effect of vanadium addition on the microstructure, hardness, and wear resistance of Al_{0.5}CoCrCuFeNi high-entropy alloy,” *Metall. Mater. Trans. A Phys. Metall. Mater. Sci.*, vol. 37, pp. 1363–1369, 2006.
- [38] N. G. Jones, A. Frezza, and H. J. Stone, “Phase equilibria of an Al_{0.5}CrFeCoNiCu high entropy alloy,” *Mater. Sci. Eng. A*, vol. 615, pp. 214–221, Oct. 2014.

- [39] K. B. Zhang *et al.*, “Annealing on the structure and properties evolution of the CoCrFeNiCuAl high-entropy alloy,” *J. Alloys Compd.*, vol. 502, no. 2, pp. 295–299, Jul. 2010.
- [40] T. T. Shun, C. H. Hung, and C. F. Lee, “Formation of ordered/disordered nanoparticles in FCC high entropy alloys,” *J. Alloys Compd.*, vol. 493, no. 1–2, pp. 105–109, Mar. 2010.
- [41] C. Varvenne, G. P. M. Leyson, M. Ghazisaeidi, and W. A. Curtin, “Solute strengthening in random alloys,” *Acta Mater.*, vol. 124, pp. 660–683, May 2017.
- [42] C. R. LaRosa, M. Shih, C. Varvenne, and M. Ghazisaeidi, “Solid solution strengthening theories of high-entropy alloys,” *Mater. Charact.*, vol. 151, pp. 310–317, May 2019.
- [43] C. Varvenne, A. Luque, and W. A. Curtin, “Theory of strengthening in fcc high entropy alloys,” *Acta Mater.*, vol. 118, pp. 164–176, Oct. 2016.
- [44] I. Toda-Caraballo and P. E. J. Rivera-Díaz-del-Castillo, “Modelling and Design of Magnesium and High Entropy Alloys Through Combining Statistical and Physical Models,” *JOM*, vol. 67, pp. 108–117, Dec. 2015.
- [45] C. E. Slone, S. Chakraborty, J. Miao, E. P. George, M. J. Mills, and S. R. Niezgod, “Influence of deformation induced nanoscale twinning and FCC-HCP transformation on hardening and texture development in medium-entropy CrCoNi alloy,” *Acta Mater.*, vol. 158, pp. 38–52, Oct. 2018.
- [46] W. Fang *et al.*, “Transformation Induced Plasticity Effects of a Non-Equal Molar Co-Cr-Fe-Ni High Entropy Alloy System,” *Metals (Basel)*, vol. 8, no. 5, p. 369, May 2018.
- [47] D. Wei *et al.*, “Novel Co-rich high performance twinning-induced plasticity (TWIP) and transformation-induced plasticity (TRIP) high-entropy alloys,” *Scr. Mater.*, vol. 165, pp. 39–43, May 2019.
- [48] M. Wang, Z. Li, and D. Raabe, “In-situ SEM observation of phase transformation and twinning mechanisms in an interstitial high-entropy alloy,” *Acta Mater.*, vol. 147, pp. 236–246, Apr. 2018.
- [49] J. Li, Q. Fang, B. Liu, and Y. Liu, “Transformation induced softening and plasticity in high entropy alloys,” *Acta Mater.*, vol. 147, pp. 35–41, Apr. 2018.
- [50] S. F. Liu *et al.*, “Transformation-reinforced high-entropy alloys with superior mechanical properties via tailoring stacking fault energy,” *J. Alloys Compd.*, vol. 792, pp. 444–455, Jul. 2019.
- [51] L. Rémy and A. Pineau, “Twinning and strain-induced f.c.c. → h.c.p. transformation on the mechanical properties of Co□Ni□Cr□Mo alloys,” *Mater. Sci. Eng.*, vol. 26, no. 1, pp. 123–132, Nov. 1976.

- [52] Y. H. Jo *et al.*, “FCC to BCC transformation-induced plasticity based on thermodynamic phase stability in novel V10Cr10Fe45CoxNi35-x medium-entropy alloys,” *Sci. Rep.*, vol. 9, p. 2948, Dec. 2019.
- [53] F. G. Coury *et al.*, “Design and in-situ characterization of a strong and ductile co-rich multicomponent alloy with transformation induced plasticity,” *Scr. Mater.*, vol. 173, 2019.
- [54] S. J. Sun *et al.*, “Transition of twinning behavior in CoCrFeMnNi high entropy alloy with grain refinement,” *Mater. Sci. Eng. A*, vol. 712, pp. 603–607, Jan. 2018.
- [55] Y. Wang *et al.*, “Probing deformation mechanisms of a FeCoCrNi high-entropy alloy at 293 and 77 K using in situ neutron diffraction,” *Acta Mater.*, vol. 154, pp. 79–89, Aug. 2018.
- [56] Z. Li, K. G. Pradeep, Y. Deng, D. Raabe, and C. C. Tasan, “Metastable high-entropy dual-phase alloys overcome the strength-ductility trade-off,” *Nature*, vol. 534, pp. 227–230, May 2016.
- [57] T. Tisone, “The concentration and temperature dependence of the stacking fault energy in face-centered cubic Co-Fe alloys,” *Acta Metall.*, vol. 21, no. 3, pp. 229–236, Mar. 1973.
- [58] W. Fang *et al.*, “Effects of Cobalt on the structure and mechanical behavior of non-equal molar CoxFe50-xCr25Ni25 high entropy alloys,” *Mater. Sci. Eng. A*, vol. 723, pp. 221–228, Apr. 2018.
- [59] K. Cho, Y. Fujioka, T. Nagase, and H. Y. Yasuda, “Grain refinement of non-equiatomic Cr-rich CoCrFeMnNi high-entropy alloys through combination of cold rolling and precipitation of σ phase,” *Mater. Sci. Eng. A*, vol. 735, pp. 191–200, Sep. 2018.
- [60] B. Cai *et al.*, “Deformation mechanisms of Mo alloyed FeCoCrNi high entropy alloy: In situ neutron diffraction,” *Acta Mater.*, vol. 127, pp. 471–480, Apr. 2017.
- [61] Z. Li, C. C. Tasan, H. Springer, B. Gault, and D. Raabe, “Interstitial atoms enable joint twinning and transformation induced plasticity in strong and ductile high-entropy alloys,” *Sci. Rep.*, vol. 7, p. 40704, Dec. 2017.
- [62] Z. Li, “Interstitial equiatomic CoCrFeMnNi high-entropy alloys: carbon content, microstructure, and compositional homogeneity effects on deformation behavior,” *Acta Mater.*, vol. 164, pp. 400–412, Feb. 2019.
- [63] S. Huang *et al.*, “Temperature dependent stacking fault energy of FeCrCoNiMn high entropy alloy,” *Scr. Mater.*, vol. 108, pp. 44–47, Nov. 2015.
- [64] W. Wang *et al.*, “An experimental and theoretical study of duplex fcc+hcp cobalt based entropic alloys,” *Acta Mater.*, vol. 176, pp. 11–18, Sep. 2019.

- [65] C. Zhang and M. C. Gao, “CALPHAD modeling of high-entropy alloys,” in *High-Entropy Alloys: Fundamentals and Applications*, Springer International Publishing, 2016, pp. 399–444.
- [66] Z. Zhou, Y. Zhou, Q. He, Z. Ding, F. Li, and Y. Yang, “Machine learning guided appraisal and exploration of phase design for high entropy alloys,” *npj Comput. Mater.*, vol. 5, p. 128, Dec. 2019.
- [67] H. Huang *et al.*, “Critical stress for twinning nucleation in CrCoNi-based medium and high entropy alloys,” *Acta Mater.*, vol. 149, pp. 388–396, May 2018.
- [68] S.-H. Joo *et al.*, “Tensile deformation behavior and deformation twinning of an equimolar CoCrFeMnNi high-entropy alloy,” *Mater. Sci. Eng. A*, vol. 689, pp. 122–133, Mar. 2017.
- [69] W. Li, H. Fan, J. Tang, Q. Wang, X. Zhang, and J. A. El-Awady, “Effects of alloying on deformation twinning in high entropy alloys,” *Mater. Sci. Eng. A*, vol. 763, p. 138143, Aug. 2019.
- [70] S. Fu, H. Bei, Y. Chen, T. K. Liu, D. Yu, and K. An, “Deformation mechanisms and work-hardening behavior of transformation-induced plasticity high entropy alloys by in-situ neutron diffraction,” *Mater. Res. Lett.*, vol. 6, no. 11, pp. 620–626, Nov. 2018.
- [71] J. M. Drapier, D. Coutsouradis, and L. Habraken, “Measurements of stacking-fault energies in Co-Ni and Co-Ni-Cr alloys,” *Acta Metall.*, vol. 15, no. 4, pp. 673–675, Apr. 1967.
- [72] G. N. Irving, J. Stringer, and D. P. Whittle, “Effect of the possible fcc stabilizers Mn, Fe, and Ni on the high-temperature oxidation of Co-Cr alloys,” *Oxid. Met.*, vol. 8, pp. 393–407, Dec. 1974.
- [73] E. H. Köster, A. R. Thölén, and A. Howie, “Stacking fault energies of Ni–Co–Cr alloys,” *Philos. Mag.*, vol. 10, no. 108, pp. 1093–1095, Dec. 1964.
- [74] L. Rémy and A. Pineau, “Twinning and strain-induced f.c.c. → h.c.p. transformation on the mechanical properties of Co-Ni-Cr-Mo alloys,” *Mater. Sci. Eng.*, vol. 26, no. 1, pp. 123–132, Nov. 1976.
- [75] G. C. Soares, M. Patnamsetty, P. Peura, and M. Hokka, “Effects of Adiabatic Heating and Strain Rate on the Dynamic Response of a CoCrFeMnNi High-Entropy Alloy,” *J. Dyn. Behav. Mater.*, vol. 5, pp. 320–330, Sep. 2019.
- [76] M. Shabani, J. Indeck, K. Hazeli, P. D. Jablonski, and G. J. Pataky, “Effect of Strain Rate on the Tensile Behavior of CoCrFeNi and CoCrFeMnNi High-Entropy Alloys,” *J. Mater. Eng. Perform.*, vol. 28, no. 7, pp. 4348–4356, Jul. 2019.
- [77] H. Song *et al.*, “Effects of strain rate on room- and cryogenic-temperature compressive properties in metastable V10Cr10Fe45Co35 high-entropy alloy,” *Sci. Rep.*, vol. 9, no. 1, pp. 1–12, Dec. 2019.

- [78] B. C. De Cooman, Y. Estrin, and S. K. Kim, "Twinning-induced plasticity (TWIP) steels," *Acta Materialia*, vol. 142. Acta Materialia Inc, pp. 283–362, 01-Jan-2018.
- [79] L. Liu, B. He, and M. Huang, "The Role of Transformation-Induced Plasticity in the Development of Advanced High Strength Steels," *Adv. Eng. Mater.*, vol. 20, p. 1701083, Jun. 2018.
- [80] S. S. Hecker, M. G. Stout, K. P. Staudhammer, and J. L. Smith, "Effects of Strain State and Strain Rate on Deformation-Induced Transformation in 304 Stainless Steel: Part I. Magnetic Measurements and Mechanical Behavior," *Metall. Trans. A*, vol. 13, pp. 619–626, Apr. 1982.
- [81] D. T. Pierce, J. A. Jiménez, J. Bentley, D. Raabe, and J. E. Wittig, "The influence of stacking fault energy on the microstructural and strain-hardening evolution of Fe-Mn-Al-Si steels during tensile deformation," *Acta Mater.*, vol. 100, pp. 178–190, 2015.
- [82] O. Bouaziz, H. Zurob, B. Chehab, J. D. Embury, S. Allain, and M. Huang, "Effect of chemical composition on work hardening of Fe-Mn-C TWIP steels," *Mater. Sci. Technol.*, vol. 27, pp. 707–709, Mar. 2011.
- [83] H. J. Lai and C. M. Wan, "The study of work hardening in Fe-Mn-Al-C alloys," *J. Mater. Sci.*, vol. 24, pp. 2449–2453, Jul. 1989.
- [84] J. G. Kim *et al.*, "Superior Strength and Multiple Strengthening Mechanisms in Nanocrystalline TWIP Steel," *Sci. Rep.*, vol. 8, p. 11200, Dec. 2018.
- [85] G. Dirras, D. Tingaud, D. Ueda, A. Hocini, and K. Ameyama, "Dynamic Hall-Petch versus grain-size gradient effects on the mechanical behavior under simple shear loading of β -titanium Ti-25Nb-25Zr alloys," *Mater. Lett.*, vol. 206, pp. 214–216, Nov. 2017.
- [86] I. Gutierrez-Urrutia and D. Raabe, "Dislocation and twin substructure evolution during strain hardening of an Fe-22 wt.% Mn-0.6 wt.% C TWIP steel observed by electron channeling contrast imaging," *Acta Mater.*, vol. 59, no. 16, pp. 6449–6462, Sep. 2011.
- [87] Y. Wu *et al.*, "In-situ neutron diffraction study of deformation behavior of a multi-component high-entropy alloy," *Appl. Phys. Lett.*, vol. 104, no. 5, p. 051910, 2014.
- [88] G. B. Olson and M. Cohen, "Kinetics of strain-induced martensitic nucleation," *Metall. Trans. A*, vol. 6, pp. 791–795, 1975.
- [89] G. B. Olson and M. Cohen, "A mechanism for the strain-induced nucleation of martensitic transformations," *J. Less-Common Met.*, vol. 28, no. 1, pp. 107–118, 1972.
- [90] G. B. Olson and M. Cohen, "A general mechanism of martensitic nucleation: Part I. General concepts and the FCC→HCP transformation," *Metall. Trans. A*, vol. 7A, pp. 1897–1904, Nov. 1976.

- [91] G. B. Olson and M. Cohen, "A general mechanism of martensitic nucleation: Part II. FCC→BCC and other martensitic transformations," *Metall. Trans. A*, vol. 7A, pp. 1905–1914, Nov. 1976.
- [92] J. Dash and H. M. Otte, "The martensite transformation in stainless steel," *Acta Metall.*, vol. 11, no. 10, pp. 1169–1178, 1963.
- [93] P. L. Mangonon and G. Thomas, "The martensite phases in 304 stainless steel," *Metall. Trans.*, vol. 1, pp. 1577–1586, Jun. 1970.
- [94] D. A. Porter, K. E. Easterling, and M. Y. Sherif, *Phase Transformations in Metals and Alloys*, 3rd ed. Taylor and Francis: CRC Press, 2009.
- [95] V. Borovikov, M. I. Mendeleev, A. H. King, and R. LeSar, "Effect of stacking fault energy on mechanism of plastic deformation in nanotwinned FCC metals," *Model. Simul. Mater. Sci. Eng.*, vol. 23, no. 5, p. 055003, May 2015.
- [96] X. X. Wu, X. Y. San, X. G. Liang, Y. L. Gong, and X. K. Zhu, "Effect of stacking fault energy on mechanical behavior of cold-forging Cu and Cu alloys," *Mater. Des.*, vol. 47, pp. 372–376, May 2013.
- [97] J. Liu *et al.*, "Deformation twinning behaviors of the low stacking fault energy high-entropy alloy: An in-situ TEM study," *Scr. Mater.*, vol. 137, pp. 9–12, Aug. 2017.
- [98] I. L. Dillamore, "The stacking fault energy dependence of the mechanisms of deformation in Fcc metals," *Metall. Trans.*, vol. 1, pp. 2463–2470, 1970.
- [99] Y. H. Zhao, Y. T. Zhu, X. Z. Liao, Z. Horita, and T. G. Langdon, "Tailoring stacking fault energy for high ductility and high strength in ultrafine grained Cu and its alloy," *Appl. Phys. Lett.*, vol. 89, no. 12, p. 121906, 2006.
- [100] V. S. Sarma *et al.*, "Role of stacking fault energy in strengthening due to cryo-deformation of FCC metals," *Mater. Sci. Eng. A*, vol. 527, no. 29–30, pp. 7624–7630, Nov. 2010.
- [101] A. Dumay, J. P. Chateau, S. Allain, S. Migot, and O. Bouaziz, "Influence of addition elements on the stacking-fault energy and mechanical properties of an austenitic Fe-Mn-C steel," *Mater. Sci. Eng. A*, vol. 483–484, pp. 184–187, Jun. 2008.
- [102] S. Curtze and V. T. Kuokkala, "Dependence of tensile deformation behavior of TWIP steels on stacking fault energy, temperature and strain rate," *Acta Mater.*, vol. 58, no. 15, pp. 5129–5141, Sep. 2010.
- [103] U. R. Kattner, "THE CALPHAD METHOD AND ITS ROLE IN MATERIAL AND PROCESS DEVELOPMENT," *Tecnol. em Metal. Mater. e Mineração*, vol. 13, no. 1, pp. 3–15, 2016.
- [104] H. Lukas, S. Fries, and B. Sundman, *Computational Thermodynamics: the CALPHAD Method*. Cambridge: Cambridge University Press, 2007.

- [105] Y.-M. Muggianu, M. Gambino, and J.-P. Bros, “Enthalpies de formation des alliages liquides bismuth-étain-gallium à 723 k. Choix d’une représentation analytique des grandeurs d’excès intégrales et partielles de mélange,” *J. Chim. Phys.*, vol. 72, pp. 83–88, 1975.
- [106] A. T. Dinsdale, “SGTE data for pure elements,” *Calphad*, vol. 15, no. 4, pp. 317–425, Oct. 1991.
- [107] T. Sun and K. Fezzaa, “HiSPoD: A program for high-speed polychromatic X-ray diffraction experiments and data analysis on polycrystalline samples,” *J. Synchrotron Radiat.*, vol. 23, pp. 1046–1053, Jul. 2016.
- [108] R. Caciuffo, S. Melone, F. Rustichelli, and A. Boeuf, “Monochromators for x-ray synchrotron radiation,” *Physics Reports*, vol. 152, no. 1. North-Holland, pp. 1–71, 01-Aug-1987.
- [109] I. Inoue *et al.*, “An X-ray harmonic separator for next-generation synchrotron X-ray sources and X-ray free-electron lasers,” *J. Synchrotron Radiat.*, vol. 25, no. 2, pp. 346–353, Mar. 2018.

CHAPTER 2
IDENTIFICATION OF TRIP ALLOYS BY CALPHAD METHODS,
AN ACCESSIBLE APPROACH

This work will be submitted to Metallurgical and Materials Transactions A for publication
J.A. Copley*¹, F.G. Coury², B. Ellyson¹, A.J. Clarke¹

2.1 Abstract

Transformation induced plasticity (TRIP) behavior has been observed in a wide range of materials as a mechanism by which alloys can overcome the strength-ductility tradeoff paradigm. TRIP behavior is predicated on the interplay between phase stability, diffusionless transformation temperatures, and the driving force for a transformation. This work focuses on the use of CALPHAD approaches to predict TRIP behavior by examining thermodynamic factors like the driving force for transformation and the diffusionless transformation temperature, and explores the reasons why this approach fails for certain alloy systems, but shows promise for identifying alloys with the potential to exhibit TRIP behavior in steels and multi-principal element alloys (MPEAs).

2.2 Introduction

Transformation induced plasticity (TRIP) has been used in advanced high strength steels for several decades as a method of overcoming the strength ductility tradeoff [1]–[3]. Recently, TRIP behavior has been found in several classes of Multi-Principal Element Alloys (MPEAs), especially those rich in Co, Cr, or Ni, as well as metastable β -Ti alloys [4]–[9]. This behavior is enabled by a strain-induced martensitic transformation (SIMT), where mechanical strain results in a transformation from a metastable parent phase to a lower energy product phase, which may or may not be the equilibrium phase. In steels, the transformation is generally from an FCC parent phase (austenite) to a BCC or BCT product phase (martensite) [10]–[12]. These phases have given their names to the parent and product phases of all diffusionless transformations (austenite and martensite, respectively). For other materials, the parent and product phases may have different structures. For many TRIP MPEAs, the austenite is FCC and the martensite is

* Corresponding author, email: jacopley@mines.edu

1: Colorado School of Mines, 1500 Illinois St, Golden, CO 80401

2: Federal University of São Carlos, Rod. Washington Luiz, São Carlos - SP, 13565, Brazil

HCP, while β -Ti alloys often transform from BCC to an orthorhombic phase referred to as α'' [13]–[16]. Behaviors like TRIP are beneficial to mechanical performance of alloys, as they result in high work hardening rates, delaying instability, resulting in improved ultimate tensile strength and uniform elongation. Because of this, enabling TRIP has become an attractive goal in alloy design. Approaches for predicting phase stability have been designed, focusing on magnetic and electronic structure for Fe-, Co- and Ni-bearing alloys [17]–[19]. For Ti-alloys, use of electronic factors, such as the mean d orbital energy (Md) and bond order (Bo), have been used as a method for predicting phase stability [20]–[22].

Phase stability may also be predicted using CALPHAD methodologies. CALPHAD, or Calculation of Phase Diagrams, was pioneered in the 1960s and 1970s by Kaufman and Bernstien as a method for determining phase stability in complex systems [23]. These approaches use experimentally based data to build databases of the response of phase stability to alloying and temperature changes. CALPHAD is capable of using known behaviors in systems with few components to predict the behavior in more complex systems [23], [24]. This feature is especially beneficial for systems with a large number of components, as complex systems are experimentally challenging to fully assess for thermodynamic properties.

2.3 Approach

Activating TRIP requires understanding of metastability and consideration of the thermodynamic limitations of martensitic transformations, specifically, the diffusionless transformation temperature, T_0 . T_0 describes the temperature at which two phases of a given composition have the same free energy. T_0 acts as the maximum temperature at which a diffusionless transformation may occur. **Figure 2.1**, on page 26, explores how T_0 may be determined from free energy curves as well as how phase stability affects the compositional dependence of T_0 . The diffusionless transformation temperature is closely related to the free energy of transformation, $\Delta G^{\alpha\rightarrow\beta}$, as T_0 describes the temperature at which $\Delta G^{\alpha\rightarrow\beta} = 0$. Above T_0 , $\Delta G^{\alpha\rightarrow\beta} > 0$, so the transformation is forbidden and below T_0 , $\Delta G^{\alpha\rightarrow\beta} < 0$, so forward progress of the transformation is favorable. Generally, the magnitude of $\Delta G^{\alpha\rightarrow\beta}$ increases further away from T_0 , though this may be a more complicated relationship for compositions with more than one diffusionless transformation temperature. As $\Delta G^{\alpha\rightarrow\beta}$ increases with distance from T_0 , it seems possible that T/T_0 could be used to predict the activation of TRIP behavior in metastable

materials. At low T/T_0 , large energy savings from martensitic transformations are expected, and thus TRIP behavior is favored. In this work, both alloy compositions that experience TRIP behavior and those that do not were pulled from literature and assessed for the relevant thermodynamic considerations, T_0 and $\Delta G^{\alpha\rightarrow\beta}$.

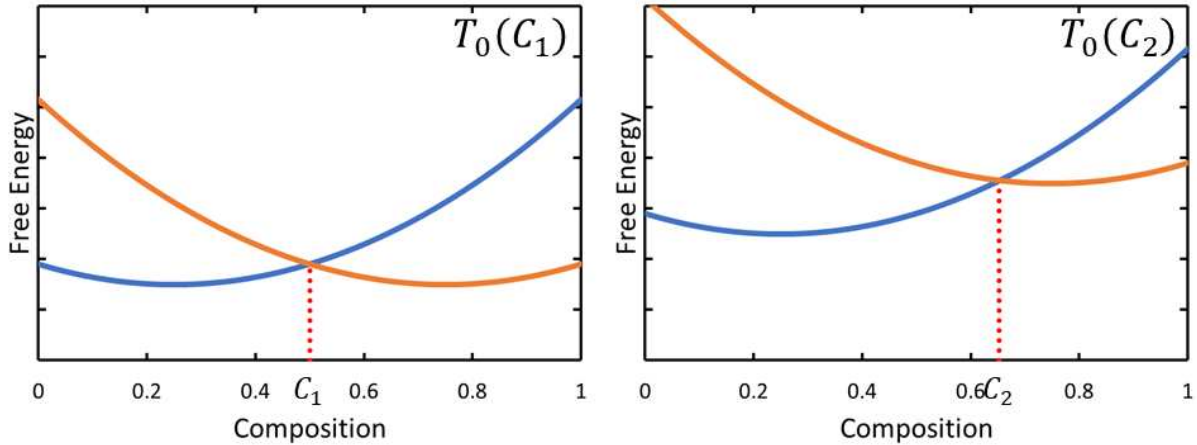


Figure 2.1: Free energy vs. composition curves may be used to define the diffusionless transformation temperature, T_0 , as the temperature at which the free energy curves of two phases intersect above the composition of interest, as illustrated above. T_0 can also be considered the projection of the intersection of two free energy surfaces onto the composition-temperature plane. The relative stability of the phases determines if T_0 increases or decreases with alloying. If the alloying element increases the stability of the high temperature phase, T_0 will decrease with alloying, such that $T_0(C_2) < T_0(C_1)$. If the alloying element increases the stability of the low temperature phase, T_0 will increase with alloying, such that $T_0(C_2) > T_0(C_1)$

2.4 Methods and Results

This work used Thermo-Calc 2020a and the TCHEA3, TCFE9 and TCTI2 databases to assess $\Delta G^{\alpha\rightarrow\beta}$ and T_0 for both TRIP and non-TRIP materials from the literature. For steels and ferrous alloys, the martensite phase often possesses a tetragonal distortion from the cubic ferrite. These results list these transformations as FCC \rightarrow BCC TRIP, as these phases are not individually modelled in the TCFE9 database, instead having a unified phase description. The use of a unified phase description for BCC and BCT presents a challenge for modelling of the diffusionless transformation temperature. In iron and iron based alloys, the BCC phase has both low and high temperature stability [19], [25]. These are referred to as α -ferrite and δ -ferrite, respectively. As a result of the BCC phase's stability at both low and high temperatures in ferrous alloys, there are

2 distinct T_0 values for a given composition. The higher T_0 is associated with the δ -ferrite \rightarrow γ -austenite transition and the lower T_0 is associated with the γ -austenite \rightarrow α -ferrite transition. As TRIP in ferrous alloys is between metastable retained austenite (γ) and martensite modelled as ferrite (α), the lower T_0 is the relevant parameter and was used if multiple T_0 values were found during the CALPHAD modelling. The results of this modelling are listed below, in **Table 2.1.1** and **Table 2.1.2**, which are summarized by **Figure 2.2**, for both FCC \rightarrow BCC TRIP and FCC \rightarrow HCP TRIP.

Table 2.1.1: Alloy and thermodynamic data for steels and FCC \rightarrow BCC MPEAs, including composition (in wt%, unless otherwise noted), TRIP behavior, testing temperature, diffusionless transformation temperature, normalized testing temperature, driving force for the transformation and reference. The BCC phase is used to describe both BCC and BCT martensite.

| Alloy | TRIP | Temp. (°C) | T_0 (K) | T/T_0 | $\Delta G^{\alpha \rightarrow \beta}$ ($\frac{J}{mol}$) | Ref. |
|--|------|---------------|-----------|---------|---|------|
| Fe-0.59C-22.26Mn-0.27V | N | -150 | 256.9 | 0.48 | -344.9 | [27] |
| Fe-0.59C-22.26Mn-0.27V | N | 25 | 256.9 | 1.16 | 153.5 | [27] |
| Fe-0.59C-22.26Mn-0.27V | N | 250 | 256.9 | 1.65 | 779.9 | [27] |
| Fe-0.59C-22.26Mn-0.27V | N | 400 | 256.9 | 2.62 | 1722.8 | [27] |
| Fe-12Cr-9Ni-2Mo-0.7Al-0.3Ti-0.02C | Y | 25 | 892.6 | 0.33 | -3455.7 | [28] |
| Fe-12Cr-9Ni-2Mo-0.7Al-0.3Ti-0.02C | Y | 180 | 892.6 | 0.51 | -2326.8 | [28] |
| Fe-15.5Cr-6.1Mn-6.1Ni-1Si-0.14Al-0.03C | Y | -100 | 731.8 | 0.24 | -3354.9 | [29] |
| Fe-15.5Cr-6.1Mn-6.1Ni-1Si-0.14Al-0.03C | Y | -50 | 731.8 | 0.30 | -2981.3 | [29] |
| Fe-15.5Cr-6.1Mn-6.1Ni-1Si-0.14Al-0.03C | Y | 0 | 731.8 | 0.37 | -2608.7 | [29] |
| Fe-15.5Cr-6.1Mn-6.1Ni-1Si-0.14Al-0.03C | Y | 125 | 731.8 | 0.55 | -1740.7 | [29] |
| Fe-15.5Cr-6.1Mn-6.1Ni-1Si-0.14Al-0.03C | Y | 175 | 731.8 | 0.61 | -1432.9 | [29] |
| Fe-15.5Cr-6.1Mn-6.1Ni-1Si-0.14Al-0.03C | N | 225 | 731.8 | 0.68 | -1137.0 | [29] |
| Fe-18Cr-8Ni-0.04C | Y | 25 | 876.3 | 0.34 | -3283.3 | [30] |
| Fe-18Cr-8Ni-0.08C | Y | 25 | 862.5 | 0.35 | -3219.8 | [26] |
| Fe-18Cr-8Ni-0.04C | Y | 50 | 876.3 | 0.37 | -3123.3 | [30] |
| Fe-18Cr-8Ni-0.04C | Y | 75 | 876.3 | 0.40 | -2913.6 | [30] |
| Fe-18Cr-8Ni-0.04C | Y | 100 | 876.3 | 0.43 | -2738.3 | [30] |
| Fe-18Cr-8Ni-0.04C | Y | 125 | 876.3 | 0.45 | -2561.5 | [30] |
| Fe-18Cr-8Ni-0.04C | N | 150 | 876.3 | 0.48 | -2404.1 | [30] |
| Fe-18Cr-8Ni-0.04C | N | 175 | 876.3 | 0.51 | -2243.0 | [30] |
| Fe-21Mn-2.70Si-1.6Al-0.1Cr-0.11C | Y | 25 | 495.3 | 0.60 | -1112.7 | [31] |
| Fe-21Mn-2.70Si-1.6Al-0.1Cr-0.11C | Y | 100 | 495.3 | 0.75 | -670.0 | [31] |
| Fe-21Mn-2.70Si-1.6Al-0.1Cr-0.11C | Y | 150 | 495.3 | 0.85 | -382.7 | [31] |
| Fe-21Mn-2.70Si-1.6Al-0.1Cr-0.11C | N | 200 | 495.3 | 0.96 | -112.5 | [31] |
| Fe-21Mn-2.70Si-1.6Al-0.1Cr-0.11C | N | 300 | 495.3 | 1.16 | 345.4 | [31] |

Table 2.1.1 Con't: Alloy and thermodynamic data for steels and FCC→BCC MPEAs, including composition (in wt%, unless otherwise noted), TRIP behavior, testing temperature, diffusionless transformation temperature, normalized testing temperature, driving force for the transformation and reference.

| Alloy | TRIP | Temp. (°C) | T_0 (K) | T/T_0 | $\Delta G^{\alpha \rightarrow \beta}$ ($\frac{J}{mol}$) | Ref. |
|----------------------------------|------|------------|-----------|---------|---|------|
| Fe-21Mn-2.70Si-1.6Al-0.1Cr-0.11C | N | 400 | 495.3 | 1.36 | 623.5 | [31] |
| Fe-22.5Ni-0.32C | Y | -200 | 429.9 | 0.17 | -520.2 | [32] |
| Fe-22.5Ni-0.32C | Y | -100 | 429.9 | 0.40 | -1568.0 | [32] |
| Fe-22.5Ni-0.32C | Y | 0 | 429.9 | 0.64 | -993.5 | [32] |
| Fe-22.5Ni-0.32C | Y | 50 | 429.9 | 0.75 | -684.4 | [32] |
| Fe-25Ni-0.37C | Y | 0 | 305.9 | 0.89 | -149.8 | [32] |
| Fe-22.5Ni-0.32C | N | 100 | 429.9 | 0.87 | -346.9 | [32] |
| Fe-22.5Ni-0.32C | N | 200 | 429.9 | 1.10 | 244.6 | [32] |
| Fe-25Ni-0.37C | N | 100 | 305.9 | 1.22 | 297.5 | [32] |
| Fe-25Ni-0.37C | N | 200 | 305.9 | 1.55 | 800.6 | [32] |
| Fe-25Ni-0.37C | Y | -200 | 305.9 | 0.24 | -1096.6 | [32] |
| Fe-25Ni-0.37C | Y | -100 | 305.9 | 0.57 | -659.9 | [32] |
| Fe-25Ni-0.37C | Y | 50 | 305.9 | 1.06 | 75.7 | [32] |
| Fe-30Mn-10Cr-10Co-0.56C (at%) | Y | 25 | 331.2 | 0.90 | -100.0 | [33] |
| Fe-30Ni-0.23C | Y | -200 | 130.3 | 0.56 | -246.5 | [32] |
| Fe-30Ni-0.23C | Y | -100 | 130.3 | 1.33 | 236.0 | [32] |
| Fe-30Ni-0.23C | Y | -40 | 130.3 | 1.79 | 564.4 | [32] |
| Fe-30Ni-0.23C | N | 0 | 130.3 | 2.10 | 752.3 | [32] |
| Fe-30Ni-0.23C | N | 100 | 130.3 | 2.86 | 1067.6 | [32] |
| Fe-30Ni-0.23C | N | 200 | 130.3 | 3.63 | 1353.0 | [32] |
| Fe-31Ni | Y | -200 | 239.3 | 0.31 | -921.8 | [32] |
| Fe-31Ni | Y | -100 | 239.3 | 0.72 | -393.4 | [32] |
| Fe-31Ni | Y | -40 | 239.3 | 0.97 | -34.2 | [32] |
| Fe-31Ni | N | 0 | 239.3 | 1.14 | 174.7 | [32] |
| Fe-31Ni | N | 100 | 239.3 | 1.56 | 548.0 | [32] |
| Fe-31Ni | N | 200 | 239.3 | 1.98 | 916.4 | [32] |
| Fe-8Mn-10Cr-5Ni-0.1C | y | 25 | 678.6 | 0.44 | -2311.8 | [34] |
| Fe-22Mn-3Al-3Si | Y | 25 | 532.0 | 0.56 | -1230.6 | [35] |
| Fe-25Mn-3Al-3Si | Y | 25 | 448.0 | 0.67 | -757.0 | [35] |
| Fe-28Mn-3Al-3Si | N | 25 | 364.4 | 0.82 | -307.6 | [35] |
| Fe-Mn28.5-Co11.1-Cr9.77-Cu0.33 | Y | 25 | 387.0 | 0.77 | -15989.1 | [5] |
| Fe-10V-10Cr-30Co5Ni (at%) | Y | -196 | 925.7 | 0.08 | -6690.3 | [36] |
| Fe-10V-10Cr-35Co (at%) | Y | 25 | 1024.0 | 0.29 | -5534.5 | [36] |
| Fe-10V-10Cr-35Co (at%) | Y | -196 | 1024.0 | 0.08 | -7862.5 | [36] |

Table 2.1.2: Alloy and thermodynamic data for FCC→HCP MPEAs, including composition (in wt%, unless otherwise noted), TRIP behavior, testing temperature, diffusionless transformation temperature, normalized testing temperature, driving force for the transformation and reference.

| Alloy | TRIP | Temp. (°C) | T_0 (K) | T/T_0 | $\Delta G^{\alpha\rightarrow\beta}$ ($\frac{J}{mol}$) | Ref. |
|---|------|------------|-----------|----------|---|------|
| Co-10Cr-35Fe-45Mn (at%) | N | 25 | 12.1 | 24.75 | 522.4 | [37] |
| Co-10Cr-40Fe-40Mn (at%) | N | 25 | 0.0 | ∞ | 521.5 | [37] |
| Co-23.3Cr-23.3Fe-23.3Ni-6.8Al (at%) | N | 25 | 0.0 | ∞ | 3295.8 | [37] |
| Co-23.6Cr-23.6Fe-23.6Ni-5.6Mo (at%) | N | 25 | 0.0 | ∞ | 863.8 | [38] |
| Co-24.3Cr-24.3Fe-24.3Ni-2.8Al (at%) | N | 25 | 0.0 | ∞ | 2020.7 | [37] |
| Co-24.4Ni-24.4Fe-24.4Cr-2.44Al ₂ (at%) | N | 25 | 0.0 | ∞ | 1898.3 | [39] |
| Co-25Cr-20Fe-25Ni (at%) | N | 25 | 0.0 | ∞ | 889.0 | [37] |
| Co-40Cr-30Ni (at%) | N | 25 | 0.0 | ∞ | 997.1 | [40] |
| Co-20Cr-15Mn-15Fe-15Ni (at%) | N | 25 | 165.4 | 1.80 | 272.4 | [41] |
| Co-25Cr-15Fe-25Ni (at%) | N | 25 | 72.1 | 4.17 | 687.9 | [37] |
| Co-25Cr-35Fe-5Ni (at%) | Y | 25 | 438.8 | 0.68 | -379.8 | [37] |
| Co-25Cr-40Fe (at%) | Y | 25 | 474.5 | 0.63 | -480.8 | [37] |
| Co-25Cr-15Mn-15Ni-10Fe (at%) | Y | 25 | 332.5 | 0.90 | -11.2 | [41] |
| Co-40Cr-20Ni (at%) | Y | 25 | 679.9 | 0.44 | -916.8 | [40] |
| Co-40Cr-10Ni (at%) | Y | 25 | 1137.5 | 0.26 | -2066.0 | [40] |
| Co-40Cr-5Ni (at%) | Y | -100 | 1240.0 | 0.14 | -2691.8 | [40] |
| Co-40Cr-5Ni (at%) | Y | 60 | 1240.0 | 0.27 | -2288.1 | [40] |
| Co-40Cr-5Ni (at%) | Y | 300 | 1240.0 | 0.46 | -1682.5 | [40] |
| Co-40Cr-5Ni (at%) | Y | 450 | 1240.0 | 0.58 | -1304.0 | [40] |
| Co-40Cr-5Ni (at%) | Y | 600 | 1240.0 | 0.70 | -925.6 | [40] |
| Co-40Cr-5Ni (at%) | Y | 750 | 1240.0 | 0.83 | -547.1 | [40] |
| Co-40Cr-5Ni (at%) | N | 900 | 1240.0 | 0.95 | -168.6 | [40] |
| Co-33Cr-33Ni (at%) | N | 25 | 0.0 | ∞ | 1399.8 | [42] |
| Fe-40Mn-10Co-10Cr (at%) | N | 25 | 0.0 | ∞ | 521.6 | [7] |
| Fe-25Co-25Cr-25Ni (at%) | N | -196 | 0.0 | ∞ | 493.7 | [43] |
| Fe-25Co-25Cr-25Ni (at%) | N | 25 | 0.0 | ∞ | 1069.8 | [43] |
| Fe-20Mn-20Co-20Cr-20Ni (at%) | N | 25 | 0.0 | ∞ | 1046.9 | [42] |
| Fe-25Ni-10V-10Cr-10Co (at%) | N | 25 | 162.0 | 1.84 | 2448.9 | [36] |

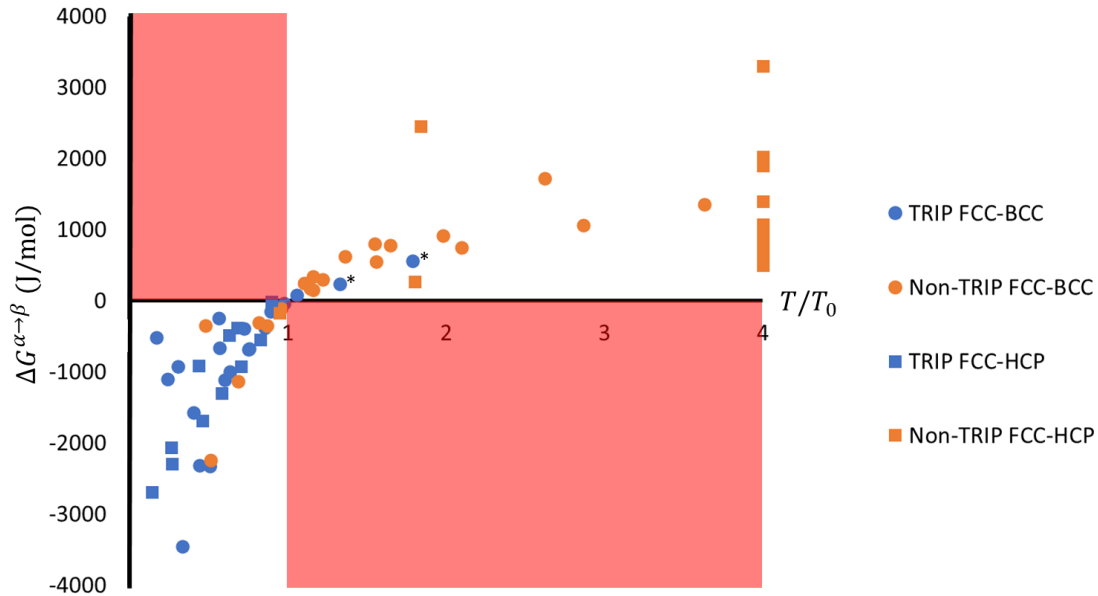


Figure 2.2: Plot of $\Delta G^{\alpha \rightarrow \beta}$ and T_0 for both TRIP and non-TRIP MPEAs and ferrous alloys. These data are distinguished based on their martensite phase as either BCC or HCP. All alloys shown here have an FCC parent austenite phase. The regions colored in red demark combinations of T_0 and $\Delta G^{\alpha \rightarrow \beta}$ which are not feasible for the case of α being the high temperature phase and β the martensitic phase. The TRIP enabled alloys are marked in blue and the non-TRIP alloys in orange. For $T/T_0 > 4$, T/T_0 is plotted as 4 for spacing. The results show clearly that these factors can be used to roughly group TRIP and non-TRIP alloys. The TRIP data that are shown above $T/T_0 = 1$ are marked with an “*”. These points are associated with TRIP behavior at cryogenic temperatures, and the predicted T_0 is well below room temperature. At these temperatures, accurate thermodynamic data, especially regarding the relative energies of non-equilibrium phases is difficult to generate.

Steels and MPEAs are not the only materials for which TRIP results in desirable mechanical properties. Metastable β -titanium alloys have also exhibited this behavior and are of particular interest in applications where specific strength and light-weighting are important. These alloys transform from a metastable BCC phase (β -Ti) to either an HCP martensite (α') or an orthorhombic martensite (α''). As with the martensite in ferrous materials, the α' and α'' phases are not modeled independently of the low temperature HCP (α) phase and have a unified description. Results from a similar analysis on Ti-alloys, as was performed on the steels and MPEAs shown in **Figure 2.2**, are listed in **Table 2.2** and shown in **Figure 2.3**.

Table 2.1.3: Alloy and thermodynamic data for BCC→HCP Ti-based alloys, including composition (in wt%, unless otherwise noted), TRIP behavior, testing temperature, diffusionless transformation temperature, normalized testing temperature, driving force for the transformation and reference. The HCP phase is used to describe both α' and α'' martensites.

| Alloy | TRIP | Temp. (°C) | T_0 (K) | T/T_0 | $\Delta G^{\alpha \rightarrow \beta}$ $\left(\frac{J}{mol}\right)$ | Ref. |
|-----------------------------------|------|------------|-----------|---------|--|------|
| Ti-10Mo | Y | 25 | 785.5 | 0.38 | -2635.5 | [44] |
| Ti-10Mo-1Fe | N | 25 | 698.3 | 0.43 | -2117.4 | [45] |
| Ti-10Mo-3Fe | N | 25 | 304.9 | 0.98 | -31.4 | [46] |
| Ti-10Mo-5Fe | N | 25 | 513.1 | 0.58 | -1075.9 | [47] |
| Ti-10V-3Fe-3Al | Y | 25 | 645.3 | 0.46 | -1410.9 | [8] |
| Ti-10V-1Fe-3Al | Y | 25 | 833.4 | 0.36 | -2281.7 | [48] |
| Ti-10V-2Cr-3Al | Y | 25 | 844.7 | 0.35 | -2319.9 | [48] |
| Ti-11.5Mo-6Zr-4.5Sn | N | 25 | 494.0 | 0.60 | -1038.0 | [49] |
| Ti-12Mo | Y | 25 | 713.7 | 0.42 | -2240.8 | [50] |
| Ti-12Mo-6Zr-2Fe | N | 25 | 469.9 | 0.63 | -855.7 | [22] |
| Ti-13Mo | Y | 25 | 677.7 | 0.44 | -2042.4 | [13] |
| Ti-13V (at%) | Y | 25 | 683.4 | 0.44 | -1721.7 | [51] |
| Ti-13V-11Cr | N | 25 | 116.5 | 2.56 | 725.2 | [15] |
| Ti-14Mo | N | 25 | 641.7 | 0.46 | -1843.2 | [50] |
| Ti-15Mo | N | 25 | 605.6 | 0.49 | -1643.4 | [44] |
| Ti-15Mo-5Zr | N | 25 | 562.9 | 0.53 | -1396.9 | [49] |
| Ti-16V-2Fe | N | 25 | 471.7 | 0.63 | -712.8 | [52] |
| Ti-16V-2Fe-2Al | N | 25 | 489.6 | 0.61 | -748.3 | [52] |
| Ti-20v-3Sn | N | 25 | 459.6 | 0.65 | -627.1 | [49] |
| Ti-20V-6Al | N | 25 | 682.0 | 0.44 | -1321.7 | [49] |
| Ti-20Zr-20Hf-20Nb-20Ta (at%) | N | 25 | 56.4 | 4.00 | 1564.7 | [53] |
| Ti-22V | N | 25 | 432.3 | 0.69 | -535.3 | [54] |
| Ti-25Ta-30Nb | N | 25 | 185.0 | 1.61 | 498.4 | [14] |
| Ti-27.5Zr-27.5Hf-27.5Nb-5Ta (at%) | Y | 25 | 818.8 | 0.36 | -2795.1 | [53] |
| Ti-28V | N | 25 | 164.2 | 1.82 | 405.0 | [54] |
| Ti-32Nb | Y | 25 | 536.0 | 0.56 | -1146.9 | [16] |
| Ti-35Nb | Y | 25 | 462.2 | 0.65 | -774.5 | [55] |
| Ti-3Al-5Mo-7V-3Cr | Y | 25 | 642.5 | 0.46 | -1485.4 | [56] |
| Ti-43Nb | N | 25 | 233.3 | 1.28 | 270.9 | [16] |
| Ti-5Al-5Mo-5V-3Cr | Y | 25 | 763.3 | 0.39 | -1959.6 | [57] |
| Ti-62Ta-2Nb | Y | 25 | 407.7 | 0.73 | -670.0 | [58] |
| Ti-8.5Cr-1.5Sn | Y | 25 | 712.7 | 0.42 | -2021.3 | [9] |
| Ti-8Mo-4Nb-2V-3Al | Y | 25 | 680.0 | 0.44 | -1784.4 | [59] |

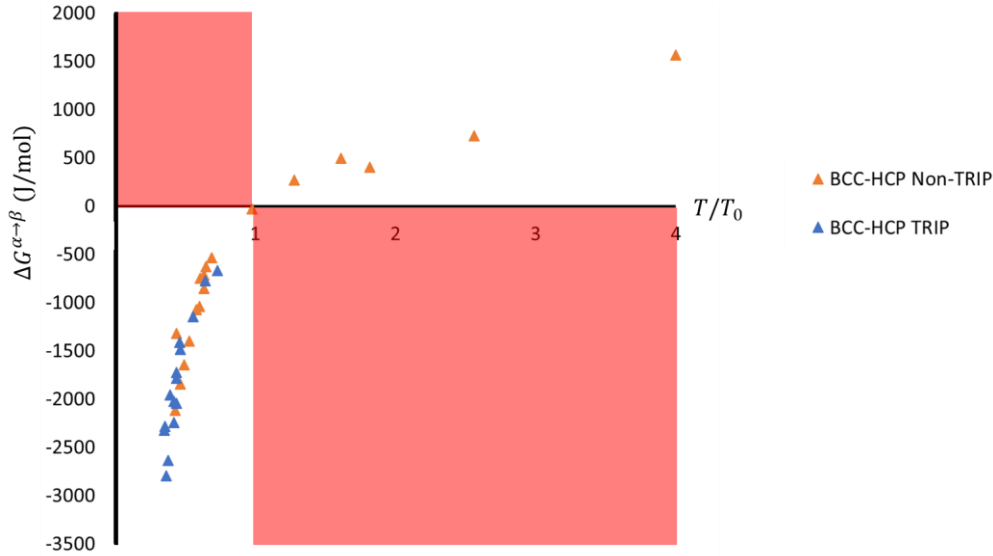


Figure 2.3: Plot of $\Delta G^{\alpha \rightarrow \beta}$ and T_0 for both TRIP and non-TRIP Ti-alloys. The HCP phase listed as the martensite represents both the HCP martensite (α') and the orthorhombic martensite (α''), as these share a unified phase description in the TCTI2 Thermo-Calc databases. There are no easily demarked regions of TRIP and TWIP behavior, instead, the non-TRIP behavior continues to follow the TRIP behavior to well below $T/T_0 = 1$. The regions colored in red demark combinations of T_0 and $\Delta G^{\alpha \rightarrow \beta}$ which are not feasible for the case of α being the high temperature phase and β the martensitic phase. The TRIP enabled alloys are marked in blue and the non-TRIP alloys in orange. For $T/T_0 > 4$, T/T_0 is plotted as 4 for spacing.

2.5 Discussion

The results for FCC \rightarrow BCC and FCC \rightarrow HCP alloys are promising. While some data points associated with non-TRIP behavior exist below $T/T_0 = 1$, the majority of plotted data are consistent with TRIP occurring below $T/T_0 = 1$, with increasing chance of TRIP behavior occurring with progressively lower T/T_0 and non-TRIP behavior occurring primarily above $T/T_0 = 1$. The relative frequency of TRIP behavior as compared to non-TRIP behavior below $T/T_0 = 1$ suggests a thermodynamic assessment of T_0 and $\Delta G^{\alpha \rightarrow \beta}$ may be a viable method for rapid assessment of TRIP potential. Assessing an alloy's ability to experience TRIP using only readily accessed thermodynamic parameters could be especially useful for some MPEAs, such as those based upon the 3d transition metals, which have a vast and relatively unexplored design space, but which may be modeled by CALPHAD techniques that extend knowledge of phase stability in few component systems to higher component systems. As a comparison between

$\Delta G^{\alpha \rightarrow \beta}$ and T/T_0 for effectiveness, both have equivalent effectiveness; however, from a design point-of-view, T_0 has the advantage of being universal to an alloy, regardless of temperature, while $\Delta G^{\alpha \rightarrow \beta}$ must be calculated for each temperature. When selecting a fraction of T_0 as a cutoff for determining TRIP potential, several values of T/T_0 seem to stand out. Below $T/T_0 = 0.45$, only TRIP behavior was observed. However, the exact location of this cutoff may be an effect of sampling, as few points exist below this T/T_0 level. Below $T/T_0 = 0.8$, TRIP is observed in 89% of tested alloys and temperatures, which is an improvement over considering all $T/T_0 < 1$, where only 83% of tested alloys and compositions exhibit TRIP behavior. For a simple model such as this, which considers only thermodynamic factors, these are encouraging results.

The extension of this method to Ti-containing alloys was less successful, with no meaningful distinctions between the TRIP and non-TRIP data being made on the $\Delta G^{\alpha \rightarrow \beta}$ vs. T/T_0 plots. This suggests other factors, beyond thermodynamics, are determining the TRIP behavior in Ti alloys. This is supported by work performed by Ahmed *et al.* that examined the effect of strain rate on the activation of TRIP behavior in a Ti-10V-3Fe-3Al alloy [8]. It was found that strain rate played a significant role in the activation of TRIP, with high strain rates acting to suppress TRIP behavior. While similar effects were seen in 304 steel performed by Hecker *et al.*, the suppression of TRIP in 304 was ascribed to the adiabatic heating associated with high strain rate tests, and thus a thermodynamic concern [26]. In the Ti-10V-3Fe-3Al alloy, while adiabatic heating may play a role in the suppression of $\beta \rightarrow \alpha''$ TRIP, other effects of strain rate, including the presence of athermal ω -phase and interface mobility, both strongly strain rate dependent, are believed to have also contributed to the reduction of TRIP behavior. The inability of a pure thermodynamics approach to accurately identify TRIP capable alloys indicates that kinetic considerations are important for determining the activation of TRIP in Ti-alloys.

2.6 Conclusions

A method to predict TRIP behavior in alloys using only thermodynamic factors easily accessed by the use of CALPHAD methodologies was explored using Thermo-Calc software for Fe- and Ti-based alloys, as well as MPEAs. The results showed that for prediction of FCC \rightarrow BCC and FCC \rightarrow HCP TRIP behavior, thermodynamic parameters like the diffusionless

transformation temperature and the driving force of the transformation are largely sufficient to predict if TRIP will occur in a material, with large $\Delta G^{\alpha \rightarrow \beta}$ and low T/T_0 corresponding to increased probability of TRIP. In Ti-based alloys, however, these factors were not adequate predictors of TRIP behavior, and it is believed that kinetic concerns dominate thermodynamic concerns in governing the activation of TRIP behavior.

2.8 Supplemental Materials

Below is included the Thermo-Calc code used to model T_0 , G^α , and G^β :

```
go data
```

```
sw tcti2
```

@@ The selected database should be chosen based on the database with the best evaluation of the composition of interest. Information about the assessment of databases is provided by Thermo-Calc online.

```
def-sys ti v al
```

@@ All components of the material of interest must be listed here

```
get
```

@@ this retrieves all relevant phase descriptions. No calculations may be performed without this step. Some versions of Thermo-Calc will generate a warning if this function is not performed when switching to Poly-3

```
go poly
```

@@ short for go_to_module poly-3, this switches to the module of Thermo-Calc designed for calculations and computing equilibrium

```
set-cond T=300 n=1 p=100000
```

@@ these set the conditions for the calulted equilibrium.

```
set-cond w(v)=0.20
```

```
set-cond w(al)=0.06
```

@@ these determine the alloy composition. There must be n-1 of these, where n is the number of components in the alloy of interest. w(A) represents the weight fraction of component A. x(A) represents the molar or atomic fraction of component A

```
c-e
```

@@ this computes an initial equilibrium

adv t-zero bcc-b2 hcp-a3

@@ This generates the t-zero temperature of the selected alloy for the selected phases

@@below is code for generating the free energies fo the phases of interest

set-cond T=2000

@@a high temperature ensures a single phase solid solution is formed in the next step, rather multiple of the same phase with different compoitions (miscibility gaps)

change-status

phase

*

suspend

@@this removes from consideration for equilibrium all of the phases

change-status

phase

BCC-B2

entered

0

@@this restores only one phase, select either the martensite or austenite

c-e

l-e

screen

vwcs

@@list-equilibrium shows the equilibrium calculated. Check to make sure the system is single phase and has the phase of interest

adv show 298.15 g

@@this generates the free energy of the desired phase at the selected temperature and displays in units of joules/mol

@@the below code repeats this process for the other phase of interest

change-status

phase

*

suspend

change-status

phase

hcp-a3

entered

0

c-e

l-e

screen

vwcs

adv show 298.15 g

References

- [1] L. Liu, B. He, and M. Huang, “The Role of Transformation-Induced Plasticity in the Development of Advanced High Strength Steels,” *Adv. Eng. Mater.*, vol. 20, p. 1701083, Jun. 2018.
- [2] S. Yan, T. Liang, Z. Wang, B. Yan, T. Li, and X. Liu, “Novel 1.4 GPa-strength medium-Mn steel with uncompromised high ductility,” *Mater. Sci. Eng. A*, vol. 773, p. 138732, Jan. 2020.
- [3] S. S. Sohn, H. Song, M. C. Jo, T. Song, H. S. Kim, and S. Lee, “Novel 1.5 GPa-strength with 50%-ductility by transformation-induced plasticity of non-recrystallized austenite in duplex steels,” *Sci. Rep.*, vol. 7, p. 1255, Dec. 2017.
- [4] F. G. Coury *et al.*, “Design and in-situ characterization of a strong and ductile co-rich multicomponent alloy with transformation induced plasticity,” *Scr. Mater.*, vol. 173, 2019.
- [5] Z. Li, C. C. Tasan, K. G. Pradeep, and D. Raabe, “A TRIP-assisted dual-phase high-entropy alloy: Grain size and phase fraction effects on deformation behavior,” *Acta Mater.*, vol. 131, pp. 323–335, Jun. 2017.
- [6] Z. Li, K. G. Pradeep, Y. Deng, D. Raabe, and C. C. Tasan, “Metastable high-entropy dual-phase alloys overcome the strength-ductility trade-off,” *Nature*, vol. 534, pp. 227–230, May 2016.
- [7] Y. Deng, C. C. Tasan, K. G. Pradeep, H. Springer, A. Kostka, and D. Raabe, “Design of a twinning-induced plasticity high entropy alloy,” *Acta Mater.*, vol. 94, pp. 124–133, May 2015.
- [8] M. Ahmed, D. Wexler, G. Casillas, D. G. Savvakina, and E. V. Pereloma, “Strain rate dependence of deformation-induced transformation and twinning in a metastable titanium alloy,” *Acta Mater.*, vol. 104, pp. 190–200, Feb. 2016.

- [9] C. Brozek *et al.*, “A β -titanium alloy with extra high strain-hardening rate: Design and mechanical properties,” *Scr. Mater.*, vol. 114, pp. 60–64, Mar. 2016.
- [10] J. A. Venables, “The martensite transformation in stainless steel,” *Philos. Mag.*, vol. 7, no. 73, pp. 35–44, 1962.
- [11] G. B. Olson and M. Cohen, “A general mechanism of martensitic nucleation: Part II. FCC→BCC and other martensitic transformations,” *Metall. Trans. A*, vol. 7A, pp. 1905–1914, Nov. 1976.
- [12] G. B. Olson and M. Cohen, “A general mechanism of martensitic nucleation: Part I. General concepts and the FCC→HCP transformation,” *Metall. Trans. A*, vol. 7A, pp. 1897–1904, Nov. 1976.
- [13] M. K. Koul and J. F. Breedis, “Phase transformations in beta isomorphous titanium alloys,” *Acta Metall.*, vol. 18, no. 6, pp. 579–588, Jun. 1970.
- [14] E. Bertrand, “Elaboration et caractérisation d’alliages biocompatibles Ti-Ta-Nb présentant des propriétés superélastiques et à mémoire de forme,” INSA de Rennes, Nov. 2011.
- [15] G. H. Narayanan and T. F. Archbold, “Decomposition of the metastable beta phase in the all-beta alloy Ti-13V-11Cr-3Al,” *Metall. Trans.*, vol. 1, pp. 2281–2290, Aug. 1970.
- [16] H. Y. Kim and S. Miyazaki, “Martensitic Transformation and Superelastic Properties of Ti-Nb Base Alloys,” *Mater. Trans.*, vol. 56, no. 5, pp. 625–634, May 2015.
- [17] Z. Yang *et al.*, “Designing transformation-induced plasticity and twinning-induced plasticity Cr-Co-Ni medium entropy alloys: theory and experiment,” Elsevier BV, Feb. 2020.
- [18] D. Ma, B. Grabowski, F. Körmann, J. Neugebauer, and D. Raabe, “Ab initio thermodynamics of the CoCrFeMnNi high entropy alloy: Importance of entropy contributions beyond the configurational one,” *Acta Mater.*, vol. 100, pp. 90–97, Nov. 2015.
- [19] T. B. Massalski and D. E. Laughlin, “The surprising role of magnetism on the phase stability of Fe (Ferro),” *Calphad Comput. Coupling Phase Diagrams Thermochem.*, vol. 33, pp. 3–7, Mar. 2009.
- [20] M. Morinaga, Y. Murata, and H. Yukawa, “Molecular orbital approach to alloy design,” in *Applied Computational Materials Modeling*, Springer US, 2007, pp. 255–306.
- [21] M. Morinaga, “The molecular orbital approach and its application to biomedical titanium alloy design,” in *Titanium in Medical and Dental Applications*, Elsevier, 2018, pp. 39–64.
- [22] D. Kuroda, M. Niinomi, M. Morinaga, Y. Kato, and T. Yashiro, “Design and mechanical properties of new β type titanium alloys for implant materials,” *Mater. Sci. Eng. A*, vol. 243, no. 1–2, pp. 244–249, Mar. 1998.
- [23] U. R. Kattner, “THE CALPHAD METHOD AND ITS ROLE IN MATERIAL AND PROCESS DEVELOPMENT,” *Tecnol. em Metal. Mater. e Mineração*, vol. 13, no. 1, pp. 3–15, 2016.

- [24] Y.-M. Muggianu, M. Gambino, and J.-P. Bros, “Enthalpies de formation des alliages liquides bismuth-étain-gallium à 723 k. Choix d’une représentation analytique des grandeurs d’excès intégrales et partielles de mélange,” *J. Chim. Phys.*, vol. 72, pp. 83–88, 1975.
- [25] D. E. Laughlin, “The β Iron Controversy Revisited,” *J. Phase Equilibria Diffus.*, vol. 39, pp. 274–279, Jun. 2018.
- [26] S. S. Hecker, M. G. Stout, K. P. Staudhammer, and J. L. Smith, “Effects of Strain State and Strain Rate on Deformation-Induced Transformation in 304 Stainless Steel: Part I. Magnetic Measurements and Mechanical Behavior,” *Metall. Trans. A*, vol. 13, pp. 619–626, Apr. 1982.
- [27] M. Madivala, A. Schwedt, S. L. Wong, F. Roters, U. Prah, and W. Bleck, “Temperature dependent strain hardening and fracture behavior of TWIP steel,” *Int. J. Plast.*, vol. 104, pp. 80–103, May 2018.
- [28] F. D. Fischer, G. Reisner, E. Werner, K. Tanaka, G. Cailletaud, and T. Antretter, “New view on transformation induced plasticity (TRIP),” *Int. J. Plast.*, vol. 16, no. 7–8, pp. 723–748, Jun. 2000.
- [29] S. Martin, S. Wolf, U. Martin, L. Krüger, and D. Rafaja, “Deformation Mechanisms in Austenitic TRIP/TWIP Steel as a Function of Temperature,” *Metall. Mater. Trans. A Phys. Metall. Mater. Sci.*, vol. 47, no. 1, pp. 49–58, Jan. 2016.
- [30] G. C. Soares, M. C. M. Rodrigues, and L. De Arruda Santos, “Influence of temperature on mechanical properties, fracture morphology and strain hardening behavior of a 304 stainless steel,” in *Materials Research*, 2017, vol. 20, pp. 141–151.
- [31] M. Eskandari, A. Zarei-Hanzaki, and A. Marandi, “An investigation into the mechanical behavior of a new transformation-twinning induced plasticity steel,” *Mater. Des.*, vol. 39, pp. 279–284, Aug. 2012.
- [32] I. Tamura, “Deformation-induced martensitic transformation and transformation-induced plasticity in steels,” *Met. Sci.*, vol. 16, no. 5, pp. 245–253, May 1982.
- [33] Z. Li, C. C. Tasan, H. Springer, B. Gault, and D. Raabe, “Interstitial atoms enable joint twinning and transformation induced plasticity in strong and ductile high-entropy alloys,” *Sci. Rep.*, vol. 7, p. 40704, Dec. 2017.
- [34] T. Furukawa, H. Huang, and O. Matsumura, “Effects of carbon content on mechanical properties of 5%Mn steels exhibiting transformation induced plasticity,” *Mater. Sci. Technol.*, vol. 10, no. 11, pp. 964–970, Jan. 1994.
- [35] D. T. Pierce, J. A. Jiménez, J. Bentley, D. Raabe, and J. E. Wittig, “The influence of stacking fault energy on the microstructural and strain-hardening evolution of Fe-Mn-Al-Si steels during tensile deformation,” *Acta Mater.*, vol. 100, pp. 178–190, 2015.

- [36] Y. H. Jo *et al.*, “FCC to BCC transformation-induced plasticity based on thermodynamic phase stability in novel V10Cr10Fe45Co_xNi35-x medium-entropy alloys,” *Sci. Rep.*, vol. 9, p. 2948, Dec. 2019.
- [37] W. Fang *et al.*, “Transformation Induced Plasticity Effects of a Non-Equal Molar Co-Cr-Fe-Ni High Entropy Alloy System,” *Metals (Basel)*, vol. 8, no. 5, p. 369, May 2018.
- [38] B. Cai *et al.*, “Deformation mechanisms of Mo alloyed FeCoCrNi high entropy alloy: In situ neutron diffraction,” *Acta Mater.*, vol. 127, pp. 471–480, Apr. 2017.
- [39] J. Liu *et al.*, “Deformation twinning behaviors of the low stacking fault energy high-entropy alloy: An in-situ TEM study,” *Scr. Mater.*, vol. 137, pp. 9–12, Aug. 2017.
- [40] J. A. Copley *et al.*, “In-situ observation of FCC->HCP transformation induced plasticity behavior during dynamic deformation of CoCrNi multi-principal element alloys,” *unpublished*, 2020.
- [41] D. Wei *et al.*, “Novel Co-rich high performance twinning-induced plasticity (TWIP) and transformation-induced plasticity (TRIP) high-entropy alloys,” *Scr. Mater.*, vol. 165, pp. 39–43, May 2019.
- [42] G. Laplanche, A. Kostka, C. Reinhart, J. Hunfeld, G. Eggeler, and E. P. George, “Reasons for the superior mechanical properties of medium-entropy CrCoNi compared to high-entropy CrMnFeCoNi,” *Acta Mater.*, vol. 128, pp. 292–303, Apr. 2017.
- [43] Y. Wang *et al.*, “Probing deformation mechanisms of a FeCoCrNi high-entropy alloy at 293 and 77 K using in situ neutron diffraction,” *Acta Mater.*, vol. 154, pp. 79–89, Aug. 2018.
- [44] M. Marteleur, F. Sun, T. Gloriant, P. Vermaut, P. J. Jacques, and F. Prima, “On the design of new β -metastable titanium alloys with improved work hardening rate thanks to simultaneous TRIP and TWIP effects,” *Scr. Mater.*, vol. 66, no. 10, pp. 749–752, May 2012.
- [45] X. Ji, S. Emura, X. Min, and K. Tsuchiya, “Strain-rate effect on work-hardening behavior in β -type Ti-10Mo-1Fe alloy with TWIP effect,” *Mater. Sci. Eng. A*, vol. 707, pp. 701–707, Nov. 2017.
- [46] X. H. Min, S. Emura, T. Nishimura, K. Tsuchiya, and K. Tsuzaki, “Microstructure, tensile deformation mode and crevice corrosion resistance in Ti-10Mo-xFe alloys,” *Mater. Sci. Eng. A*, vol. 527, no. 21–22, pp. 5499–5506, Aug. 2010.
- [47] X. H. Min, S. Emura, N. Sekido, T. Nishimura, K. Tsuchiya, and K. Tsuzaki, “Effects of Fe addition on tensile deformation mode and crevice corrosion resistance in Ti-15Mo alloy,” *Mater. Sci. Eng. A*, vol. 527, no. 10–11, pp. 2693–2701, Apr. 2010.
- [48] C. Li, J. H. Chen, X. Wu, and S. van der Zwaag, “Effect of strain rate on stress-induced martensitic formation and the compressive properties of Ti-V-(Cr,Fe)-Al alloys,” *Mater. Sci. Eng. A*, vol. 573, pp. 111–118, Jun. 2013.

- [49] S. Hanada and O. Izumi, "Correlation of tensile properties, deformation modes, and phase stability in commercial β -phase titanium alloys," *Metall. Trans. A*, vol. 18, pp. 265–271, Feb. 1987.
- [50] F. Sun *et al.*, "Investigation of early stage deformation mechanisms in a metastable β titanium alloy showing combined twinning-induced plasticity and transformation-induced plasticity effects," *Acta Mater.*, vol. 61, no. 17, pp. 6406–6417, Oct. 2013.
- [51] Z. Y. Yang, X. H. Zheng, and W. Cai, "Martensitic transformation and shape memory effect of Ti-V-Al lightweight high-temperature shape memory alloys," *Scr. Mater.*, vol. 99, pp. 97–100, Apr. 2015.
- [52] W. Wang, X. Zhang, and J. Sun, "Phase stability and tensile behavior of metastable β Ti-V-Fe and Ti-V-Fe-Al alloys," *Mater. Charact.*, vol. 142, pp. 398–405, Aug. 2018.
- [53] L. Lilensten *et al.*, "Design and tensile properties of a bcc Ti-rich high-entropy alloy with transformation-induced plasticity," *Mater. Res. Lett.*, vol. 5, no. 2, pp. 110–116, Mar. 2016.
- [54] F. W. Ling, H. J. Rack, and E. A. Starke, "An X-ray examination of deformation in β Ti-V alloys," *Metall. Trans.*, vol. 4, pp. 1671–1676, Jul. 1973.
- [55] S. Semboshi, T. Shirai, T. J. Konno, and S. Hanada, "In-situ transmission electron microscopy observation on the phase transformation of Ti-Nb-Sn shape memory alloys," *Metall. Mater. Trans. A Phys. Metall. Mater. Sci.*, vol. 39, pp. 2820–2829, Oct. 2008.
- [56] S. Sadeghpour, S. M. Abbasi, M. Morakabati, A. Kisko, L. P. Karjalainen, and D. A. Porter, "A new multi-element beta titanium alloy with a high yield strength exhibiting transformation and twinning induced plasticity effects," *Scr. Mater.*, vol. 145, pp. 104–108, Mar. 2018.
- [57] A. Zafari and K. Xia, "Stress induced martensitic transformation in metastable β Ti-5Al-5Mo-5V-3Cr alloy: Triggering stress and interaction with deformation bands," *Mater. Sci. Eng. A*, vol. 724, pp. 75–79, May 2018.
- [58] H. Y. Kim, J. Fu, H. Tobe, J. Il Kim, and S. Miyazaki, "Crystal Structure, Transformation Strain, and Superelastic Property of Ti-Nb-Zr and Ti-Nb-Ta Alloys," *Shape Mem. Superelasticity*, vol. 1, pp. 107–116, Jun. 2015.
- [59] T. Zhou, M. Aindow, S. P. Alpay, M. J. Blackburn, and M. H. Wu, "Pseudo-elastic deformation behavior in a Ti/Mo-based alloy," *Scr. Mater.*, vol. 50, no. 3, pp. 343–348, Feb. 2004.

CHAPTER 3

HISPOD AS A PREPARATORY TOOL FOR IMPROVING DESIGN OF HIGH-RATE, TIME-RESOLVED SYNCHROTRON X-RAY DIFFRACTION EXPERIMENTS

This work will be submitted to the Journal of Synchrotron Radiation for publication

J. Copley*¹, B. Ellyson¹, J. Klemm-Toole¹, J. Gao², N. Kedir², C. Kirk², W. Chen², N. Parab³, T. Sun⁴, K. Fezzaa³, A.J. Clarke¹

3.1 Abstract

Synchrotron light sources enable high rate, time resolved, simultaneous x-ray diffraction and imaging experiments. For intensity limited experiments involving time resolved diffraction, monochromacy may be sacrificed in favor of higher intensity polychromatic beams for increased time resolution. In these instances, the MATLAB program High Speed Polychromatic X-Ray Diffraction (HiSPoD) serves as powerful tool for processing and interpreting data. This work focuses on the use of HiSPoD as a preparatory tool for improving the results of diffraction performed using polychromatic synchrotron x-rays, with a specific focus on using HiSPoD to evaluate sample geometries and detector positions to improve data acquisition and the interpretability of collected diffraction results.

3.2 Introduction

Synchrotron light sources provide the capability to perform highly informative and unique experiments as a result of their high intensity, tunable x-rays and ability to perform ultra-fast imaging and diffraction experiments [1]–[3]. Synchrotron light sources may be used for x-ray radiography (microscopy), x-ray absorption spectroscopy, and x-ray diffraction experiments [1]. For the latter, the beam may be monochromated by use of mirrors, prisms, or diffraction through a perfect crystal to improve the quality of the collected diffraction patterns [4]. Flux or intensity limited experiments, such as high-rate-time-resolved diffraction, may not benefit from the use of a monochromatic beam, being unable to collect sufficient diffracted intensity to produce an interpretable diffraction pattern. In these instances, use of a higher

* Corresponding Author, email: jacopley@mines.edu

1: Colorado School of Mines, 1500 Illinois St, Golden, CO 80401

2: Purdue University, 610 Purdue Mall, West Lafayette, IN 47907

3: Argonne National Laboratory, 9700 S Cass Ave, Lemont, IL 60439

4: University of Virginia, 351 McCormick Rd, Charlottesville, VA 22904

intensity polychromatic beam with a sharp peak may be preferable, even at the expense of the sharpness of the diffraction patterns.

HiSPoD or High Speed Polychromatic x-ray Diffraction is a MATLAB based program developed at the Advanced Photon Source at Argonne National Laboratory for the purposes of processing and interpreting x-ray diffraction data collected using a polychromatic beam [5]. Specifically, HiSPoD was developed for diffraction experiments at Sector 32-ID of the APS, which is equipped with a miniaturized pressure bar and gas gun for high rate deformation experiments [6], [7]. These experiments occur in time frames of tens of microseconds or less, and thus require high x-ray fluxes to generate sufficient diffracted intensity for interpretable diffraction results [5]. HiSPoD includes capability to produce simulated diffraction patterns, when provided information about detector position, the energy intensity spectrum, the sample crystal structure and its allowed peaks and their relative intensities [5]. Generally, this information is used to locate the beam center using a built-in functionality. Locating the beam center allows for integration of the collected area patterns into more conventional 2θ vs. Intensity plots. Additionally, because most experiments are performed in transmission mode, HiSPoD includes capability to modify the energy spectrum by the fraction of intensity transmitted through the sample.

There are several important considerations in selecting a sample thickness for use in a transmission x-ray diffraction experiment using a polychromatic beam: those favoring thicker samples and those favoring thin samples. Samples with high thickness are generally more practical to produce and easier to work with. Additionally, given a fixed grain size, thicker samples will contain more grains and are more likely to produce full rings rather than “spotty” rings in the area diffraction patterns as compared to a thin sample. Factors favoring thin samples generally relate to the polychromatic nature of the beam used for high-rate-time-resolved diffraction experiments. This work focuses on the use of HiSPoD to evaluate the effects of sample thickness and detector position on the acquisition and interpretability of collected diffraction patterns.

3.3 Mitigating the diffraction effects of multiple harmonics by detector placement and sample geometry changes

3.3.1 Energy dependent beam attenuation as a result of heavy or thick samples

Undulators produce multiple peaks of intensity, referred to as harmonics, with increasing number harmonics being associated with multiples of the peak energy of the first harmonic. Generally, these higher order harmonics are lower in intensity than the first harmonic but can be broader. An example energy spectrum from Sector 32-ID of the APS, and the energy spectrum used for all models and experiments in this work, is shown in **Figure 3.1**.

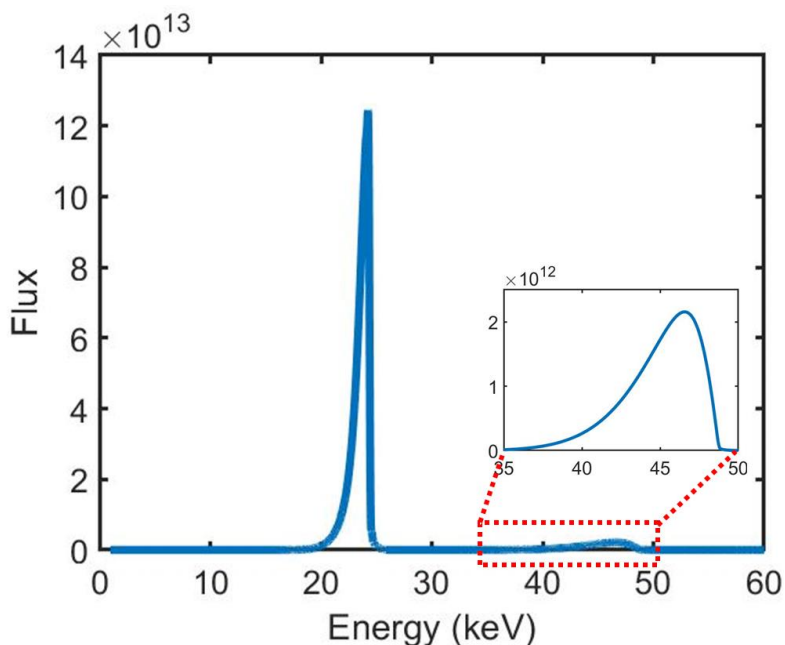


Figure 3.1: Example energy spectrum for a “pink” beam at a synchrotron light source. This spectrum matches the output of Sector 32-ID of the Advanced Photon Source with an undulator gap of 12 mm. This is the energy spectrum used to generate all simulated diffraction and attenuated energy spectrum results in this work.

As synchrotron x-ray diffraction experiments are often run in transmission mode (a schematic of which is shown in **Figure 3.2** on page 44), the penetration depth of the x-rays contributes to the diffracted intensity. Low energy x-rays with lower penetration depths will have reduced diffracted intensity in thick samples because the x-rays diffracted near the surface of the sample are unable to transmit through the rest of the sample without experiencing a second scattering event. Because higher level harmonics are higher in energy, they are less attenuated during transmission through the sample. Attenuation can be evaluated using the Beer-Lambert Law, which describes the transmitted intensity through a medium as a fraction of initial intensity

determined by an exponential factor based on the distance traveled through the medium and a material dependent factor. The Beer-Lambert law is shown below:

$$I = I_0 * e^{-x \mu(E)} \quad (3.1)$$

where x is the path length a photon must travel through the material and μ is a material and photon energy dependent function that describes the scattering of incident photons [8]. A high μ results in lower transmitted intensity. Generally, μ decreases with increasing photon energy, and increases with increasing atomic number. Values of μ for elemental media are readily available from the National Institute for Standards and Technology (NIST) for a wide range of photon energies, and values for μ for alloys and compounds can be generated by taking an average of the μ for the components, weighted by their mass fraction [9]. Depending on alloy composition and thickness, this can result in the second harmonic producing higher diffracted intensities as compared to the first harmonic. An example of alloy and thickness effects on the relative intensities of the first and second harmonic and the associated effects on area diffraction patterns are shown in **Figure 3.3** on page 46.

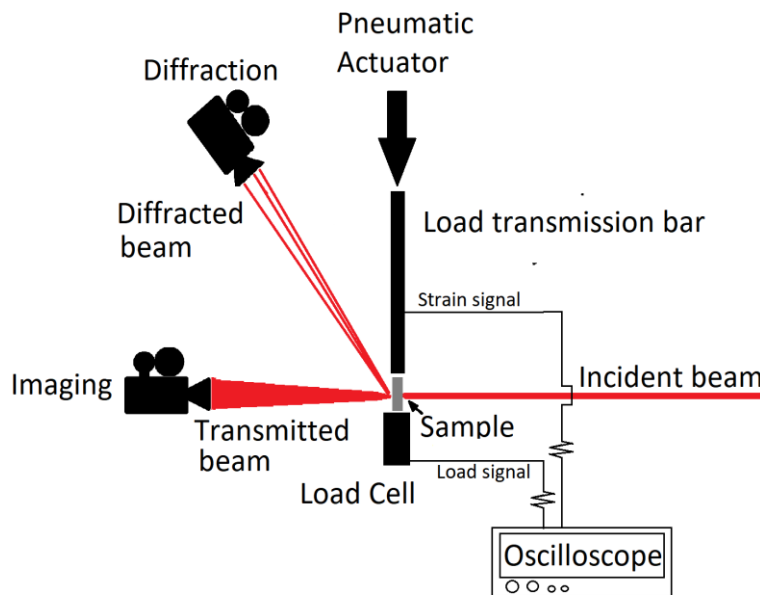


Figure 3.2: Schematic of the experimental setup for dynamic strain rate experiments at sector 32-ID of the APS, showing the positioning of the sample and detectors relative to the incident beam. Due to the requirement of the diffracted intensity to be transmitted through the sample in order to be collected, sample thickness effects become important for the diffraction.

Having too low a relative intensity of the first to second harmonic can be deleterious to collected diffraction results. Because the second harmonic is higher energy, the resulting rings will be closer to the beam center, as well as closer together. Additionally, because the second harmonic is broader, the resultant peaks will be both close together and broad. This can result in peak overlap that is difficult to deconvolute. The simulated diffraction patterns shown in **Figure 3.3** on page 46 show only peak broadening due to the polychromatic nature of the incident beam and the effect of attenuation of the beam on the relative intensities of the harmonics. This does not include peak broadening as a result of diffraction occurring at multiple locations within the volume of the sample or the noise inherent to high rate testing. As a result, second harmonic peaks are not well suited for diffraction applications. Actual patterns where the second harmonic dominates the collected diffraction patterns are shown later and compared to patterns collected with optimized thicknesses.

3.3.2 Detector positioning to minimize an unavoidable second harmonic

In cases where second harmonic effects cannot be mitigated by thinning of the sample, the second harmonic may be avoided by moving the high intensity peaks associated with it out of the frame of view of the diffraction camera. This idea is explored in **Figure 3.4**, located on page 48. When the high intensity peaks associated with the 2nd harmonic are moved out of the view of the camera, as in position 2, the highest intensity peak associated with the 1st harmonic becomes the maximum intensity against which other peaks present are normalized in processing. The high index peaks associated with the second harmonic may still be in view of the camera; however, they are likely to have lower relative intensities. Consequently, more peaks associated with the first harmonic are now visible. Identifying the peaks associated with the first and second harmonic is possible through use of the “Label (hkl) in I(tth)” function of HiSPoD.

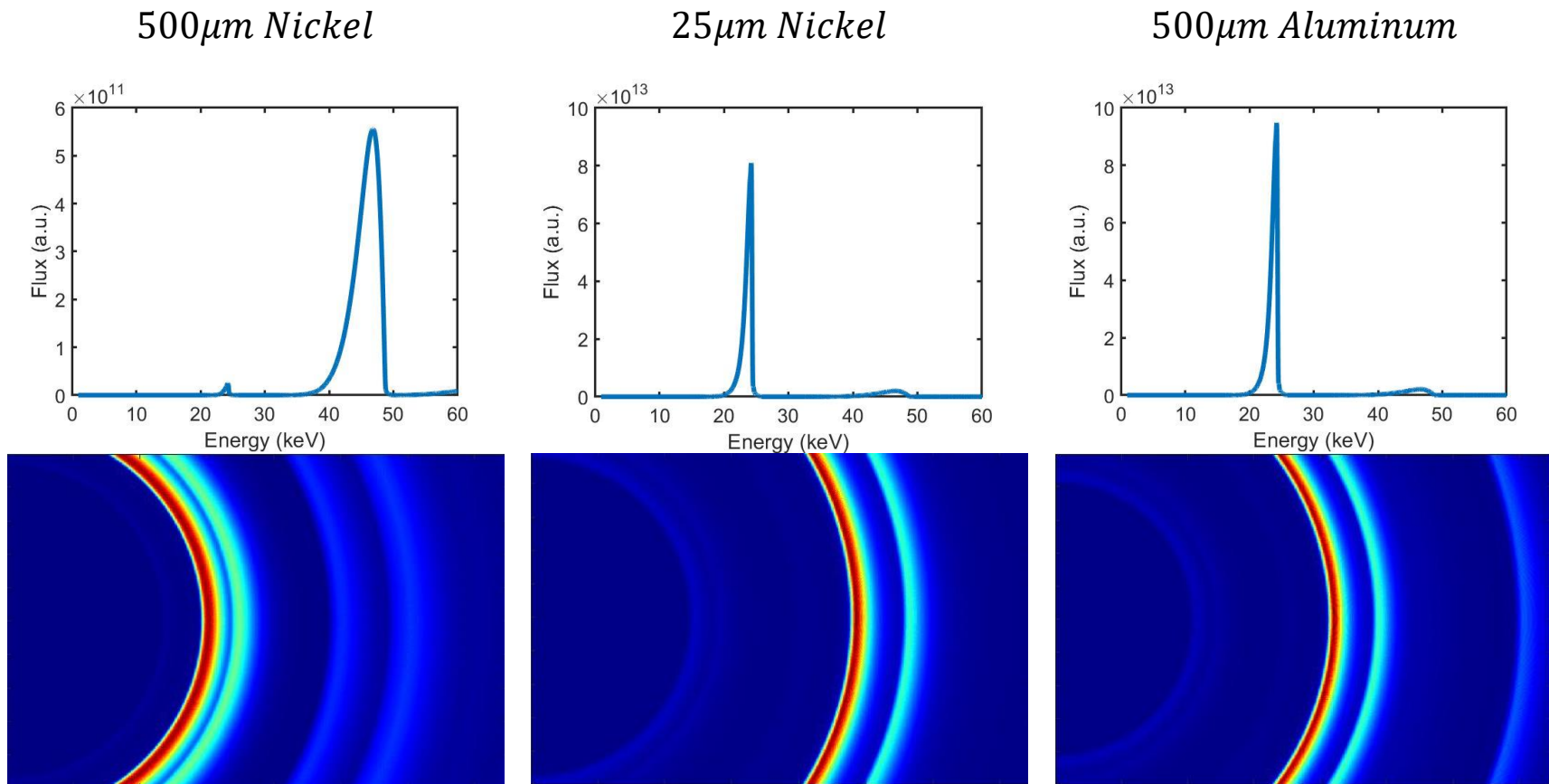


Figure 3.3: Attenuation corrected energy spectrums and simulated diffraction patterns of various thicknesses of pure aluminum and nickel, highlighting the effect of composition and thickness on the relative intensity of the first and second harmonics. Light metals, like aluminum, have low attenuation coefficients and thus higher intensities for the peaks associated with the lower energy first harmonic. Heavier metals, such as nickel, have higher attenuation coefficients and thus lower relative intensities for the lower energy first harmonic. This effect can be mitigated by using a thinner sample. Practical limits exist, however. In order for nickel to have an equivalent relative intensity of the harmonics as the 500 μm thick aluminum requires a sample thickness of approximately 25 μm , which may be beyond a practical limit for machining or use. Note also for the case of the 500 μm thick nickel sample that the peaks associated with the second harmonic (the rightmost arc segments) are closer together and broader as compared to their equivalent peaks in the 25 μm nickel or 500 μm aluminum first harmonic cases. Only peak broadening as a result of the polychromatic nature of the beam is simulated, not other sources of broadening.

There are limits to this technique. As the detector is moved away from the beam center, the fraction of each ring falling within the view of the camera is decreased, and thus the absolute diffracted intensity collected for these rings falls. If the absolute intensity is too low, these rings may become unobservable against noise. Moving the detector closer to the sample can combat this by increasing the fraction of the ring in view of the camera. Moving the detector closer will also have the effect of increasing the range of 2θ sampled, thus moving rings closer together. This is explored by position 3 in **Figure 3.4**, located on page 48.

In practice, it will likely be simpler to use HiSPoD find the best experimental parameters for the transformation one wishes to observe, then simulate the pattern of aluminum or another reference material using the same experimental parameters. Setting up for experiments at a light source, one can then move the detector into such a position that the collected pattern matches the desired simulated pattern for the reference. Any fine-grained, light metal would produce satisfactory results. Aluminum foil is an inexpensive, readily available, and effective reference material. This method is superior to using the parameters (i.e. Sample-to-Detector, Detector Angle, Direct Beam X, Direct Beam Y) entered in the “Experiment Parameters” portion of the HiSPoD graphical user interface as a guide to positioning the diffraction camera, as several of the experimental parameters are compounded by optics, especially the sample to detector distance.

3.4 Application of HiSPoD based optimization to a $\text{Co}_{50}\text{Cr}_{40}\text{Ni}_{10}$ MPEA

3.4.1 A brief description of TRIP behavior and interest

In-situ x-ray diffraction experiments are greatly beneficial for transformation induced plasticity (TRIP) enabled alloys as a means of observing the correlation between strain and transformation progress [10]–[12]. Alloys with TRIP behavior are of particular interest as structural materials, as TRIP behavior results in increased work hardening rates, delaying instability and producing increased ultimate tensile strength and uniform elongation [13]. Recent work in TRIP enabled MPEAs has suggested promise as blast resistant materials, necessitating the study of their TRIP behavior at high strain rates. At quasi-static strain rates, these experiments may be performed at a wide range of user facilities with monochromated beams, because these are not intensity limited experiments. Interrupted testing or magnetic measurements may also allow for similar studies, without need for a synchrotron light source [14]–[17].

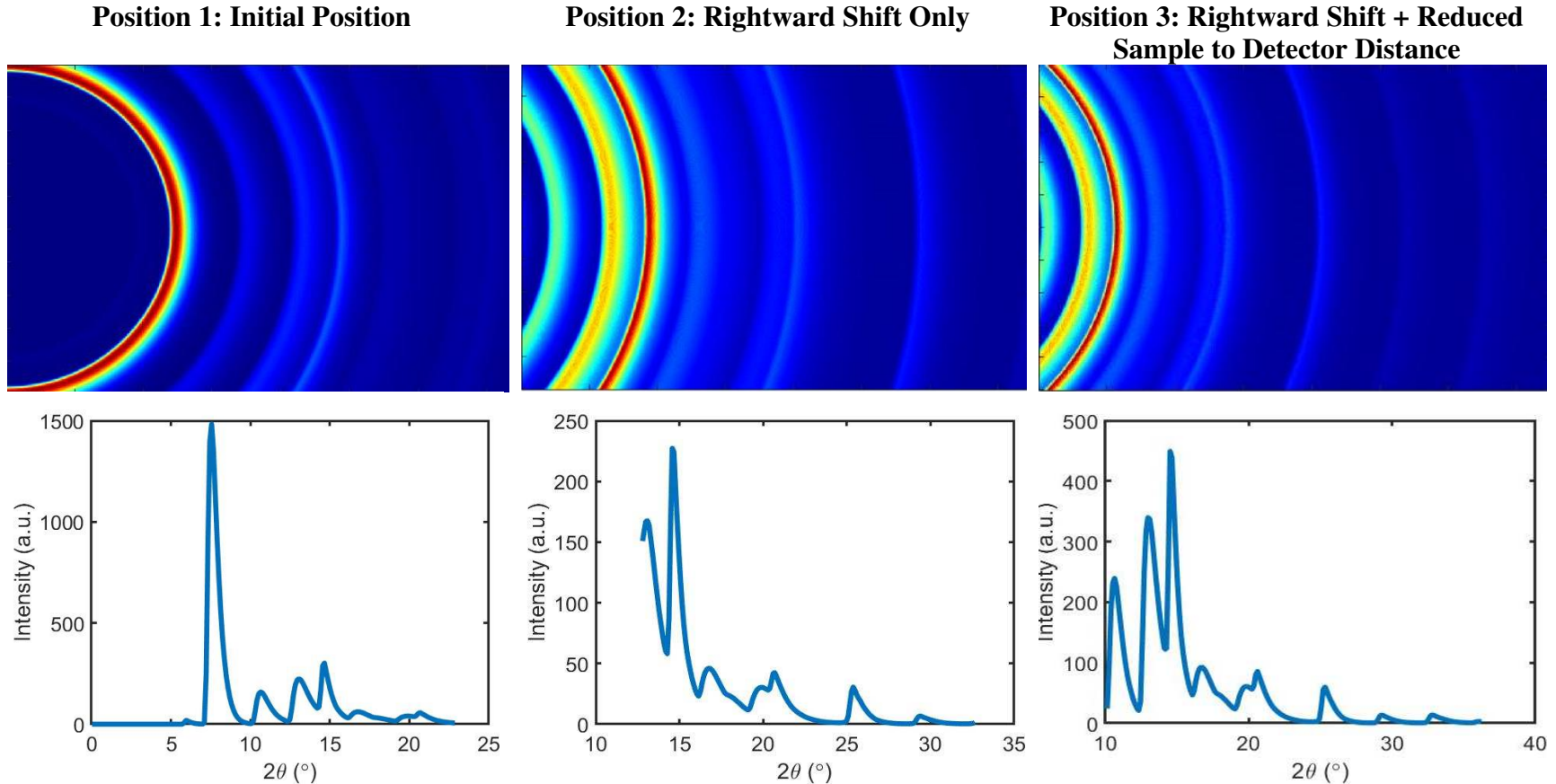


Figure 3.4: Simulated area diffraction patterns and corresponding integrated I vs 2θ plots for a $500\mu\text{m}$ thick iron sample, illustrating how shifting the detector position can alter collected diffraction patterns. While the second harmonic remains more intense than the first for all cases, for right-shifted camera positions in positions 2 and 3, the only visible peaks associated with the high intensity 2nd harmonic are high index peaks with relatively low diffracted intensities. This enables observation of peaks that would have been too low in relative intensity to be observed simultaneously with the low index second harmonic peaks. Because the most intense peak is now associated with the first harmonic, all first harmonic peaks with sufficiently high relative intensity to be seen when the second harmonic is not considered can now be observed. Because the first harmonic peaks are low in absolute intensity, moving the detector closer to the sample can result in increased collected intensity, as more of each ring is in the view of the camera, however, this also results in decreasing the separation between peaks, as shown by position 3.

For experiments at higher strain rates, intensity becomes a limiting factor in the time resolution of the diffraction, especially as many TRIP alloys are Fe-, Mn-, Ni-, or Co-rich and thus have high x-ray attenuation coefficients [13], [18]. The use of polychromatic beams to overcome this limitation can obscure changes in the diffraction, for example, the appearance of new peaks due to a phase transformation. To combat the effect of the polychromatic nature of the incident beam used in these experiments, the techniques discussed above were applied to an FCC→HCP TRIP enabled $\text{Co}_{50}\text{Cr}_{40}\text{Ni}_{10}$ alloy.

3.4.2 Second Harmonic Effects in $\text{Co}_{50}\text{Cr}_{40}\text{Ni}_{10}$

The first harmonic peak intensity of the incident beam used lies at 24.23KeV ($\lambda = 0.5117\text{\AA}$) and has an associated mass attenuation coefficient in Co of 143.6cm^{-1} , in Cr of 84.2cm^{-1} , and in Ni of 166.1cm^{-1} . The second harmonic peak intensity at 46.82KeV ($\lambda = 0.2648\text{\AA}$) has attenuation coefficients of 22.5cm^{-1} in Co, 12.9cm^{-1} in Cr and 26.3cm^{-1} in Ni. As the attenuation coefficients are much larger for the energy of the first harmonic as compared to the second harmonic, it can be anticipated that there are substantial changes in the relative intensity of the first and second harmonic for thick samples of this material. A quantitative assessment of this is shown in **Figure 3.5**, below, which shows the attenuation corrected energy spectra for two thicknesses of $\text{Co}_{50}\text{Cr}_{40}\text{Ni}_{10}$. Using these attenuation corrected energy spectra, simulation of optimal thickness and detector position is possible.

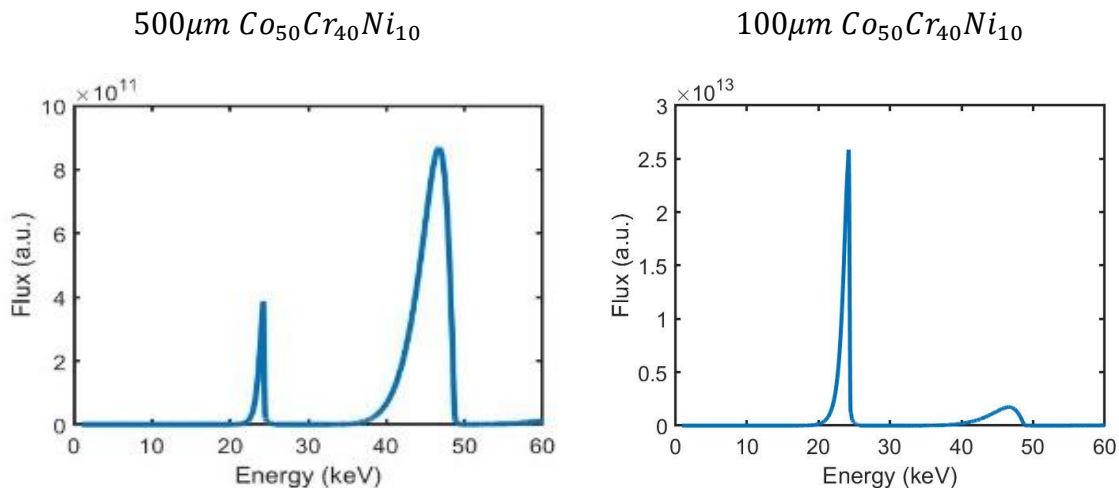


Figure 3.5: Attenuation corrected energy spectrums for given thicknesses of a TRIP enabled CoCrNi MPEA. As thickness decreases, both the relative intensity of the first and second harmonics and the absolute transmitted intensity increases. These thicknesses are actual sample thicknesses used during experiments at Sector 32-ID of the APS.

3.4.3 Simulations of Transformation as Compared to Experimental Results

These energy spectra can be used to enable comparisons between individual simulated area diffraction patterns, which are explored in **Figure 3.6** on page 51, illustrating the degree to which the high noise level of high rate deformation affects the ability to observe low index peaks. Additionally, attenuation corrected energy spectra can be used to generate simulations of the transformation within HiSPoD, using its built-in simulation functions. This involves simulating the area pattern for a range of phase fractions, then using HiSPoD to process the simulated patterns again to generate heatmaps of 2θ vs. Intensity vs. fraction transformed. These simulations are useful for both identifying optimal detector positions for observing a given phase transformation, and also for comparing to experimental results for qualitative comparison of the extent of transformation. This is explored in **Figure 3.7**, on page 52 for the example FCC \rightarrow HCP TRIP alloy. The TRIP behavior is readily observed in the optimized pattern, while it is difficult to identify in the unoptimized case. Relative to the unoptimized case, the optimized case uses thinner samples (100 μm vs 500 μm) and a rightward shift, as well as reduced sample to detector distance.

Some differences exist between the experimental results not attributable to the differences in sample thickness and detector position. These include a difference in aspect ratio and the presence of a ring of anomalous intensity near the edges of the unoptimized result. These differences are a result of a difference in the camera-scintillator set-up used in the experiments. The optimized patterns were collected using a Shimadzu Hyper-Vision HPV-X2 camera, while the unoptimized patterns were collected using a Photron FASTCAM SA1.1.

3.5 Summary

Access to synchrotron light sources is generally limited, and users are often unable to make significant changes to their samples during their allotted beamtime. As a result, all effort to ensure optimal experimental results is made. To this end, HiSPoD can serve as a powerful tool, not just for the post-processing of data collected during experiments at a beamline, but also for preparatory work. HiSPoD's ability to modulate the incident energy spectrum by energy dependent attenuation allows for the determination of sample thicknesses to improve the relative intensities of the various harmonics produced by undulators. This is especially important for observation of phase transformations in materials such as TRIP steels or MPEAs, where high

attenuation coefficients result in low diffracted intensities for the sharp first harmonic and low attenuation for the higher energy, but broad second harmonic. Beyond sample thickness effects, HiSPoD's simulation capabilities allow for identification of optimal detector positions to further mitigate effects of the second harmonic. As illustrated by the comparison between the unoptimized and optimized diffraction results presented in **Figure 3.7**, these methods have been used to great effect in the in-situ study of $\text{Co}_{50}\text{Cr}_{40}\text{Ni}_{10}$ with simultaneous synchrotron- x-ray diffraction using a polychromatic beam.

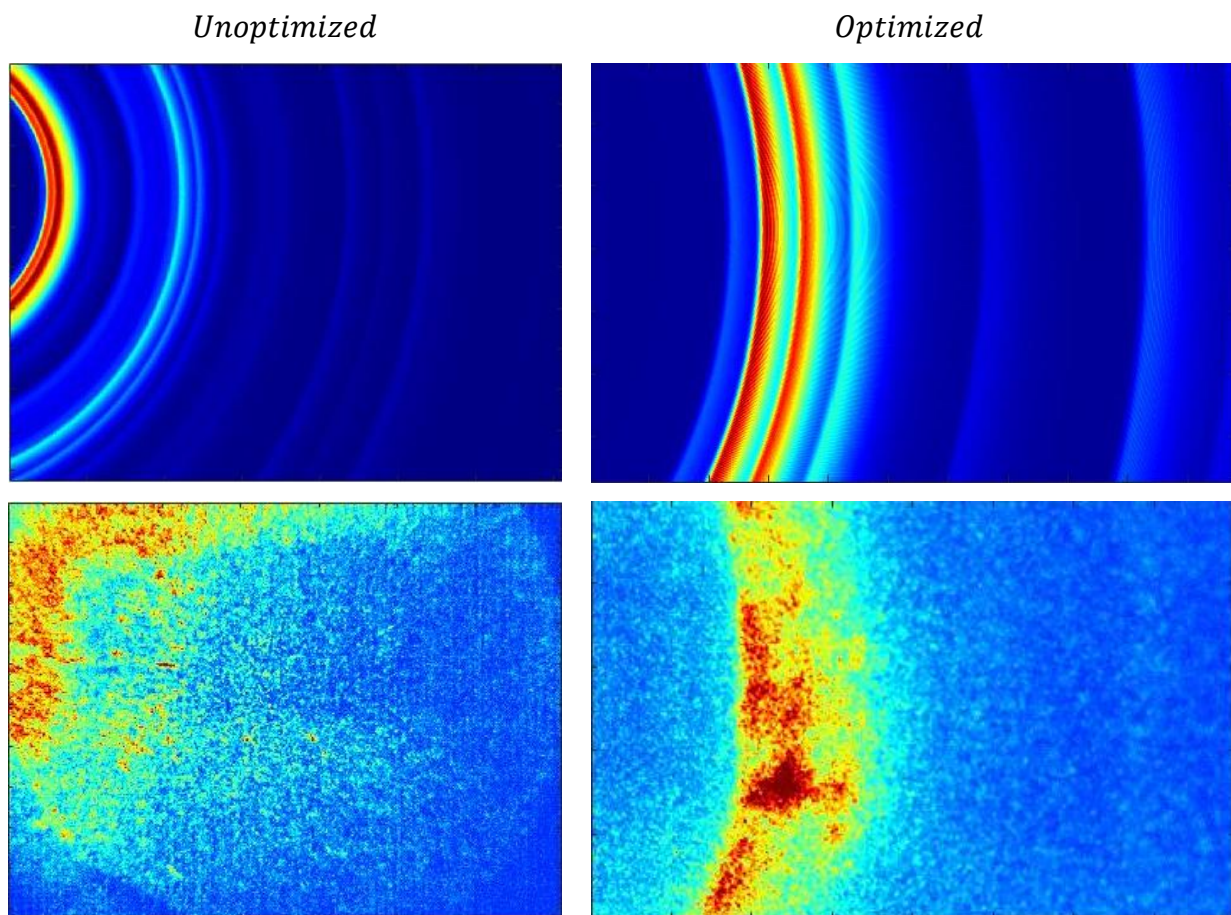


Figure 3.6: Optimized and unoptimized area diffraction patterns for a 50/50 mixture of FCC and HCP $\text{Co}_{50}\text{Cr}_{40}\text{Ni}_{10}$ tested at Sector 32-ID-B of the APS. A comparison can be made between the simulated patterns (above) and the collected patterns (below), with low relative intensity peaks in the simulation invisible against the noise of the experimental results. Because the high index peaks have low relative intensity and have a lower arc length caught by the diffraction camera, they have low absolute intensity and can be difficult to conclusively capture during experiments. Also, there is increased broadening as compared to the simulated patterns. This occurs because simulated patterns only include broadening as a result of the polychromatic nature of the beam, no other sources. Differences between the aspect ratio of the experimental patterns are a result of different diffraction cameras being used.

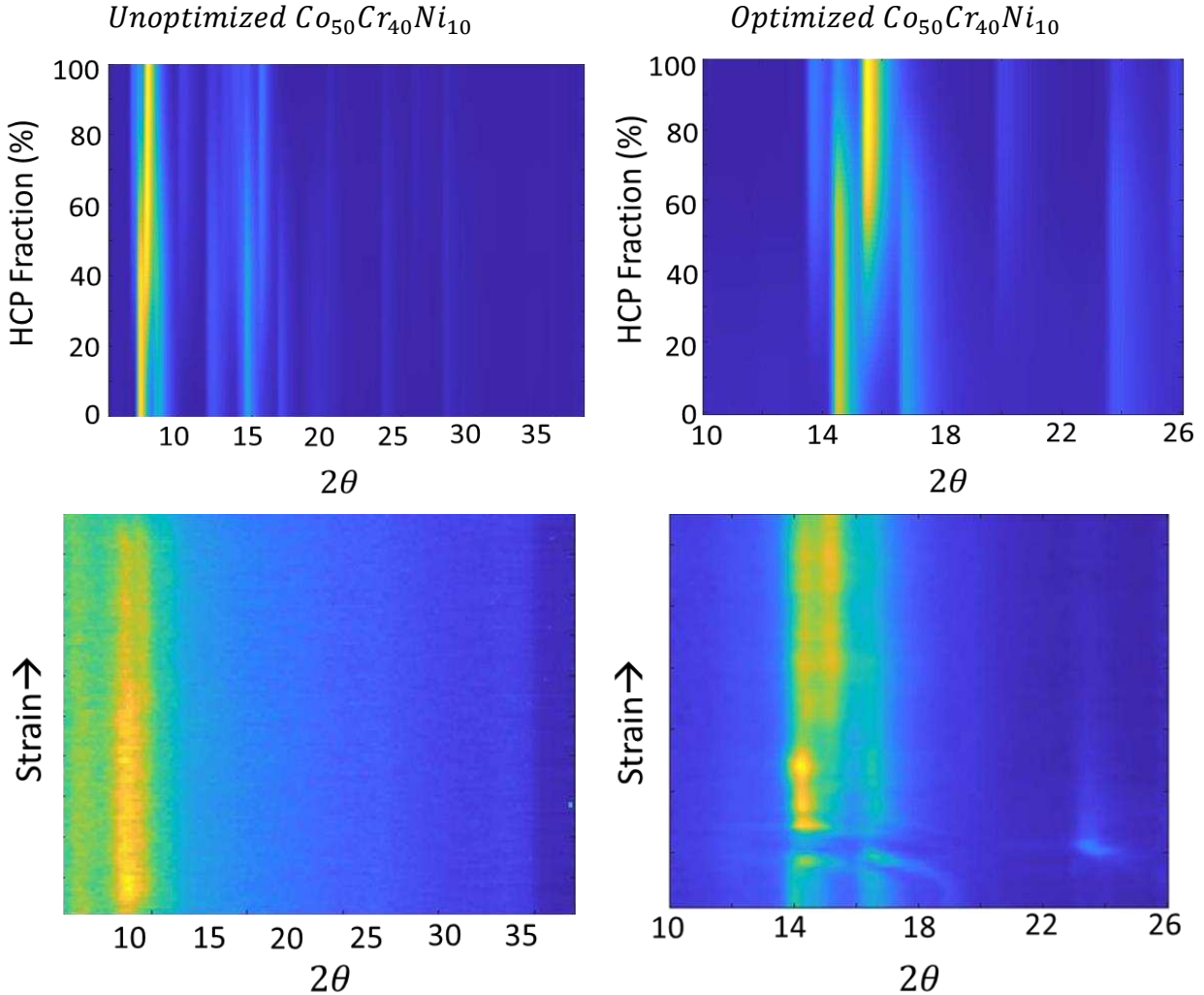


Figure 3.7: (Top) A comparison of an unoptimized and optimized simulation of a complete FCC \rightarrow HCP transformation in $Co_{50}Cr_{40}Ni_{10}$, as well as experimental results (bottom). In these simulations, the decrease in intensity of the FCC $\{111\}$ and $\{200\}$ peaks and appearance of the HCP $\{10\bar{1}1\}$ peak is much more evident in the optimized case, which uses both a decreased thickness ($100\ \mu m$ vs. $500\ \mu m$) and right-shift in detector position. In the unoptimized case, the high intensity of the high energy second harmonic results in the evidence of transformation being obscured by overlapping, broad peaks that are difficult to deconvolute, and the low intensity of peaks with sufficient separation to distinguish. In the optimized case, evidence of the transformation is clearer, as the peaks are both sharper and have greater separation.

References

- [1] I. M. Ternov, "Synchrotron radiation," *Physics-Uspekhi*, vol. 38, no. 4, pp. 409–434, Apr. 1995.
- [2] H. Navirian, R. Shayduk, W. Leitenberger, J. Goldshteyn, P. Gaal, and M. Bargheer, "Synchrotron-based ultrafast x-ray diffraction at high repetition rates," *Review of Scientific Instruments*, vol. 83. American Institute of PhysicsAIP, p. 063303, 08-Jun-2012.

- [3] B. Wang *et al.*, “Ultrafast synchrotron X-ray imaging studies of microstructure fragmentation in solidification under ultrasound,” *Acta Mater.*, vol. 144, pp. 505–515, Feb. 2018.
- [4] R. Caciuffo, S. Melone, F. Rustichelli, and A. Boeuf, “Monochromators for x-ray synchrotron radiation,” *Physics Reports*, vol. 152, no. 1. North-Holland, pp. 1–71, 01-Aug-1987.
- [5] T. Sun and K. Fezzaa, “HiSPoD: A program for high-speed polychromatic X-ray diffraction experiments and data analysis on polycrystalline samples,” *J. Synchrotron Radiat.*, vol. 23, pp. 1046–1053, Jul. 2016.
- [6] M. Hudspeth *et al.*, “High speed synchrotron x-ray phase contrast imaging of dynamic material response to split Hopkinson bar loading,” in *Review of Scientific Instruments*, 2013, vol. 84, no. 2, p. 025102.
- [7] S. N. Luo *et al.*, “Gas gun shock experiments with single-pulse x-ray phase contrast imaging and diffraction at the Advanced Photon Source,” *Review of Scientific Instruments*, vol. 83. American Institute of PhysicsAIP, p. 073903, 12-Jul-2012.
- [8] D. F. Swinehart, “The Beer-Lambert Law,” *J. Chem. Educ.*, vol. 39, no. 7, pp. 333–335, 1962.
- [9] J. H. Hubbell and S. M. Seltzer, “Tables of X-Ray Mass Attenuation Coefficients and Mass Energy-Absorption Coefficients from 1 keV to 20 MeV for Elements Z = 1 to 92 and 48 Additional Substances of Dosimetric Interest*,” *Radiation Physics Division, PML, NIST*, 2004. .
- [10] F. G. Coury *et al.*, “Design and in-situ characterization of a strong and ductile co-rich multicomponent alloy with transformation induced plasticity,” *Scr. Mater.*, vol. 173, 2019.
- [11] B. Fu, W. Y. Yang, Y. D. Wang, L. F. Li, Z. Q. Sun, and Y. Ren, “Micromechanical behavior of TRIP-assisted multiphase steels studied with in situ high-energy X-ray diffraction,” *Acta Mater.*, vol. 76, pp. 342–354, Sep. 2014.
- [12] N. Li *et al.*, “In situ X-ray microdiffraction study of deformation-induced phase transformation in 304 austenitic stainless steel,” *Acta Mater.*, vol. 64, pp. 12–23, Feb. 2014.
- [13] L. Liu, B. He, and M. Huang, “The Role of Transformation-Induced Plasticity in the Development of Advanced High Strength Steels,” *Adv. Eng. Mater.*, vol. 20, p. 1701083, Jun. 2018.
- [14] K. Yan, K. D. Liss, I. B. Timokhina, and E. V. Pereloma, “In situ synchrotron X-ray diffraction studies of the effect of microstructure on tensile behavior and retained austenite stability of thermo-mechanically processed transformation induced plasticity steel,” *Mater. Sci. Eng. A*, vol. 662, pp. 185–197, Apr. 2016.
- [15] Y. Tian, S. Lin, J. Y. P. Ko, U. Lienert, A. Borgenstam, and P. Hedström, “Micromechanics and microstructure evolution during in situ uniaxial tensile loading of TRIP-assisted duplex stainless steels,” *Mater. Sci. Eng. A*, vol. 734, pp. 281–290, Sep. 2018.

- [16] D. Kaoumi and J. Liu, “Deformation induced martensitic transformation in 304 austenitic stainless steel: In-situ vs. ex-situ transmission electron microscopy characterization,” *Mater. Sci. Eng. A*, vol. 715, pp. 73–82, Feb. 2018.
- [17] S. S. Hecker, M. G. Stout, K. P. Staudhammer, and J. L. Smith, “Effects of Strain State and Strain Rate on Deformation-Induced Transformation in 304 Stainless Steel: Part I. Magnetic Measurements and Mechanical Behavior,” *Metall. Trans. A*, vol. 13, pp. 619–626, Apr. 1982.
- [18] S. Wei, F. He, and C. C. Tasan, “Metastability in high-entropy alloys: A review,” *Journal of Materials Research*, vol. 33, no. 19. Cambridge University Press, pp. 2924–2937, 14-Oct-2018.

CHAPTER 4

IN-SITU OBSERVATION OF FCC→HCP TRANSFORMATION-INDUCED PLASTICITY BEHAVIOR DURING DYNAMIC DEFORMATION OF CoCrNi MULTI-PRINCIPAL ELEMENT ALLOYS

This work will be submitted to Metallurgical and Materials Transactions A for publication

J. Copley*¹, F.G. Coury², B. Ellyson¹, J. Klemm-Toole¹, N. Kedir³, C. Kirk³, W. Chen³, N. Parab⁴, T. Sun⁵, K. Fezzaa⁴, A.J. Clarke¹

4.1 Abstract

CoCrNi multi-principal element alloys (MPEAs) have potential as high toughness, blast resistant materials, but limited studies of their high strain rate behavior have been performed. Their high toughness has been attributed to their low stacking fault energies and the activation of toughness enhancing deformation mechanisms, such as twinning- and transformation-induced plasticity (TWIP and TRIP, respectively), that may be affected by increased strain rate. This work examines a series of CoCrNi MPEAs tested at dynamic strain rates using a miniaturized pressure bar with simultaneous synchrotron x-ray diffraction and imaging and compares these results to those collected during quasi-static deformation at elevated temperatures. The collected diffraction indicates TRIP behavior was active at elevated strain rates for the most Co-rich alloys, while TRIP behavior was suppressed in a lower Co-content alloy initially anticipated to experience TRIP. The suppression of TRIP in the lower Co alloy at high strain rates was attributed to adiabatic heating and was consistent with suppression of TRIP as a result of elevated temperatures.

4.2 Background and Introduction

Multi-Principal Element Alloys (MPEAs) and related materials, such as High Entropy Alloys (HEAs), Medium Entropy Alloys (MEAs) and Complex Concentrated Alloys (CCAs) have grown in interest since their introduction in 2004 by Cantor and Yeh [1], [2]. Some of these

* Corresponding Author, email: jacopley@mines.edu

1: Colorado School of Mines: 1500 Illinois St, Golden, CO 80401

2: Federal University of São Carlos, Rod. Washington Luiz, São Carlos - SP, 13565, Brazil

3: Purdue University, 610 Purdue Mall, West Lafayette, IN 47907

4: Argonne National Laboratory: 9700 S Cass Ave, Lemont, IL 60439

5: University of Virginia: 351 McCormick Rd, Charlottesville, VA 22904

materials, including the equiatomic CoCrNi alloy, have shown promise as exceptionally damage tolerant materials, especially at cryogenic temperatures [3], [4]. The discovery of CoCrNi's excellent mechanical properties has resulted in a surge of interest in MPEAs that experience specific deformation mechanisms, such as TWinning and TRansformation Induced Plasticity (TWIP and TRIP, respectively), in search of more damage tolerant alloys [5]–[9]. TRIP and TWIP behaviors have been studied more extensively in advanced high strength steels, and are regarded as toughness enhancing deformation mechanisms, due to their ability to promote high work hardening rates and thus increased strength and uniform elongation[10]–[15]. While the face-centered-cubic (FCC) CoCrNi remains the structural alloy with the highest reported fracture toughness, other works have produced evidence of non-equiatomic alloys with comparable or superior tensile strength and ductility [3], [16]. Manganese containing MPEAs, such as those in the FeMnCoNi family have been shown to experience both TRIP and TWIP behaviors as well [17]. Recent work has shown the TRIP and TWIP effects may be enabled through alloying in the CoCrNi ternary, with Co-rich alloys experiencing TRIP behavior and Co-lean alloys experiencing TWIP behavior [18], [19]. This is a result of cobalt's effect on stacking fault energy and the increased stability of the hexagonal-close-packed (HCP) phase [20]–[23]. Because these alloys have excellent damage tolerance at cryogenic temperatures, it is anticipated that they may have similar performance at elevated strain rates and be suitable for blast resistance applications. This is supported by recent strain rate studies of FeMnCoCrNi and FeCoCrNi performed by *Shibani et al.*, as well as studies of FeCoCrNi performed by *Zhang et al.*, which showed increased strength and ductility as a function of increasing strain rate [24], [25]. While some dynamic testing has been performed on MPEAs, little work has been dedicated to examining the effects of strain rate on the activation of TRIP behavior.

Because TRIP behavior is predicated on a martensitic transformation from the parent to product phase (in this work, FCC→HCP), TRIP behavior is limited by the diffusionless transformation temperature. The diffusionless transformation temperature, T_0 is a thermodynamic factor describing the temperature at which two phases have the same free energy for a given composition. This serves as a limiting temperature for TRIP, because it is the maximum temperature at which a free energy savings from the martensitic parent→product phase transformation exists.

4.3 Experimental Methods

4.3.1 Quasi-Static Testing of a Co₅₅Cr₄₀Ni₅ MPEA at Elevated Temperatures

A Co₅₅Cr₄₀Ni₅ alloy (hereafter Co55) was predicted to experience TRIP behavior using Thermo-Calc software to identify alloys with high diffusionless transformation temperatures that lay within the single-phase region of the CoCrNi ternary phase diagram at 1200°C. While dual phase MPEAs exist that can have good mechanical properties, in CoCrNi the FCC region is bounded by intermetallics, such as σ -phase, which can have deleterious effects on mechanical properties [8]. **Figure 4.1** on page 59 explores the range of possible CoCrNi alloys with TRIP behavior. A roughly 3 kg ingot of Co55 was produced via spray forming from commercially pure precursor material. Samples were prepared by cold rolling, followed by heat treatment at 1200°C to recrystallize the material and ensure a fully FCC microstructure, before being machined by wire electro-discharge machining (EDM). A schematic of the sample geometry is provided in the supplemental materials. Tests were performed using a Gleeble thermo-mechanical simulator at the XTMS beamline at the Brazilian Synchrotron Light Laboratory (LNLS), using a beam energy of 12KeV ($\lambda = 0.1033\text{\AA}$) to perform simultaneous x-ray diffraction (in reflection geometry) and quasi-static straining ($\dot{\epsilon} = 8.75 * 10^{-4} s^{-1}$) at a range of temperatures from -100°C to 900°C. Coury *et al.* contains more details on the methodology for choosing this alloy, as well as additional description of the experimental parameters [18], [26].

4.3.2 High Rate Testing of CoCrNi TRIP and TWIP MPEAs

In this work a series of five CoCrNi alloys were selected, based on their ability to be heated into a single phase FCC disordered solid solution and to have a range of diffusionless transformation temperatures (in the method of F. Coury *et al.*) [18]. The alloys selected included four alloys along the $Co_XCr_{40}Ni_{60-X}$ line, with $X = 30, 40, 50,$ and 55 at\% , as well as the equiatomic $Co_{33.33}Cr_{33.33}Ni_{33.33}$. The selected alloys are plotted onto a map of the diffusionless transformation temperatures for the CoCrNi ternary in **Figure 4.1**, located on page 59. Hereafter, these alloys are referred to by their Co-content (e.g., Co₄₀Cr₄₀Ni₂₀ is Co40), aside from the equiatomic composition, which is referred to as CoCrNi. The diffusionless transformation temperatures for these alloys are presented in **Table 4.1** on page 59. These alloys were prepared by arc-melting in an inert argon atmosphere from high purity components (99.9% or greater). The resulting buttons were then forged at above 1000°C to improve their geometry for machinability. Samples were then machined using wire EDM, and manually ground to final

thickness of 100 μm . A schematic of the sample geometry is provided in the supplemental materials. This thickness is required, due to the high attenuation coefficients of Co, Cr, and Ni for photons in the energy range used for diffraction, as further described below. Finally, the samples were homogenized at 1150°C for 90 minutes before a water quench to room temperature to ensure a single-phase FCC microstructure. This heat treatment has been verified by laboratory X-ray diffraction (Cu-K α radiation) to produce a single-phase FCC structure in all alloys, except for Co55. As 1150°C is well above the FCC solvus for Co55, this is believed to be a result of a martensitic transformation during quenching, indicating Co55 has a martensite start temperature (M_s) above room temperature. These samples were tested at Sector 32-ID-B at the Advanced Photon Source (APS) at Argonne National Laboratory, using a miniaturized pressure bar (because of space limitations within the 32-ID-B hutch, only an incident bar, and not a transmitted bar, can be used) to perform high rate deformation ($\dot{\epsilon} \approx 1000\text{s}^{-1}$) with simultaneous synchrotron x-ray diffraction and imaging. More information on the pressure bar used may be found in Hudspeth *et al.* [27]. All thermodynamic data used was generated using Thermo-Calc 2020a and the TCHEA4 database, in which the Co-Cr-Ni ternary is fully assessed for all compositions and temperatures.

4.4 Results

Initial HCP in the spray-formed Co55 induced by machining was removed by a heat treatment at above 1200°C immediately prior to straining before quenching to the testing temperature, resulting in nearly fully FCC microstructures prior to straining. During quasi-static straining at temperatures between -100°C and 450°C, the samples showed clear evidence of the evolution of HCP peaks with strain, indicating the presence of a strain induced martensitic transformation, or TRIP. An example of the collected diffraction for the TRIP alloys is shown in **Figure 4.2**, on page 60. At the highest temperature, 900°C, TRIP behavior was not observed, as indicated by the lack of peaks evolving with strain in the diffraction, see **Figure 4.3** on page 61. For the 600°C and 750°C cases, HCP peaks evolve as a function of strain, but continue to grow after failure has occurred in the sample. This can be rationalized by considering the greater extent of deformation occurring near the point of failure and the movement of the neck into the beam after the sample has failed.

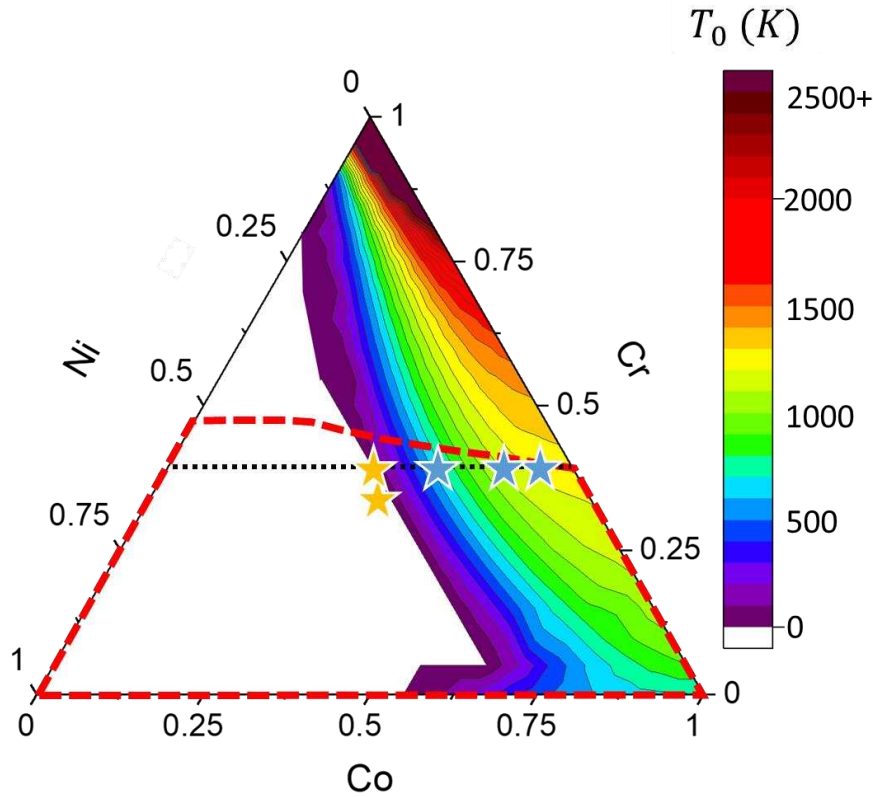


Figure 4.1: Diffusionless Transformation Temperatures of the CoCrNi ternary. Diffusionless transformation temperatures are increased by the additions of Co and Cr, which stabilize the HCP phase. Ni acts to stabilize the FCC phase, with resulting Ni-rich alloys having low T_0 , to the point of the HCP phase never being lower in energy than the FCC, regardless of temperature ($T_0 \leq 0K$). The single phase FCC region at 1200°C is marked with a dashed red line. The $Co_xCr_{40}Ni_{60-x}$ line is marked by a black dotted line. Alloys believed to be TRIP enabled are marked by blue stars, and alloys believed to be TWIP enabled are marked by yellow stars.

Table 4.1: Diffusionless transformation temperatures for the alloys tested. For the equiatomic CoCrNi and Co30 alloys, the relative stability of the FCC and HCP phases is such that there is no temperature at which the HCP is predicted to be more stable than the FCC.

| Alloy | T_0 (°C) |
|--|------------|
| CoCrNi | D.N.E |
| Co ₃₀ Cr ₄₀ Ni ₃₀ | D.N.E |
| Co ₄₀ Cr ₄₀ Ni ₂₀ | 407 |
| Co ₅₀ Cr ₄₀ Ni ₁₀ | 864 |
| Co ₅₅ Cr ₄₀ Ni ₅ | 967 |

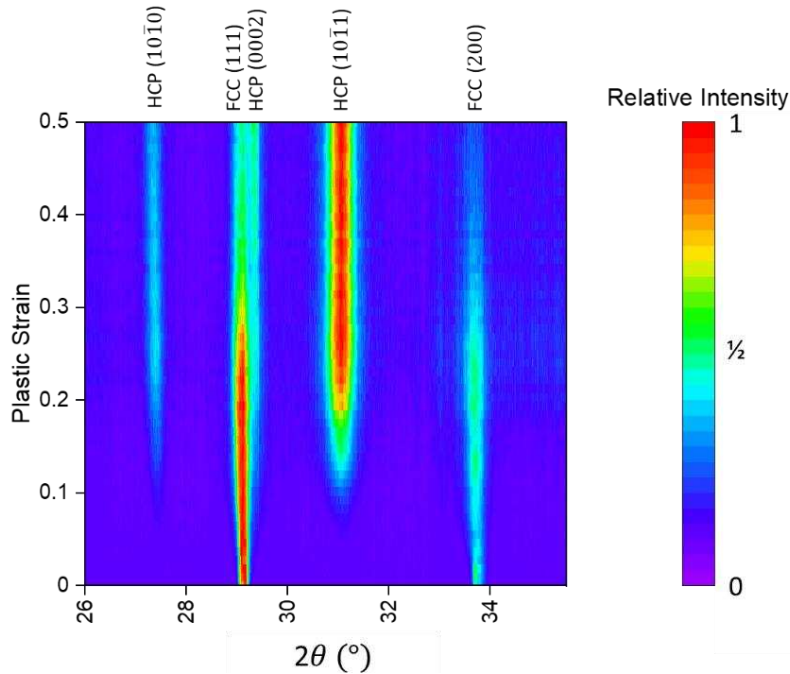


Figure 4.2: Heatmap of normalized intensity for $\text{Co}_{55}\text{Cr}_{40}\text{Ni}_5$ tested at 60°C showing the evolution of HCP peaks as a function of plastic strain from an initially pure FCC matrix. Detectable quantities of HCP begin forming at approximately 10% plastic strain, and the relative intensity of the HCP $(10\bar{1}1)$ peak continues to grow until approximately 20% plastic strain. The peaks are indexed and attributed to the FCC or HCP phases.

During the test, simultaneous crosshead motion in both directions was used to ensure the illuminated area of the sample was fixed, thus eliminating the effects of microstructural variation across the sample. However, after failure, the illuminated area of the sample changes in time due to continuing crosshead displacement. This would account for the near linear response of the HCP fraction with time after failure, as well as the close relation between the end of the crosshead displacement and the time at which the plateau in HCP fraction is reached. This data is explored in **Figure 4.4** for the 600°C case, located on page 62. It is not anticipated for this to be a diffusional transformation, because similar behavior is not observed in the 900°C case, where the equilibrium microstructure is fully HCP and due to increased temperature, diffusion should proceed at a much more rapid rate. This indicates that TRIP is still occurring at 600°C and 750°C , but requires additional damage to activate as compared to the lower temperature cases.

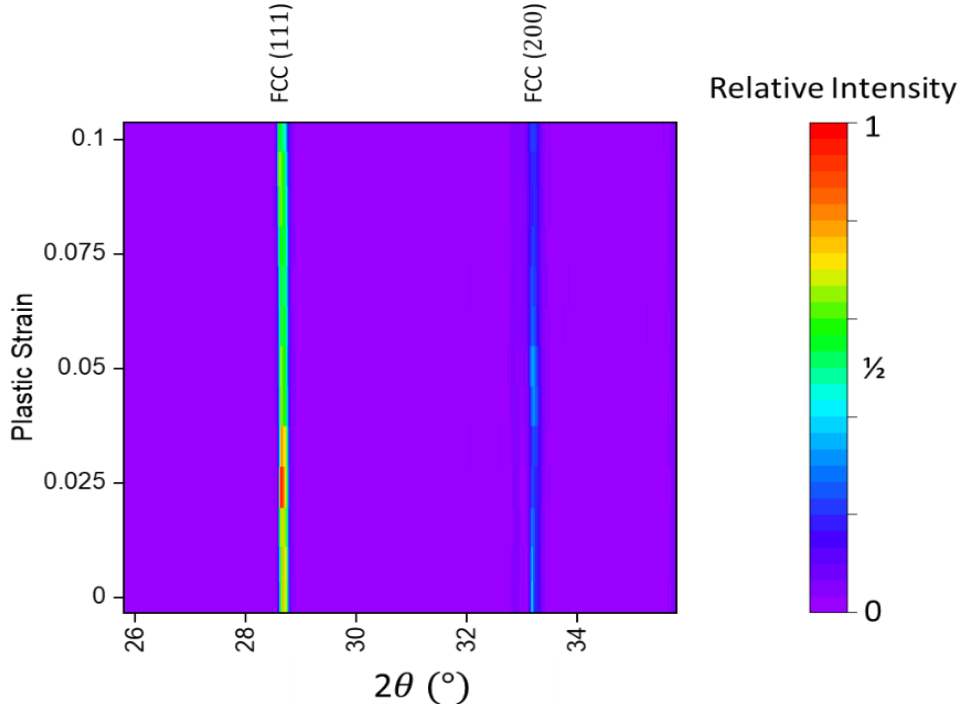


Figure 4.3: Heatmap of normalized intensity for $\text{Co}_{55}\text{Cr}_{40}\text{Ni}_{15}$ tested at 900°C showing no evolution of HCP peaks. This implies that either TRIP behavior was completely suppressed at this temperature, or so little transformation occurred that it could not be detected by the diffraction. In either case, this indicates elevated temperatures, even when still below T_0 , are able to result in suppressed TRIP behavior in CoCrNi alloys.

Because temperature correlates strongly with the activation of TRIP, analysis of the transformed fraction with plastic strain for all TRIP temperatures was performed. The fraction of HCP was determined by analyzing the relative areas of the FCC (111) and HCP ($10\bar{1}1$) peaks. Because the HCP (0002) peak overlaps with the FCC (111) peak, the area of the HCP ($10\bar{1}0$) peak, scaled by its relative intensity as compared to the HCP (0002) peak, was subtracted from the area ascribed to the FCC (111) peak. Assessing these for the plastic strains of the different temperature tests, and then using a generalized logistic fit (**Equation 4.1**) to assess the growth of the HCP phase results in **Figure 4.5**, on page 63. A difference in the behavior of the TRIP phenomenon as temperature increases is evident from both the plateaus and rates of transformation as shown by the data. The generalized logistic curve used is defined by **Equation 4.1**, below:

$$HCP(\varepsilon) = A + \frac{K - A}{(C + Q e^{-B\varepsilon})^{\frac{1}{v}}} \quad (4.1)$$

where A is the lower asymptote, K is the upper asymptote, Q is a factor relating to the initial HCP fraction prior to straining, B is the transformation rate, and ν describes the asymmetry of the curve. The parameter C is generally taken as 1 and alters the upper asymptote from K when $C \neq 1$. To enable direct comparison of the upper plateaus from the fits, the value of C has been fixed at 1. Additionally, as the microstructures were all initially fully FCC, the value of A was assumed to be 0 for all cases. The details of the fits are found in **Table 4.2**. The LNLS diffraction data shows a decrease in both the rate of transformation (defined using the growth rate parameter, B , of the generalized logistic curve) and the extent of transformation (defined as the upper asymptote of the generalized logistic curve). These values, as well as the fraction of T_0 and $\Delta G^{FCC \rightarrow HCP}$ for each temperature, are presented in **Table 4.2**, presented on page 64.

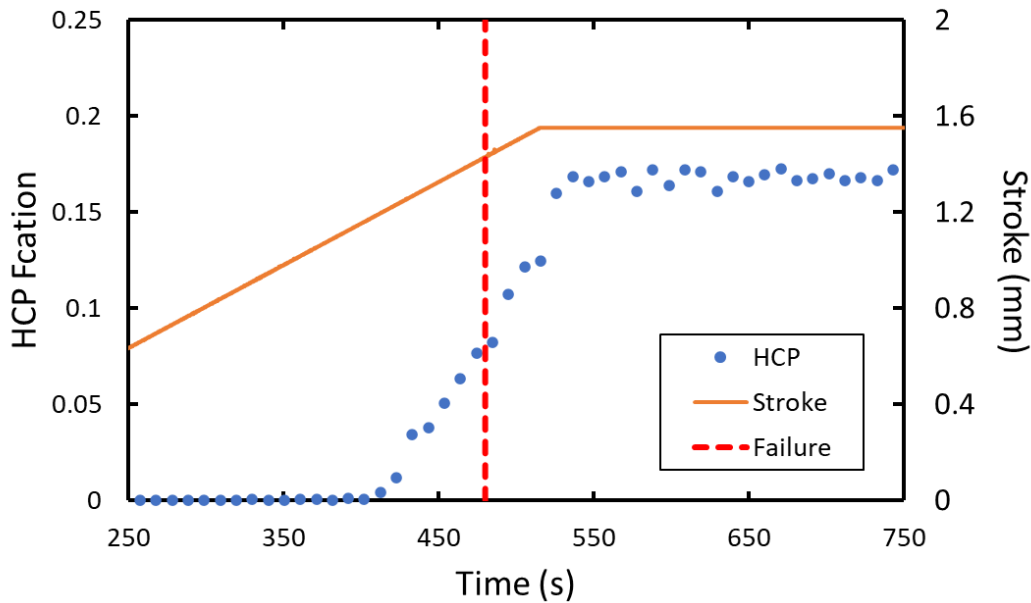


Figure 4.4: Transformation in $\text{Co}_{55}\text{Cr}_{40}\text{Ni}_5$ at 600°C continues after the failure of the sample (marked by red dashed line). The crosshead displacement (stroke) continues after the failure and ceases at approximately the same time as the HCP fraction plateaus. The constant rate of increase in HCP fraction with time differs from the logistic growth seen in the other temperatures with TRIP, but correlates well with the linear displacement. This suggests that HCP was forming in the material, likely in the necked region, before failure, and that after failure a more heavily transformed region was moved into the path of the beam.

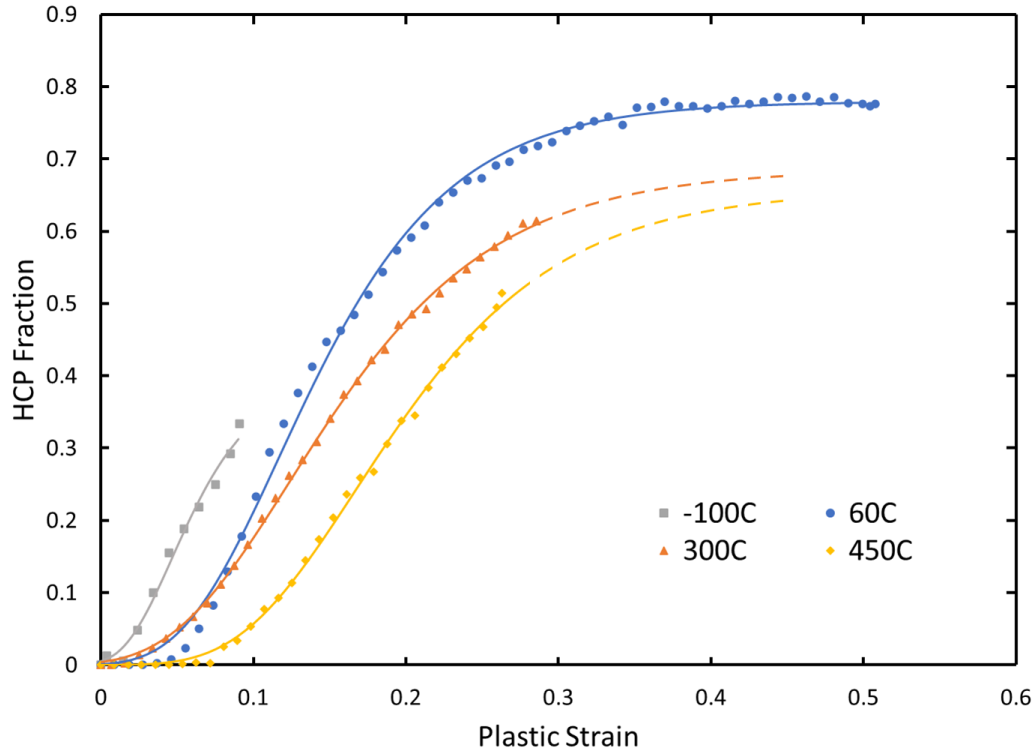


Figure 4.5: Plots of HCP fraction as a function of plastic strain for tests from -100°C to 450°C behavior, as determined from in-situ diffraction experiments at LNLS, along with generalized logistic fits of the data to estimate the plateau heights of the samples that failed before the plateau was reached. This shows a decrease in the plateau height for the maximum HCP as a function of increasing temperature (due to porosity, the -100°C test failed at a too low a strain to allow accurate estimation of the plateau height). In addition to decreasing plateau height, the increasing temperatures resulted in decreased growth rates in the generalized logistic fits. In the plots, this appears as a decreasing slope of the near-linear portion of the logistic fits.

Of the alloys tested with simultaneous x-ray diffraction and imaging during high rate deformation with a miniaturized pressure bar, three of the five tested alloys (CoCrNi, Co30 and Co40) showed no evidence of exhibiting TRIP type behavior, as no new peaks were evolved during the straining at 1000s^{-1} . The TRIP enabled Co50 showed evolution of a new peak attributable to HCP $\{10\bar{1}1\}$. The Co55, while containing initial HCP, showed increased intensity of the HCP $\{10\bar{1}1\}$ peak as compared to the FCC $\{111\}$ and $\{200\}$ peaks. Examples of the collected diffraction patterns, as compared to a simulation of the expected pattern for a 100% FCC \rightarrow HCP transformation, are shown in **Figure 4.6**, located on page 65.

Table 4.2: Parameters for fits of TRIP behavior as a function of temperature for Co₅₅Cr₄₀Ni₅, showing decreasing upper asymptotes (K), as well as transformation rates (B) with increasing temperatures. Also shown are the relevant thermodynamic parameters to TRIP behavior, T_0 and $\Delta G^{FCC \rightarrow HCP}$ for each temperature. 600°C and 750°C tests, which showed evolution of HCP after failure were not fit, as the HCP formation is better attributed to changes in the sampled region than deformation, and the 900°C test showed no HCP peak evolution.

| Temperature (°C) | TRIP | K | B | $Q * 10^7$ | $v * 10^7$ | T/T_0 | $\Delta G^{FCC \rightarrow HCP}$ (J/mol) |
|---------------------|------|--------|------|------------|------------|---------|---|
| -100 | Y | 0.399* | 32.2 | 4.69 | 1.06 | 0.14 | -2691.8 |
| 60 | Y | 0.779 | 15.9 | 4.64 | 0.73 | 0.27 | -2288.1 |
| 300 | Y | 0.686 | 13.2 | 4.54 | 0.90 | 0.46 | -1682.5 |
| 450 | Y | 0.657 | 13.3 | 11.3 | 1.23 | 0.58 | -1304.0 |
| 600 | Y | --- | --- | --- | --- | 0.70 | -925.6 |
| 750 | Y | --- | --- | --- | --- | 0.83 | -547.1 |
| 900 | N | --- | --- | --- | --- | 0.95 | -168.6 |

* Due to the limited strain at failure for the -100°C, accurate prediction of the upper asymptote is not possible, resulting in a prediction just shortly above the HCP fraction at failure.

Due to the high ductility of CoCrNi alloys, a number of the samples did not fail in the initial straining wave, but rather failed in subsequent pulses. The mechanical data for the subsequent loading was not collected. Examination of the mechanical response for the high rate testing shows similar stress-strain response for all alloys besides Co55, which exhibits increased strength and reduced ductility. The sinusoidal shape of the stress strain curves occurs due to ringing in the load cell, as a result of elastic wave propagation through the incident bar and sample. These are shown in **Figure 4.7**, located on page 66.

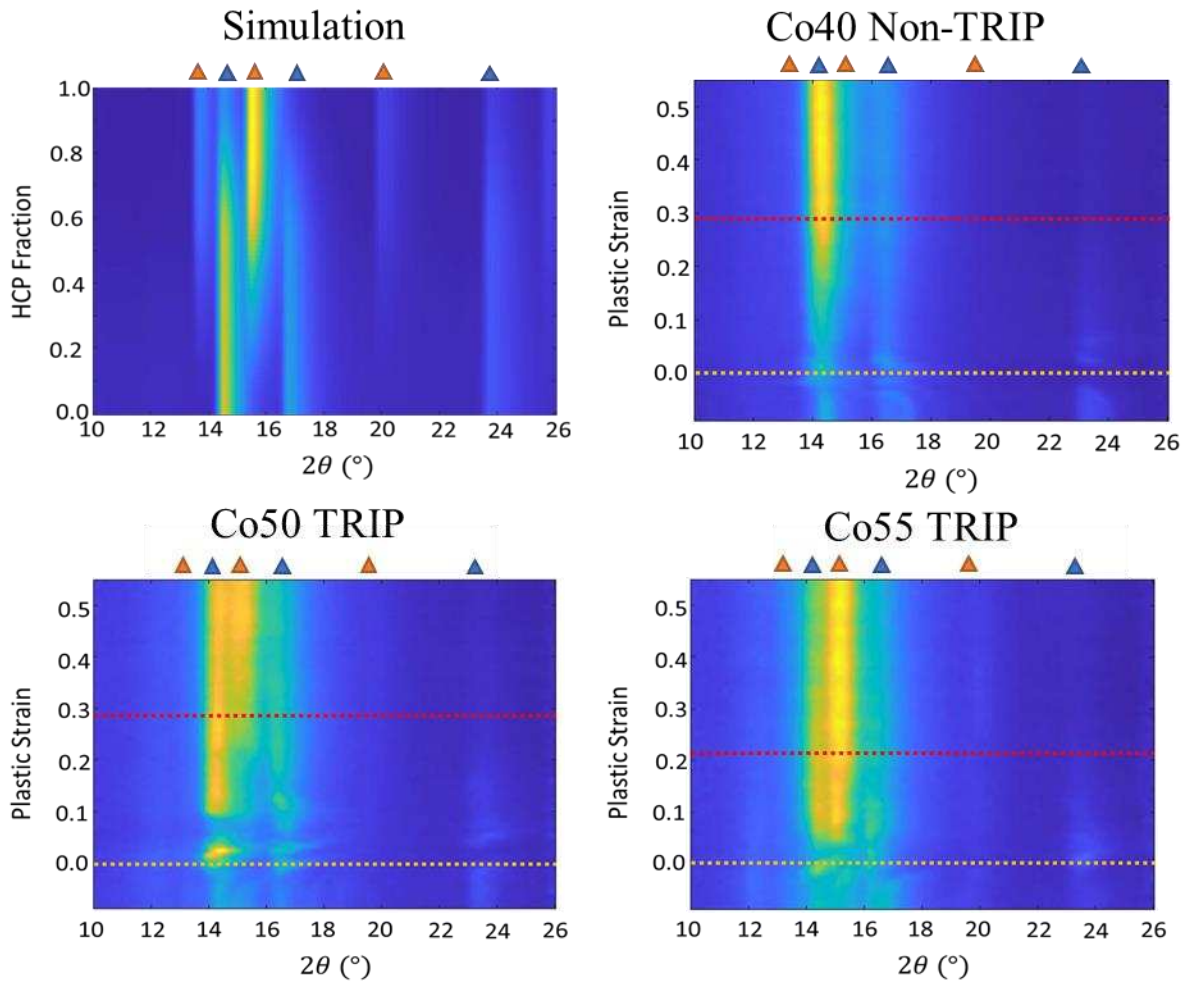


Figure 4.6: Comparison between simulated diffraction patterns showing a transformation from 100% FCC to 100% HCP, given the energy spectrum used for diffraction and detector geometry ($E_{peak} = 24.23\text{KeV}$, $\lambda_{peak} = 0.5117\text{\AA}$) with experimental results for a Co40 (non-TRIP), Co50 (TRIP), and Co55 (TRIP). The onset of straining, as well as failure or the end of the first straining pulse, whichever occurred first, are marked with dotted lines (gold and red, respectively). Qualitative comparison between the simulated diffraction and collected patterns shows a HCP fraction of 40-60% in the Co50 case at 30% strain, and of 60-80% in the Co55 case at 20% strain. Results for other non-TRIP alloys (CoCrNi and Co30) are similar to the Co40.

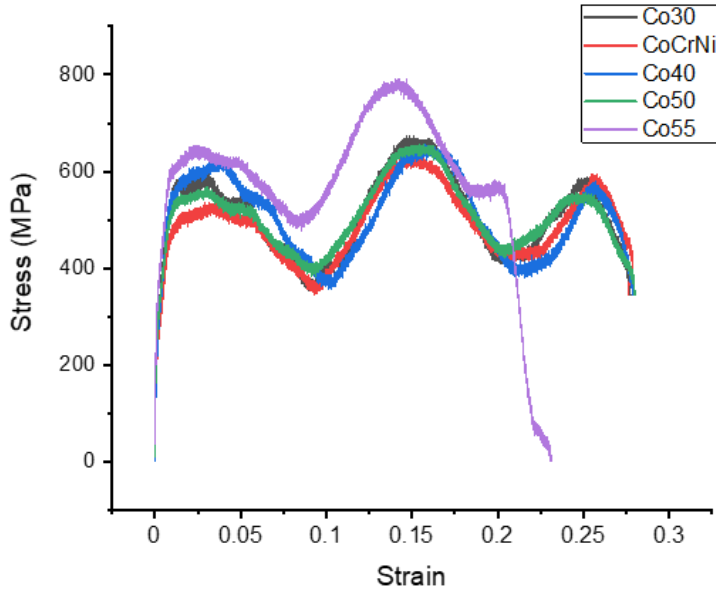


Figure 4.7: Mechanical response of alloys tested at $1070 \pm 15s^{-1}$. Co30, CoCrNi, Co40, and Co50 all demonstrate similar mechanical response to the high rate deformation. Co55 showed limited ductility as compared to the lower Co alloys. Only the Co55 alloy failed before the end of the first strain pulse.

4.5 Discussion

In the Co55 alloy tested at LNLS, suppression of TRIP behavior was seen even below T_0 . Beginning at 600°C , TRIP initiation required high strain levels as compared to the low temperature tests, where TRIP was active even at low plastic strains (5% or less). In the 900°C test, no evidence of TRIP behavior was observed. The effect of temperature on the driving force for TRIP is clear. At high temperatures (approaching $T/T_0 = 1$), the volumetric free energy savings for the martensitic transformation decrease. At $T/T_0 = 1$, there is no driving force for the transformation, and above this temperature, the forward progress of the reaction is thermodynamically forbidden. From the experiments at LNLS, it can be seen that the decrease in $\Delta G^{FCC-HCP}$ results in decreasing HCP fraction with strain, as well as decreased rates of HCP formation with strain. This can be attributed to the decreasing driving force of the transformation. As the temperature increases, the TRIP phenomenon becomes less favorable and other deformation mechanism(s) activate. For the case of the Co55 at 600°C , as compared to 60°C , there is a decrease in driving force of over 1.3kJ/mol , greater than one half of the driving force for TRIP at the lower temperature.

This reduction in driving force can also be examined as it relates to another measure of an alloy's TRIP potential, stacking fault energy. It has been established that as stacking fault energy increases, alloys shift from deformation by TRIP to TWIP to dislocation slip [28]–[30]. It is known that stacking fault energy, γ_{SFE} , increases with temperature, and therefore TWIP would be favored at elevated temperatures as compared to TRIP [31], [32]. Using the Olsen-Cohen model of stacking fault energy in FCC materials and considering only the effect of changing $\Delta G^{FCC \rightarrow HCP}$ for Co55 with temperature, it can be seen that stacking fault energy will increase by 82 mJ/m² at 600°C as compared to 60°C [33]. This suggests TWIP, or even dislocation slip, are activated as the primary deformation mechanism at elevated temperatures. For comparison, measurement of γ_{SFE} for Co55 showed room temperature stacking fault energies in the range of 18-24 mJ/m², which is consistent with the values reported for similarly Co-rich CoCrNi alloys by Koster *et al.* [34]. These data were generated using the method of Peirce *et al* [35]. and are presented in **Figure 4.8**.

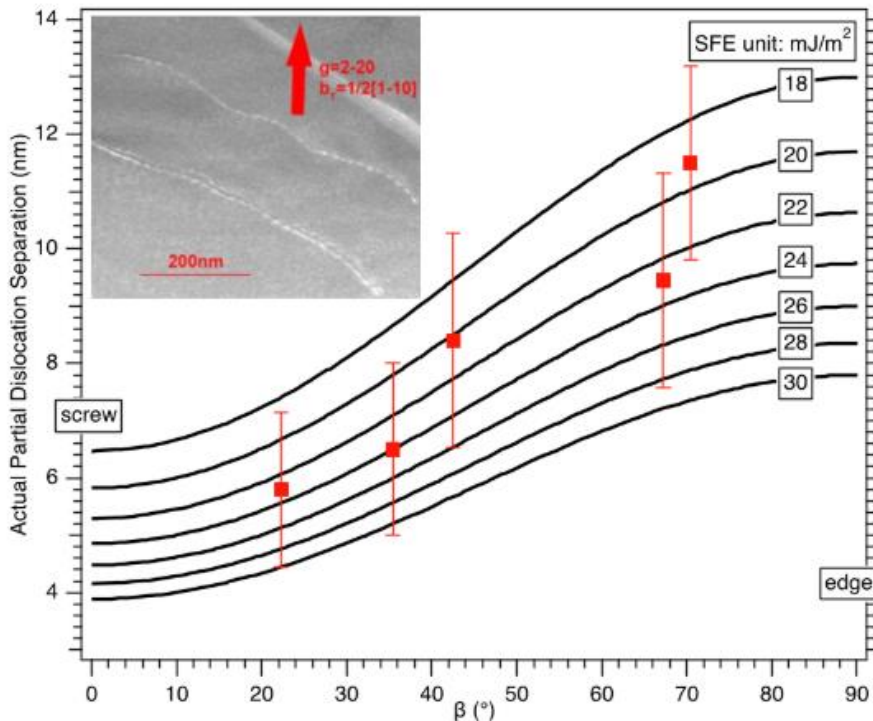


Figure 4.8: Measurements of stacking fault energy for Co55 at room temperature. These values are consistent with those reported in literature for Co-rich CoCrNi alloys, and are reflective of this alloy's potential to exhibit TRIP type behavior. Measurement of the stacking fault energy was performed in the method of Pierce *et al.* [35]. Results courtesy of Y. Guo, Colorado School of Mines.

TRIP behavior was anticipated in the Co40, Co50, and Co55 alloys, both by consideration of thermodynamic factors like the diffusionless transformation temperature, T_0 , and from previous work (for the Co55). The Co40 alloy was expected to TRIP based on its T_0 of 407°C and $\Delta G^{FCC \rightarrow HCP}$ of -916 J/mol at room temperature, as well as TRIP behavior that has been observed in a similar alloy, $\text{Co}_{36}\text{Cr}_{36}\text{Ni}_{28}$ [30]. As increased Ni acts to stabilize the FCC phase, it would be expected that increasing Ni at the expense of Co and Cr would result in an alloy less likely to TRIP, or conversely, that TRIP behavior would be promoted by decreasing Ni-content and replacing it with additional Co and Cr [36]. This suggests that an effect of the dynamic strain rates acted to suppress the TRIP behavior.

Dynamic testing has several effects on sample response. In general, and analogously to low temperatures, high strain rates reduce the thermal contribution to dislocation motion and promotes deformation twinning [37], [38]. Additionally, because the tests are short in duration, heat generated by plastic deformation during dynamic tests is unable to transfer to the surroundings and results in increased sample temperatures. Recent work by Soares *et al.* on an equiatomic FeMnCoCrNi alloy tested at strain rates up to 2800s^{-1} has shown the adiabatic heating can result in sample temperature increases of up to 80°C [39]. This is still below the diffusionless transformation temperature for Co40 of 407°C. At 380K (107°C), there is also a relatively large driving force for the FCC \rightarrow HCP transformation in Co40 ($\Delta G_{378\text{K}}^{FCC \rightarrow HCP} = -724.6 \text{ J/mol}$), allowing for the possibility of TRIP from a thermodynamic standpoint. However, volumes of HCP sufficient to be observed in the diffraction did not evolve. Comparing the driving force for the transformation in Co40 at 107°C to the driving forces of Co55 for the temperatures tested at LNLS shows that Co40 at 107°C has similar $\Delta G^{FCC \rightarrow HCP}$ as Co55 between 600°C and 750°C, where TRIP behavior required greater strain to activate, and only low fractions of HCP were ever produced. Due to high noise levels associated with high-rate diffraction, it is possible that HCP was evolved in low fractions, unable to be identified in the diffraction for the Co40. This is also consistent with behavior in 304 stainless steel. Work by Hecker *et al.*, as well as other studies, has shown that increased strain rates and associated adiabatic heating resulted in significantly reduced TRIP behavior as compared to quasi-static deformation [40][40]–[43]. Correlation between in-situ data and post-mortem examination is difficult on these samples, because of deformation that was not captured in the recorded

mechanical response data, both in the case of multiple pulses of strain, and also deformation occurring from the failed samples being deformed out of plane and at low strain rates when the incident bar rebounded after failure.

It is believed that the alloys not exhibiting TRIP type behavior instead exhibited TWIP behavior, including the Co40 alloy. Considering high strain rate to be analogous to low temperatures, this behavior is consistent with the reported deformation mechanisms of Co-lean CoCrNi MPEAs [19], [21]. While TWIP is more difficult to observe by means of in-situ diffraction with only partial ring detectors, the collected area diffraction patterns, which initially contain only partial, “spotty” rings rapidly evolve into full rings during the initial straining. This behavior is consistent with deformation twinning, as twinned regions introduce new crystal orientations. Examples of initial “spotty” rings and later full rings of a Co40 alloy are shown in **Figure 4.9** on page 70. While this is not solely indicative of TWIP behavior, in alloys like CoCrNi, which have been extensively reported to experience significant deformation twinning, TWIP type behavior is the most probable explanation [19], [21]. The TWIP behavior of Co40 is also consistent with the behavior seen in this work of Co55 at elevated temperatures, where Co55 has similar $\Delta G^{FCC \rightarrow HCP}$, and TRIP behavior is suppressed and replaced by another deformation mechanism.

Exploration of the mechanical response of the high rate data is complicated by ringing in the load cell, and the fact that not all alloys failed consistently in the first pulse of strain. The data shows the Co55 alloy has higher strength, but lowered ductility as compared to the other alloys tested (**Figure 4.7**). As tested, the Co55 was the only alloy with initial HCP in the microstructure. This initial HCP may result in the observed increase in strength and reduction in ductility as compared to the other alloys. HCP present in the initial microstructure would result in increased yield strength as a result of a composite strengthening effect, in which HCP acts as a stronger phase as compared to the FCC. The reduction in ductility may also be attributed to the initial HCP as the ductility in TRIP materials is a result of the high work hardening that the martensitic transformation promotes, which delays instability. By having initial HCP in the microstructure, the saturation of the transformation may occur at lower strain. As saturation of the transformation is expected to result in reducing work hardening rates, this may result in

instability, and thus a reduction in ductility of the sample, although additional studies of the bulk mechanical response and associated microstructural characterization are warranted.

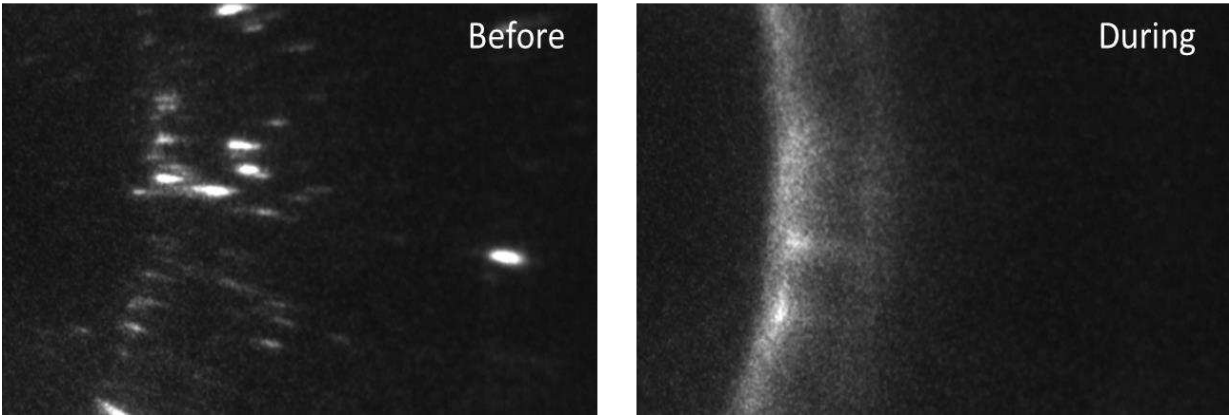


Figure 4.9: Evolution of full diffraction rings from initially “spotty” rings collected before and during straining of Co40 at high rate ($1000s^{-1}$) at the APS. This behavior is attributed to deformation twinning, which is promoted in FCC alloys during high rate deformation, and has been shown to be a common deformation mechanism in the CoCrNi family of MPEAs.

4.6 Conclusions

This work examined the suppression of TRIP behavior at temperatures below T_0 during quasi-static straining of a Co-rich TRIP alloy. At elevated temperatures where $\Delta G^{FCC \rightarrow HCP} \leq 1000J/mol$, TRIP behavior was nearly completely suppressed, and at temperatures where $\Delta G^{FCC \rightarrow HCP} \leq 200J/mol$, TRIP was suppressed completely. Assessing HCP evolution with plastic strain revealed that increasing temperature, and thereby decreasing the driving force for the martensitic transformation, resulted in both decreased rate and extent of the transformation. These results were compared to and used to explain the suppression of TRIP in a lower Co-content TRIP alloy during dynamic testing at $1000s^{-1}$. In this case, adiabatic heating and the low driving force for transformation in low Co alloys act to suppress TRIP behavior and favor TWIP type behavior instead. Co-content was seen to dominate the activation of TRIP behavior, as it has a strong effect on the relative stability of the FCC and HCP phases and allowed for TRIP behavior to remain active for high Co alloys. TWIP remains active in CoCrNi at elevated strain rates, and becomes the deformation mechanism for Co40 when TRIP is suppressed.

Both TRIP and TWIP CoCrNi type alloys showed similar mechanical response at high strain rates, with the exception of the Co55 alloy, which had limited ductility and enhanced strength as compared to the other alloys. This was attributed to the presence of HCP in the

microstructure prior to straining. The initial HCP is believed to result in reduced ductility by reducing the strain at which saturation of the FCC→HCP transformation occurs, resulting in reduced work hardening and the onset of instability. Additionally, the initial HCP in the Co55 is believed to result in increased strength of that alloy through a composite strengthening type effect. Additional work is needed to assess the relative mechanical properties of CoCrNi alloys deformed at dynamic strain rates and explore the relationship between ductility and deformation mechanism.

4.7 Supplemental Materials

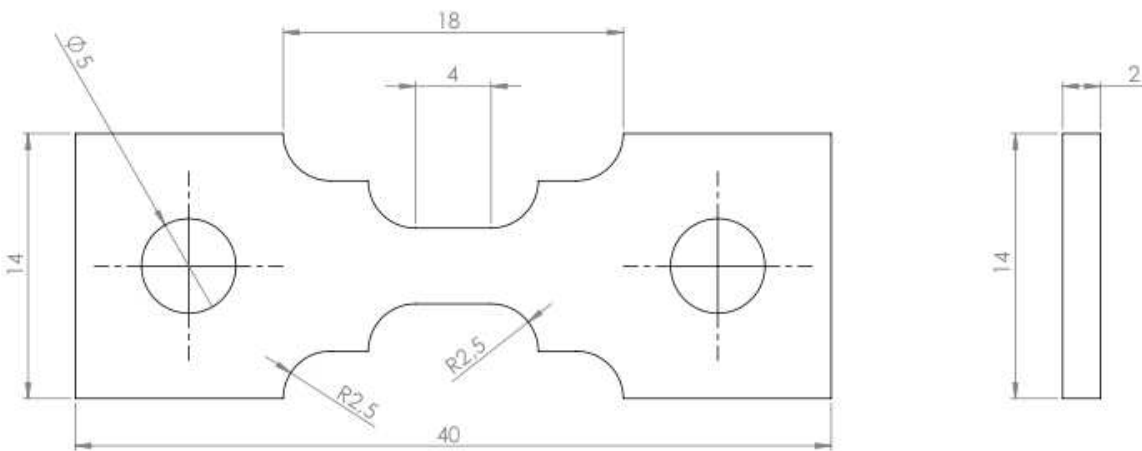


Figure 4.10: Geometry of samples used during quasi-static testing at the XTMS beamline of the Brazilian Synchrotron Light Source. Dimensions in mm.

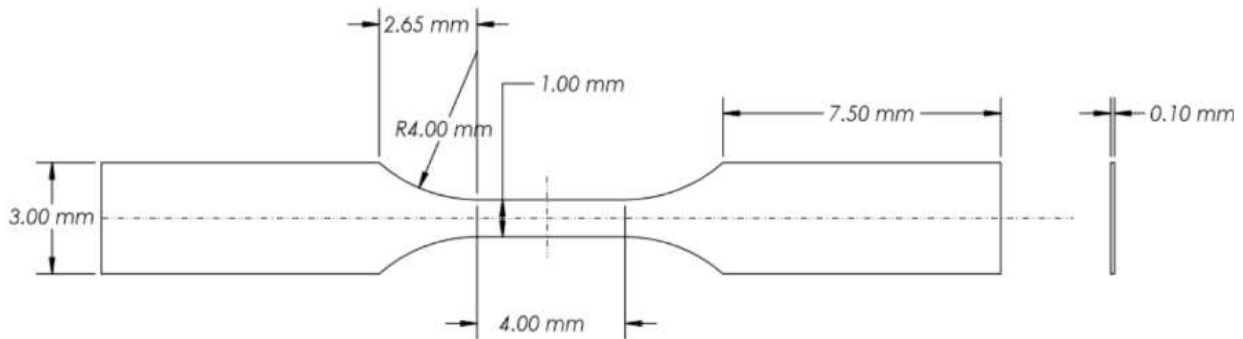


Figure 4.11: Geometry of samples used during high rate deformation of samples at Sector 32-ID of the Advanced Photon Source at Argonne National Laboratory. Dimensions in mm.

References

- [1] B. Cantor, I. T. H. Chang, P. Knight, and A. J. B. Vincent, "Microstructural development in equiatomic multicomponent alloys," *Mater. Sci. Eng. A*, vol. 375–377, pp. 213–218, Jul. 2004.
- [2] J. W. Yeh *et al.*, "Nanostructured high-entropy alloys with multiple principal elements: Novel alloy design concepts and outcomes," *Adv. Eng. Mater.*, vol. 6, no. 5, pp. 299–303, May 2004.
- [3] B. Gludovatz, A. Hohenwarter, D. Catoor, E. H. Chang, E. P. George, and R. O. Ritchie, "A fracture-resistant high-entropy alloy for cryogenic applications," *Science (80-.)*, vol. 345, no. 6201, pp. 1153–1158, Sep. 2014.
- [4] Z. J. Zhang *et al.*, "Nanoscale origins of the damage tolerance of the high-entropy alloy CrMnFeCoNi," *Nat. Commun.*, vol. 6, p. 10143, Dec. 2015.
- [5] Y. H. Jo *et al.*, "FCC to BCC transformation-induced plasticity based on thermodynamic phase stability in novel V10Cr10Fe45CoxNi35-x medium-entropy alloys," *Sci. Rep.*, vol. 9, p. 2948, Dec. 2019.
- [6] S.-H. Joo *et al.*, "Tensile deformation behavior and deformation twinning of an equimolar CoCrFeMnNi high-entropy alloy," *Mater. Sci. Eng. A*, vol. 689, pp. 122–133, Mar. 2017.
- [7] Y. Deng, C. C. Tasan, K. G. Pradeep, H. Springer, A. Kostka, and D. Raabe, "Design of a twinning-induced plasticity high entropy alloy," *Acta Mater.*, vol. 94, pp. 124–133, May 2015.
- [8] Z. Li, K. G. Pradeep, Y. Deng, D. Raabe, and C. C. Tasan, "Metastable high-entropy dual-phase alloys overcome the strength-ductility trade-off," *Nature*, vol. 534, pp. 227–230, May 2016.
- [9] Z. Li, F. Körmann, B. Grabowski, J. Neugebauer, and D. Raabe, "Ab initio assisted design of quinary dual-phase high-entropy alloys with transformation-induced plasticity," *Acta Mater.*, vol. 136, pp. 262–270, Sep. 2017.
- [10] L. Liu, B. He, and M. Huang, "The Role of Transformation-Induced Plasticity in the Development of Advanced High Strength Steels," *Adv. Eng. Mater.*, vol. 20, p. 1701083, Jun. 2018.
- [11] O. Bouaziz, H. Zurob, B. Chehab, J. D. Embury, S. Allain, and M. Huang, "Effect of chemical composition on work hardening of Fe-Mn-C TWIP steels," *Mater. Sci. Technol.*, vol. 27, pp. 707–709, Mar. 2011.
- [12] S. Yan, T. Liang, Z. Wang, B. Yan, T. Li, and X. Liu, "Novel 1.4 GPa-strength medium-Mn steel with uncompromised high ductility," *Mater. Sci. Eng. A*, vol. 773, p. 138732, Jan. 2020.
- [13] S. S. Sohn, H. Song, M. C. Jo, T. Song, H. S. Kim, and S. Lee, "Novel 1.5 GPa-strength with 50%-ductility by transformation-induced plasticity of non-recrystallized austenite in duplex steels," *Sci. Rep.*, vol. 7, p. 1255, Dec. 2017.

- [14] P. C. Maxwell, A. Goldberg, and J. C. Shyne, “Stress-Assisted and strain-induced martensites in Fe-Ni-C alloys,” *Metall. Trans.*, vol. 5, pp. 1305–1318, Jun. 1974.
- [15] D. T. Pierce, J. A. Jiménez, J. Bentley, D. Raabe, and J. E. Wittig, “The influence of stacking fault energy on the microstructural and strain-hardening evolution of Fe-Mn-Al-Si steels during tensile deformation,” *Acta Mater.*, vol. 100, pp. 178–190, 2015.
- [16] F. G. Coury, P. Wilson, K. D. Clarke, M. J. Kaufman, and A. J. Clarke, “High-throughput solid solution strengthening characterization in high entropy alloys,” *Acta Mater.*, vol. 167, pp. 1–11, Apr. 2019.
- [17] J. Tu *et al.*, “Deformation and annealing behaviors of as-cast non-equiatomic high entropy alloy,” *Mater. Sci. Eng. A*, vol. 737, pp. 9–17, Nov. 2018.
- [18] F. G. Coury *et al.*, “Design and in-situ characterization of a strong and ductile co-rich multicomponent alloy with transformation induced plasticity,” *Scr. Mater.*, vol. 173, 2019.
- [19] G. Laplanche, A. Kostka, C. Reinhart, J. Hunfeld, G. Eggeler, and E. P. George, “Reasons for the superior mechanical properties of medium-entropy CrCoNi compared to high-entropy CrMnFeCoNi,” *Acta Mater.*, vol. 128, pp. 292–303, Apr. 2017.
- [20] W. Li, H. Fan, J. Tang, Q. Wang, X. Zhang, and J. A. El-Awady, “Effects of alloying on deformation twinning in high entropy alloys,” *Mater. Sci. Eng. A*, vol. 763, p. 138143, Aug. 2019.
- [21] D. J. Siegel, “Generalized stacking fault energies, ductilities, and twinnabilities of Ni and selected Ni alloys,” *Appl. Phys. Lett.*, vol. 87, p. 121901, Sep. 2005.
- [22] M. Laurent-Brocq *et al.*, “Insights into the phase diagram of the CrMnFeCoNi high entropy alloy,” *Acta Mater.*, vol. 88, pp. 355–365, Apr. 2015.
- [23] K. Sasaki, K. Yabuuchi, S. Nogami, and A. Hasegawa, “Effects of temperature and strain rate on the tensile properties of twip steels,” *J. Nucl. Mater.*, vol. 461, no. 2, pp. 357–364, 2015.
- [24] M. Shabani, J. Indeck, K. Hazeli, P. D. Jablonski, and G. J. Pataky, “Effect of Strain Rate on the Tensile Behavior of CoCrFeNi and CoCrFeMnNi High-Entropy Alloys,” *J. Mater. Eng. Perform.*, vol. 28, no. 7, pp. 4348–4356, Jul. 2019.
- [25] T. W. Zhang *et al.*, “Simultaneous enhancement of strength and ductility in a NiCoCrFe high-entropy alloy upon dynamic tension: Micromechanism and constitutive modeling,” *Int. J. Plast.*, vol. 124, pp. 226–246, Jan. 2020.
- [26] G. Faria *et al.*, “Advanced Facility for Parallel Thermo-Mechanical Simulation and Synchrotron X-Ray Diffraction,” in *In-situ Studies with Photons, Neutrons and Electrons Scattering II*, Springer International Publishing, 2014, pp. 245–259.
- [27] M. Hudspeth *et al.*, “High speed synchrotron x-ray phase contrast imaging of dynamic material response to split Hopkinson bar loading,” in *Review of Scientific Instruments*, 2013, vol. 84, no. 2, p. 025102.

- [28] V. Borovikov, M. I. Mendeleev, A. H. King, and R. LeSar, “Effect of stacking fault energy on mechanism of plastic deformation in nanotwinned FCC metals,” *Model. Simul. Mater. Sci. Eng.*, vol. 23, no. 5, p. 055003, May 2015.
- [29] R. Kalsar, P. Khandal, and S. Suwas, “Effects of Stacking Fault Energy on Deformation Mechanisms in Al-Added Medium Mn TWIP Steel,” *Metall. Mater. Trans. A*, vol. 50, pp. 3683–3696, Aug. 2019.
- [30] Z. Yang *et al.*, “Designing transformation-induced plasticity and twinning-induced plasticity Cr-Co-Ni medium entropy alloys: theory and experiment,” Elsevier BV, Feb. 2020.
- [31] Y. Wang *et al.*, “Probing deformation mechanisms of a FeCoCrNi high-entropy alloy at 293 and 77 K using in situ neutron diffraction,” *Acta Mater.*, vol. 154, pp. 79–89, Aug. 2018.
- [32] S. Huang *et al.*, “Temperature dependent stacking fault energy of FeCrCoNiMn high entropy alloy,” *Scr. Mater.*, vol. 108, pp. 44–47, Nov. 2015.
- [33] G. B. Olson and M. Cohen, “A general mechanism of martensitic nucleation: Part I. General concepts and the FCC→HCP transformation,” *Metall. Trans. A*, vol. 7A, pp. 1897–1904, Nov. 1976.
- [34] E. H. Koster, A. R. Tholen, and A. Howie, “Stacking Fault Energies of Ni-Co-Cr Alloys,” *Philos. Mag.*, vol. 10, no. 108, pp. 1093–1095, 1964.
- [35] D. T. Pierce, J. A. Jiménez, J. Bentley, D. Raabe, C. Oskay, and J. E. Wittig, “The influence of manganese content on the stacking fault and austenite/ ϵ -martensite interfacial energies in Fe-Mn-(Al-Si) steels investigated by experiment and theory,” *Acta Mater.*, vol. 68, pp. 238–253, Apr. 2014.
- [36] G. N. Irving, J. Stringer, and D. P. Whittle, “Effect of the possible fcc stabilizers Mn, Fe, and Ni on the high-temperature oxidation of Co-Cr alloys,” *Oxid. Met.*, vol. 8, pp. 393–407, Dec. 1974.
- [37] G. T. (Rusty) Gray, “High-Strain-Rate Deformation: Mechanical Behavior and Deformation Substructures Induced,” *Annu. Rev. Mater. Res.*, vol. 42, no. 1, pp. 285–303, 2012.
- [38] Z. J. Jiang, J. Y. He, H. Y. Wang, H. S. Zhang, Z. P. Lu, and L. H. Dai, “Shock compression response of high entropy alloys,” *Mater. Res. Lett.*, vol. 4, no. 4, pp. 226–232, Oct. 2016.
- [39] G. C. Soares, M. Patnamsetty, P. Peura, and M. Hokka, “Effects of Adiabatic Heating and Strain Rate on the Dynamic Response of a CoCrFeMnNi High-Entropy Alloy,” *J. Dyn. Behav. Mater.*, vol. 5, pp. 320–330, Sep. 2019.
- [40] S. S. Hecker, M. G. Stout, K. P. Staudhammer, and J. L. Smith, “Effects of Strain State and Strain Rate on Deformation-Induced Transformation in 304 Stainless Steel: Part I. Magnetic Measurements and Mechanical Behavior,” *Metall. Trans. A*, vol. 13, pp. 619–626, Apr. 1982.

- [41] K. Clarke, "INFLUENCE OF STRAIN RATE ON THE MECHANICAL PROPERTIES AND FORMABILITY OF FERRITIC STAINLESS STEELS," Colorado School of Mines. Arthur Lakes Library, 2002.
- [42] J. Lichtenfeld and C. J. Van Tyne, "Effect of strain rate on tensile properties of austenitic stainless steels at room temperature," 2004.
- [43] W. A. Poling, "TENSILE DEFORMATION OF THIRD GENERATION ADVANCED HIGH STRENGTH SHEET STEELS UNDER HIGH STRAIN RATES," Colorado School of Mines. Arthur Lakes Library, 2016.

CHAPTER 5

SUMMARY AND AVENUES FOR FUTURE WORK

This chapter presents a general summary and review of conclusions from earlier chapters, and suggests potential avenues of future work that could expand upon the results of this work.

5.1 General summary and review of conclusions

Multi-Principal Element Alloys (MPEAs) are a promising class of materials that evolved out of initial studies of High Entropy Alloys (HEAs), when it was discovered that high entropies of mixing are not necessarily critical to the properties or phase stability of these alloys. Some MPEAs, including the equiatomic CoCrNi, have exhibited excellent combinations of strength and ductility, which indicates promise as blast resistant materials. The high damage tolerance of CoCrNi, as well as several other MPEAs, has been attributed to the activation of toughness enhancing deformation mechanisms, such as transformation and twinning induced plasticity (TRIP and TWIP, respectively). These deformation mechanisms result in high work hardening rates, and thus delay localized deformation by the Considère instability criterion. As a result, they simultaneously promote increased strength and uniform ductility, overcoming the strength-ductility tradeoff paradigm.

Due to the importance of TRIP and TWIP behavior to the mechanical properties of many MPEAs, and as the alloy design space for MPEAs is vast, efforts have been made to predict the activation of TRIP behavior as a preliminary step before experimental alloy design. These efforts include ab-initio density functional theory calculations, as well as other assessments of magnetic and electronic structure effects on phase stability. While these approaches have generally been successful, they are complex and computationally expensive. CALPHAD, or Calculation of Phase Diagram, approaches to predicting phase stability are computationally cheap compared to other methods. While not all alloy compositions have been explored or well modelled with CALPHAD approaches, CALPHAD's ability to extend knowledge about alloying and temperature effects in few component systems (three or fewer) to more complex systems (four or greater components) makes it well suited for high throughput exploration of MPEA design. For both ferrous alloys (steels) and MPEAs, it appears that thermodynamic considerations, such as $\Delta G^{\alpha \rightarrow \beta}$ and T/T_0 , are sufficient to predict the activation of TRIP behavior, with almost 90% of

alloy and temperature combinations evaluated, demonstrating TRIP behavior when $T/T_0 < 0.8$. This does not extend to metastable β -Ti alloys, where kinetic effects and more complex microstructure evolution may be responsible for the suppression of TRIP behavior, even with large $\Delta G^{\alpha \rightarrow \beta}$ and small T/T_0 .

Understanding the relationship between strain and transformation or strain and twinning is important for TRIP and TWIP alloys. While techniques, such as interrupted mechanical testing, exist to study this behavior at quasi-static and low strain rates, these techniques do not extend well to higher strain rates. In dynamic strain rate testing, there is no instrumental control of the strain rate after straining has begun, so interrupted tests are not possible. To access similar information as generated by the interrupted strain rate tests, in-situ experiments are required, often using synchrotron x-rays. These experiments are complicated by the short durations of these tests, which can occur in timeframes on the order of tens of microseconds. In order to generate sufficient signal during these tests, high fluxes of x-rays are required. While monochromated x-rays produce superior diffraction results, monochromation of a beam results in significant intensity loss, which can prevent sufficient signal:noise ratios for interpretable diffraction results. High speed polychromatic x-ray diffraction, or HiSPoD, is a program designed for the processing of diffraction data collected using a polychromatic beam at a synchrotron light source. HiSPoD can also be used for the evaluation of sample thickness and detector position, in order to optimize diffraction results collected during the limited and valuable time users are granted for experiments at synchrotron light sources.

As some MPEAs have shown excellent low temperature strength and toughness, it is anticipated they may also demonstrate similar performance at elevated strain rates and thus be suitable for blast resistance applications. Understanding how strain rate impacts the activation of deformation mechanisms is important for designing alloys that will remain damage tolerant in dynamic conditions. A series of CoCrNi alloys were tested using a miniaturized pressure bar at Sector 32-ID of the Advanced Photon Source (APS), while performing simultaneous x-ray diffraction and imaging using a polychromatic beam. The results showed TRIP remaining active in Co-rich alloys $\text{Co}_{55}\text{Cr}_{40}\text{Ni}_5$ and $\text{Co}_{50}\text{Cr}_{40}\text{Ni}_{10}$, which had the highest diffusionless transformation temperatures (T_0), while the TRIP effect was suppressed in a lower Co-content $\text{Co}_{40}\text{Cr}_{40}\text{Ni}_{20}$ alloy, which had a lower T_0 . Additionally, a TRIP enabled Co-rich MPEA,

Co₅₅Cr₄₀Ni₅, was produced via spray forming and strained at quasi-static rates while at temperatures between -100°C and 900°C with simultaneous synchrotron X-ray diffraction at the XTMS beamline of the Brazilian Synchrotron Light Laboratory. The results of the quasi-static straining showed that even below the diffusionless transformation temperature, increasing temperatures resulted in decreasing rates of the FCC→HCP transformation as well as a decrease in the maximum HCP fraction that evolves during straining. The suppression of TRIP observed in the Co₄₀Cr₄₀Ni₂₀ at dynamic strain rates was compared to suppression of TRIP in a Co₅₅Cr₄₀Ni₅ alloy at elevated temperatures during quasi-static testing and was attributed to effects of adiabatic heating. The alloys that did not exhibit TRIP behavior instead exhibit behavior consistent with the activation of TWIP. Due to limitations inherent to the nature of pressure bar experiments, comprehensive assessment of the mechanical properties of these alloys at high strain rates was not possible from these initial experiments. However, the data show the Co₅₅Cr₄₀Ni₅ alloy exhibits increased strength and limited ductility as compared to the other alloys tested. This behavior is attributed to the presence of some initial HCP in the microstructure of the Co₅₅Cr₄₀Ni₅ samples, although subsequent microstructural characterization and perhaps additional mechanical testing are recommended to explore this hypothesis.

5.2 Avenues for future work

Studies of MPEAs as a class of alloys have only begun recently. Thus, MPEAs are far from being optimized, as evidenced by many studies focusing on equiatomic or near equiatomic compositions. Much work remains to be done in the realm of MPEAs and related materials. This work includes continued studies of high strain rate testing of these alloys, as well as continued investigation into the activation and suppression of TRIP and TWIP toughness enhancing deformation mechanisms as a result of alloying, strain rate, and strain state. To this end, quasi-static deformation experiments of the alloys tested in this work with simultaneous x-ray diffraction, especially the Co₄₀Cr₄₀Ni₂₀ alloy, at elevated temperatures would illuminate the relative effects of temperature and kinetic effects on the suppression of TRIP in CoCrNi alloys at high strain rates. Interestingly, during the high rate deformation experiments at the APS, the collected x-ray imaging showed visible microstructural evolution during the straining. While these experiments were not optimized for this effect, future experiments could take advantage of the visible microstructural evolution to tie postmortem examination of deformation induced

microstructures to strain. These effects were most visible in well-polished, thin samples. Examples of the apparent microstructural changes are shown in **Figure 5.1**, located on page 79.

As CoCrNi alloys, while potentially possessing high damage tolerance, are costly to produce, investigation of potential Fe-rich MPEAs that exhibit similar deformation mechanisms may be beneficial to these materials being adopted into engineering applications. Two sets of Fe-rich MPEAs were explored in the same manner as the selection of Co-rich TRIP MPEAs tested here and are presented in **Figure 5.2** on page 79. While MPEAs are relatively new as a class of materials, a number of alloys have demonstrated promising properties that warrant further exploration. With further development, the design of MPEA microstructures with controlled deformation mechanisms and properties may be realized for structural applications and performance in extreme environments.

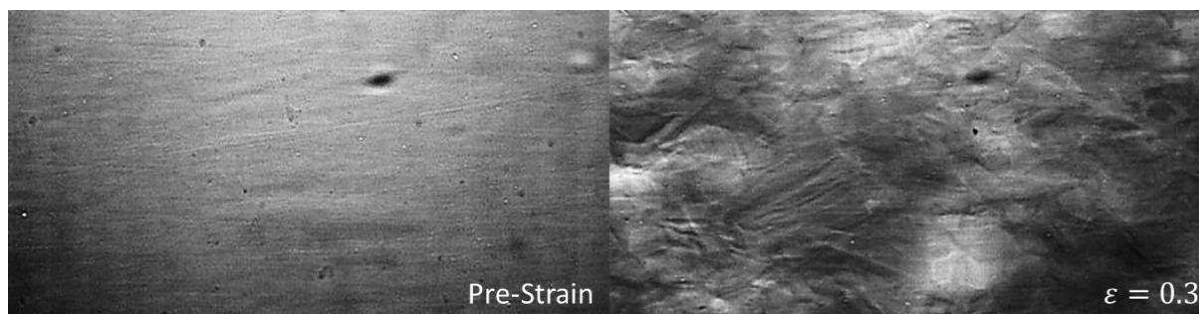


Figure 5.1: Example microstructural evolution visible in a TWIP enabled CoCrNi MPEA deformed under dynamic conditions at the APS with simultaneous synchrotron x-ray imaging. Grain and other microstructural features are clearly visible during deformation. This effect was maximized in the cases of thin and well-polished samples.

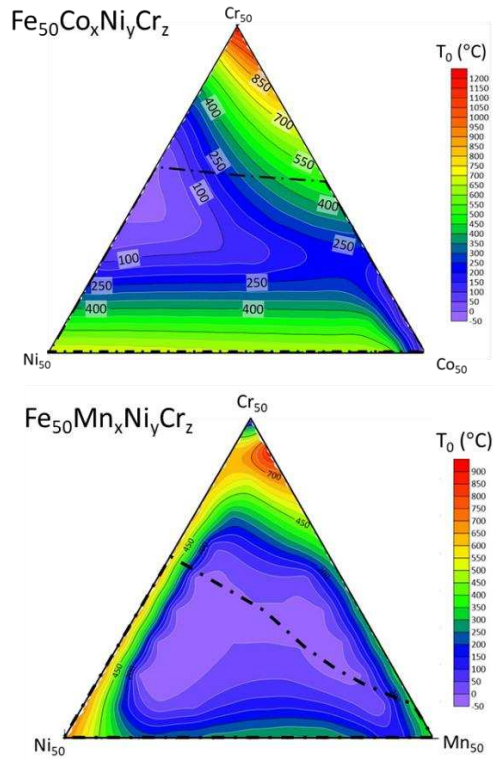


Figure 5.2: Maps of diffusionless transformation temperature (T_0) for two pseudo-ternary phase diagrams showing potential Fe-rich MPEAs capable of exhibiting FCC \rightarrow HCP TRIP. Both pseudo-ternaries are 50 at% Fe, with the remaining elements, either (top) Co-Cr-Ni or (bottom) Mn-Ni-Cr, comprising the remaining 50 at%. The FCC single phase region at 1200°C is marked with a black dotted and dashed line.

APPENDICES

Appendix A: Description of sample production and heat treatment.

All tested materials were produced from high purity precursor elements (>99.9% purity). Methods to produce material include spray forming, arc melting and bulk casting. Of these, the arc melting was most successful in producing fully dense material without inclusions or porosity. The arc melted buttons were used to produce samples for all testing performed at the Advanced Photon Source. These samples were forged at greater than 1000°C to form small rectangular prisms from the as cast arc-melted button. Samples were then machined from the ingots by wire EDM, then ground to final thickness manually, before being annealed at 1150°C for 90 minutes. Spray formed material was tested at the Brazilian light source, but porosity led to premature failure. No bulk cast material was used due to large chromium-oxide inclusions. The microstructures of the bulk cast and spray formed materials are shown below to illustrate their respective inclusions and porosity, as well as a micrograph and energy dispersive spectroscopy map of the arc melted samples to illustrate the lack of secondary phases and large scale segregation.

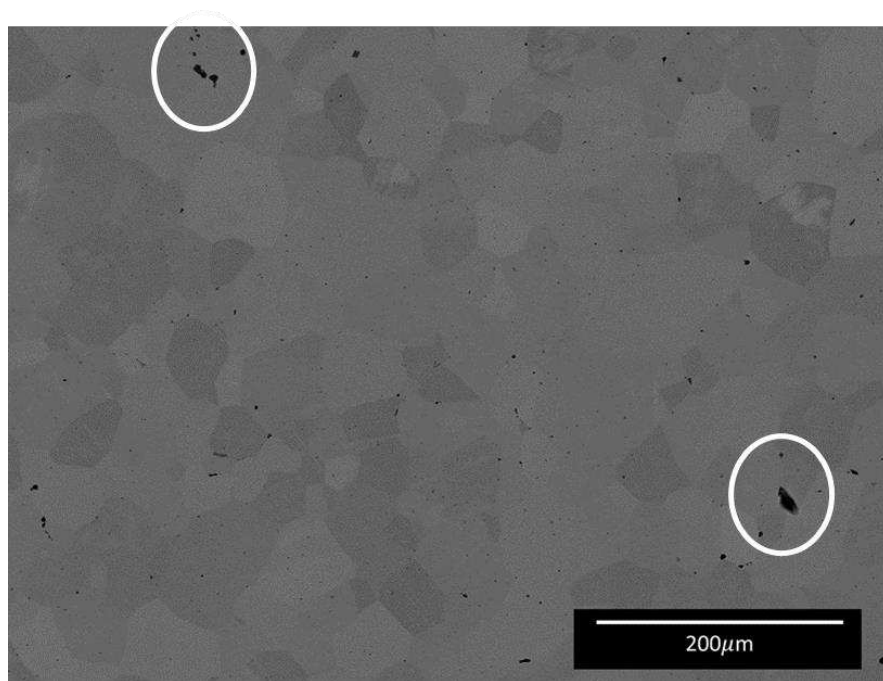


Figure A1: An example backscatter electron micrograph of the spray formed Co₅₅Cr₄₀Ni₅ alloy, showing a few large pores, circled in white. Grain contrast is a result of channeling contrast. Sample was section from the as cast material and mechanically polished to 0.05 μm.

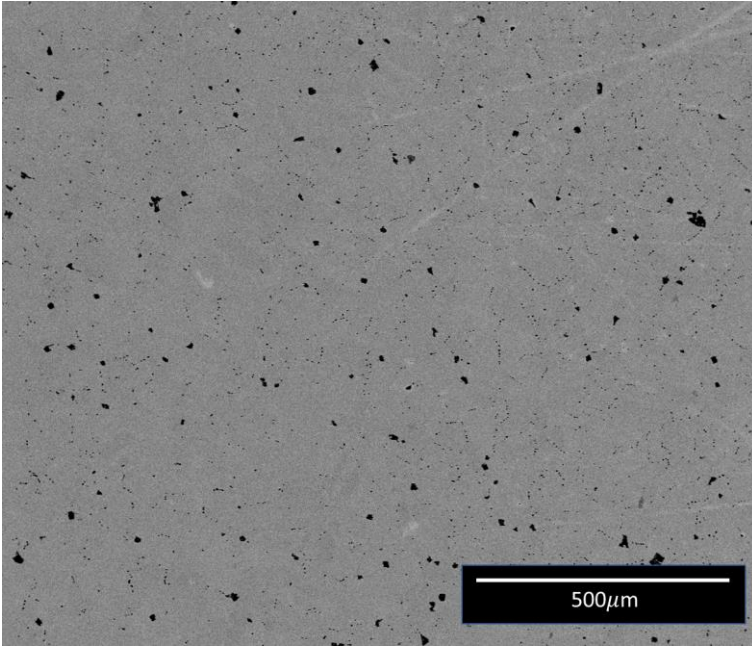


Figure A2: MA backscatter electron micrograph of the bulk cast $\text{Co}_{55}\text{Cr}_{40}\text{Ni}_{15}$ alloy produced at UFSCar, illustrating the degree and size of inclusions. Black specks are chromium oxide inclusions. The sample was sectioned from the as cast material, then mechanically polished to $0.5\ \mu\text{m}$.

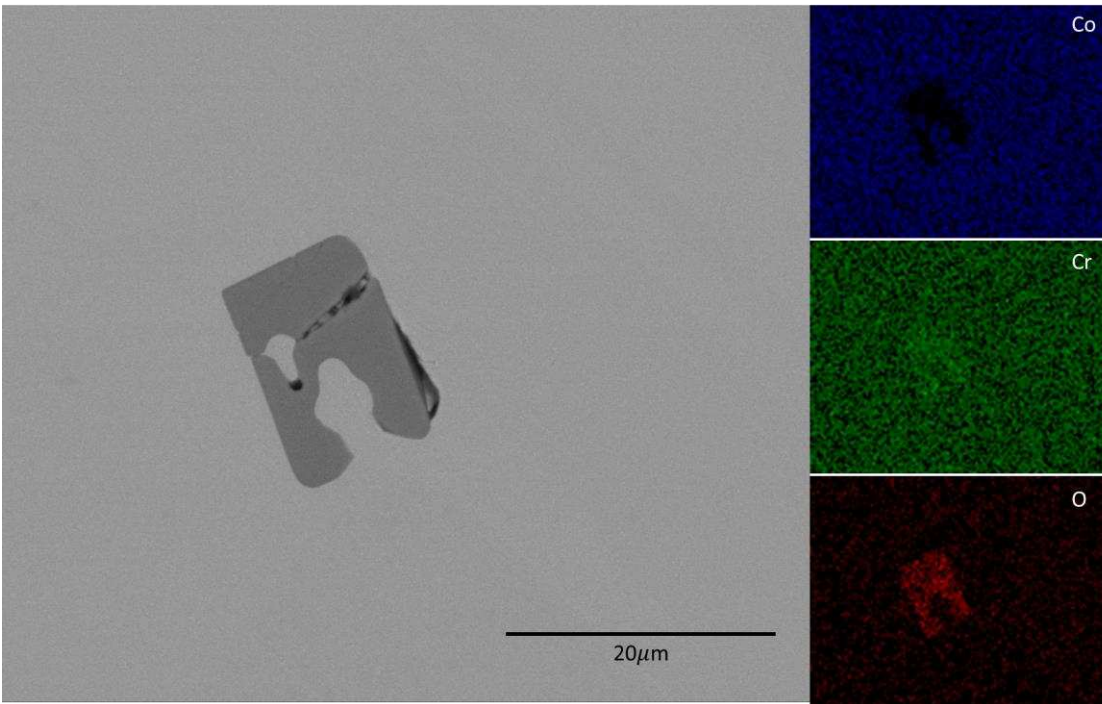


Figure A3: A backscatter electron micrograph of an example chromium-oxide found within the bulk cast $\text{Co}_{55}\text{Cr}_{40}\text{Ni}_{15}$ alloy produced at UFSCar, as well as EDS maps of the relative composition, showing the inclusion is rich in chromium and oxygen, while deficient in cobalt.

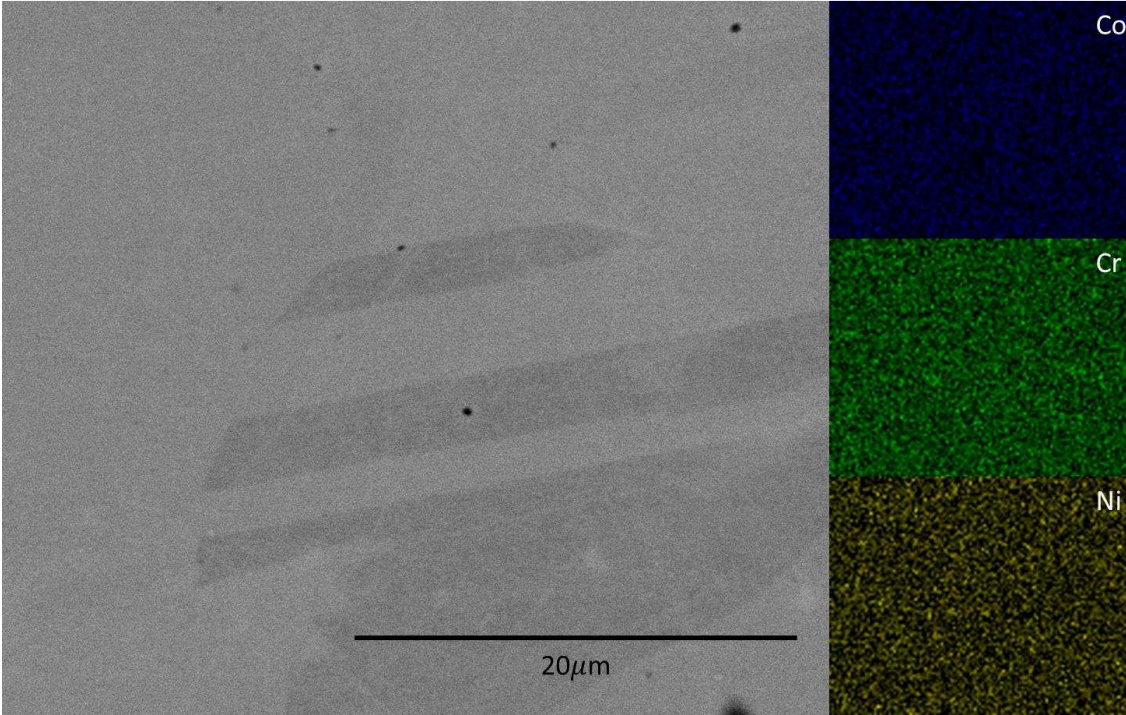


Figure A4: Backscatter electron micrograph and EDS map of the $\text{Co}_{30}\text{Cr}_{40}\text{Ni}_{30}$ alloy produced at Mines by arc melting, cold rolling to 50% reduction in height and annealing at 1200°C for two hours in air, illustrating the lack of visible secondary phases or segregation of the components. Sample was mechanically polished to $1\ \mu\text{m}$.

All tested materials were annealed at temperatures of 1150°C or above for no less than 90 minutes, followed by quenching in water to room temperature before testing. Samples for in-situ testing were encapsulated and annealed in vacuum, otherwise, samples were annealed in open atmosphere. This heat treatment was designed to ensure that the samples reached a fully FCC microstructure during the solutionizing treatment. The phase stability of the tested alloys, as illustrated by the equilibrium phase fractions as predicted by Thermo-Calc 2020a using the TCHEA4 database, is presented for each alloy in **Figures A4-A8**. In the case of the Co55, laboratory x-ray diffraction ($\text{Cu-K}\alpha$, $\lambda = 1.5406\ \text{\AA}$) shows the presence of a small HCP peak, indicating that there is some degree of $\text{FCC} \rightarrow \text{HCP}$ martensitic transformation active in this material. Additional study is required to assess if this is a result of this alloy possessing an M_s temperature above room temperature, or a result of mechanically induced transformation during the removal of oxide from the surface of the samples after heat treatment.

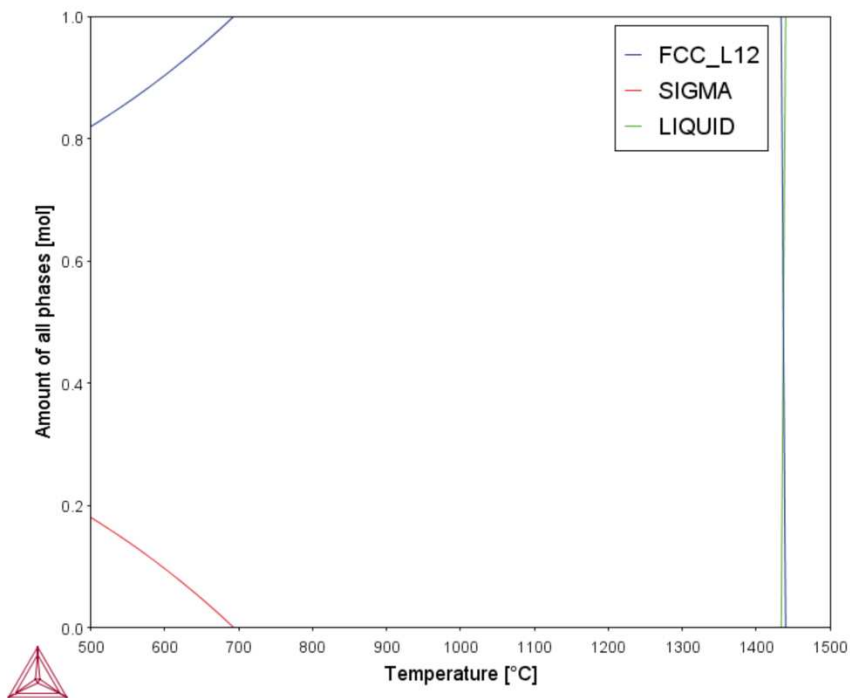


Figure A5: Equilibrium phase fraction for the equiatomic CoCrNi alloy as a function of temperature between 500°C and 1500°C.

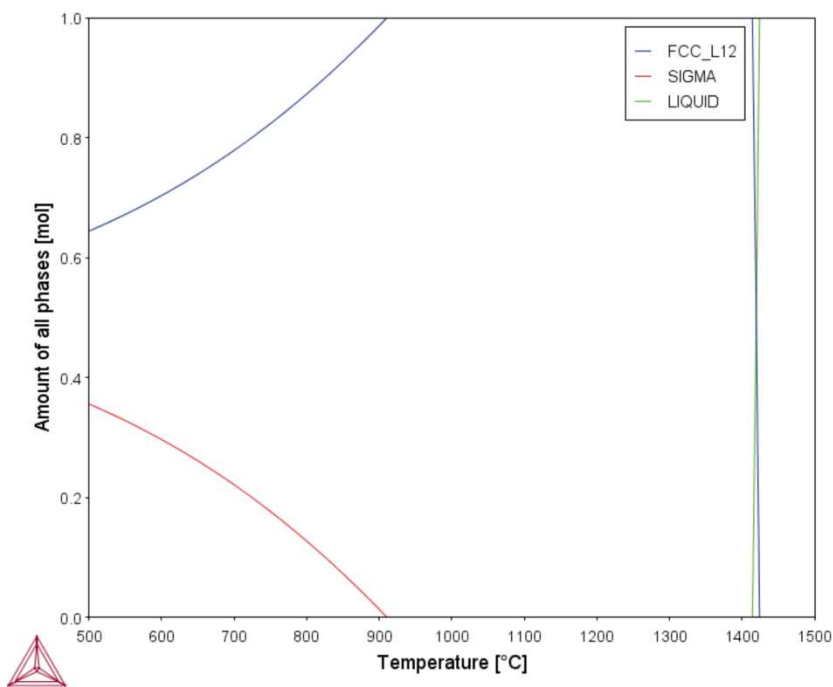


Figure A6: Equilibrium phase fraction for $\text{Co}_{30}\text{Cr}_{40}\text{Ni}_{30}$ as a function of temperature between 500°C and 1500°C.

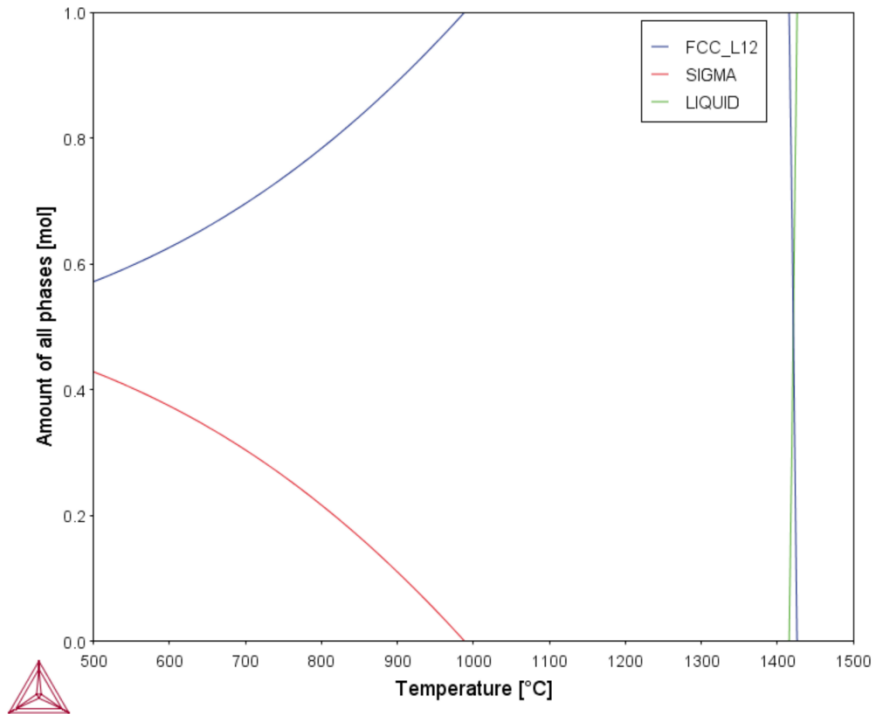


Figure A7: Equilibrium phase fraction for $\text{Co}_{40}\text{Cr}_{40}\text{Ni}_{20}$ as a function of temperature between 500°C and 1500°C.

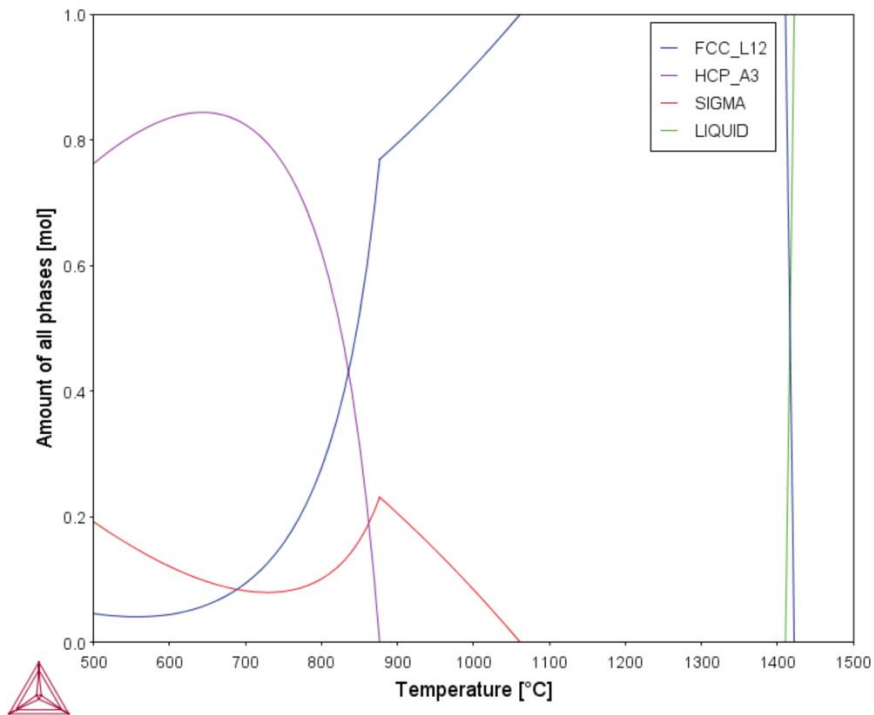


Figure A8: Equilibrium phase fraction for $\text{Co}_{50}\text{Cr}_{40}\text{Ni}_{10}$ as a function of temperature between 500°C and 1500°C.

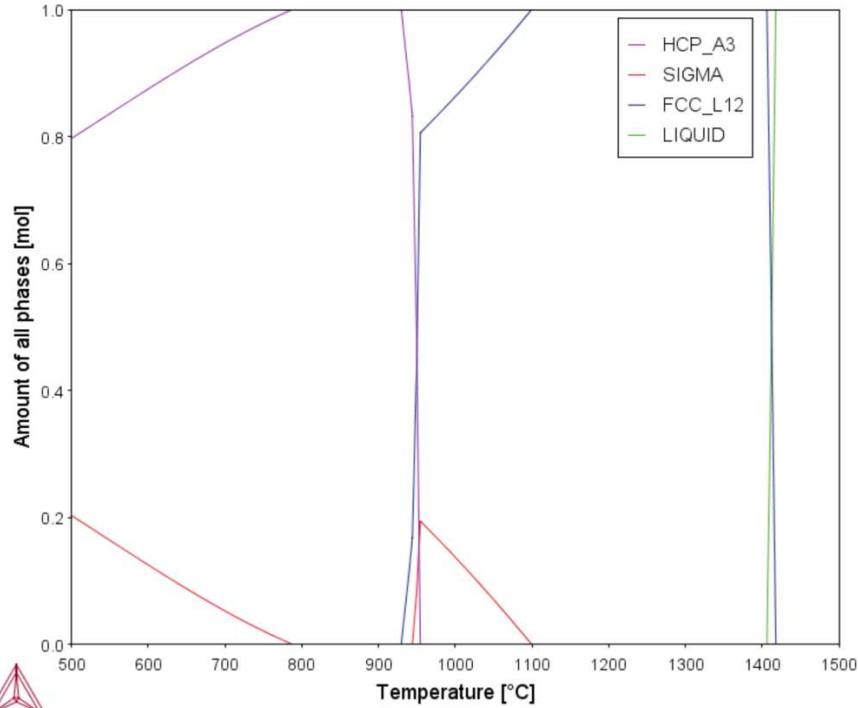


Figure A9: Equilibrium phase fraction for $\text{Co}_{55}\text{Cr}_{40}\text{Ni}_5$ as a function of temperature between 500°C and 1500°C.

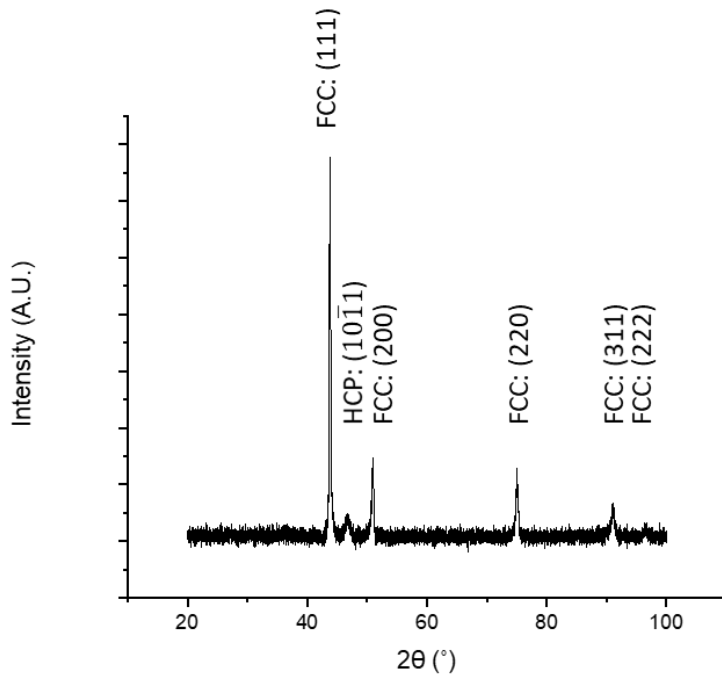


Figure A10: XRD of a Co_{55} sample produced by arc melting, which was rolled to 50% reduction in height then annealed at 1200°C in air for 2 hours, then quenched to room temperature. It is unclear if the HCP present is due to the alloy possessing an M_s temperature above room temperature, or mechanically induced during the removal of oxide formed on the surface of this sample during heat treatment in open atmosphere.

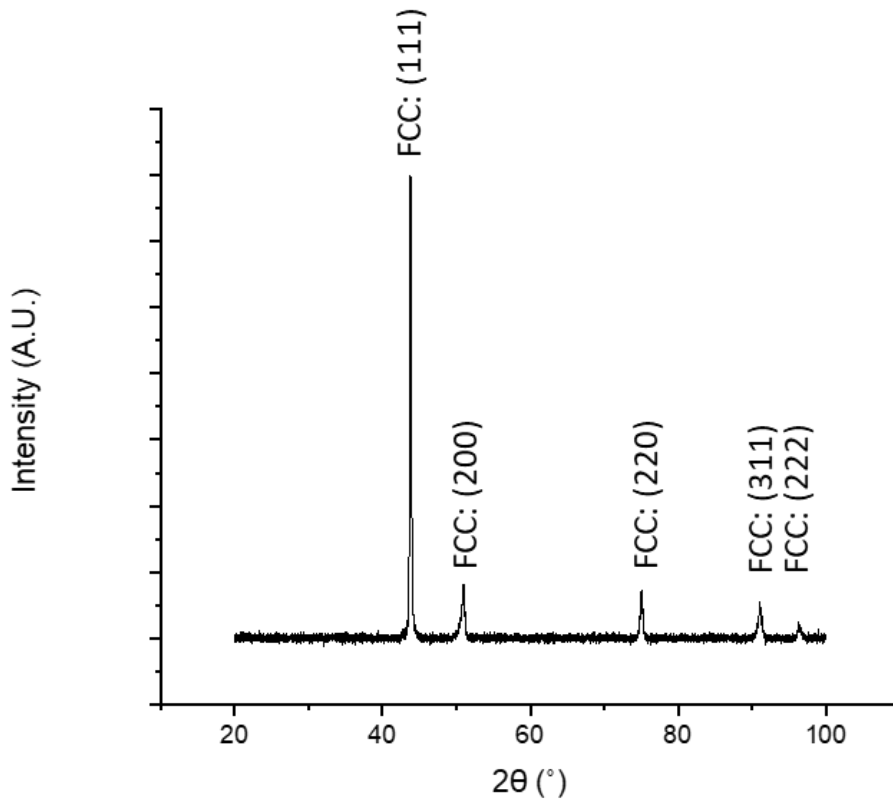


Figure A11: XRD of a Co40 sample produced by arc melting, followed by rolling to 50% reduction in height, annealed at 1200°C in air for 2 hours, then quenched to room temperature. The diffraction indicates a fully FCC microstructure.

Appendix B: Hardness Measurements of CoCrNi MPEAs

Table A1: Vickers hardness measurements of several CoCrNi MPEAs with various reductions in height from rolling. All alloys started in the as annealed condition (1200°C for two hours).

| Rolling Reduction (%) | CoCrNi | | Co30 | | Co40 | | Co50 | |
|-----------------------|-----------|----------------|-----------|----------------|-----------|----------------|-----------|----------------|
| | Mean (HV) | Std. Dev. (HV) | Mean (HV) | Std. Dev. (HV) | Mean (HV) | Std. Dev. (HV) | Mean (HV) | Std. Dev. (HV) |
| 0 | 185.15 | 5.3 | 187.8 | 6.7 | 241.1 | 14.3 | 329.6 | 33.8 |
| 10 | 282.35 | 23.9 | 301.5 | 21.6 | 300.4 | 22.3 | 354.6 | 15.5 |
| 25 | 377.4 | 51.1 | 353.7 | 35.6 | 387.15 | 19.37 | 444.6 | 31.3 |
| 50 | 432.25 | 17.6 | 454.1 | 26.04 | 417.9 | 24.4 | 481.25 | 39.3 |